High-power Few-cycle MID-IR Pulse Generation for Vibrational Spectroscopy

Dissertation
zur Erlangung des Doktorgrades an der Fakultät für
Mathematik, Informatik und Naturwissenschaften
Fachbereich Physik
der Universität Hamburg

vorgelegt von
Cheng Luo
aus
New Taipei City, Taiwan

Hamburg
2025

Gutachter der Dissertation:	Priv.-Doz. Dr. Tim Laarmann Prof. Dr. Markus Drescher
Zusammensetzung der Prüfungskommission:	Priv.-Doz. Dr. Tim Laarmann Prof. Dr. Markus Drescher Prof. Dr. Daniela Pfannkuche Dr. Mikhail Pergament Prof. Dr. Andrea Trabattoni
Vorsitzende der Prüfungskommission:	Prof. Dr. Daniela Pfannkuche
Datum der Disputation:	02.12.2024
Vorsitzender Fach-Promotionsausschuss PHYSIK:	Prof. Dr. Markus Drescher
Leiter des Fachbereichs PHYSIK:	Prof. Dr. Wolfgang J. Parak
Dekan der Fakultät MIN:	Prof. Dr.-Ing. Norbert Ritter

Eidesstattliche Versicherung
Declaration on oath

Hiermit versichere ich an Eides statt, dass ich die vorliegende Dissertation selbst verfasst und keine anderen als die angegebenen Quellen und Hilfsmittel benutzt habe.

I hereby declare upon oath that I have written the present dissertation independently and have not used further resources and aids than those stated in the dissertation.

Hamburg, den 11.Juli.2024

Cheng Luo

Abstract

High-power, high-energy, ultrashort, mid-infrared (MID-IR) laser systems operating at high repetition rates are of significant interest for coherent vibrational spectroscopy investigations within the "fingerprint region" ($6 - 16\,\mu m$). First of all, the optical properties of Li-based nonlinear crystals (NLC) for MID-IR generation are evaluated under high power laser irradiation at 1030 nm central wavelength using a thermal imaging method. It turns out that lithium gallium sulfide (LGS) crystal exhibits a relatively low linear absorption coefficient $< 0.002\,cm^{-1}$, the lowest nonlinear absorption coefficient $< 3.2{\times}10^{-4}\,cm/W$ and a nonlinear refractive index $< 6.4{\times}10^{-15}\,cm^2/W$, positioning it as a highly promising material candidate for MID-IR optical parametric chirped-pulse amplifier (OPCPA) applications.

Based on the LGS crystal, a versatile design of a MID-IR OPCPA laser system is developed, featuring two complementary operation modes differ that in the group-delay dispersion (GDD) of the signal pulse. One scheme provides a wavelength-tunable source (from 4.2 to 11 μm) at ≈ 1 ps pulse width, while the other sheme generates a broadband pulse (from 7 to 11 μm) centered at 9 μm with 114 fs pulse duration, which corresponds to about 3 optical cycles. Both MID-IR laser operation modes exhibit high average power exceeding 200 mW and high pulse energy of 1.2 μJ operating at 200 kHz, having significant potential for vibrational spectroscopy and microscopy making use of characteristic molecular fingerprints in the MID-IR spectral range.

Moreover, by utilizing the broadband ultrashort MID-IR pulse, the ultrabroadband vibrational sum-frequency generation (BB-VSFG) spectroscopy is demonstrated using glucose pellets as a proof-of-principle sample, revealing 8 characteristic vibrational modes spanning from 800 to $1400\,cm^{-1}$. Notably, the carbon-oxygen bond stretching mode at $1035\,cm^{-1}$ shows high sensitivity to biologically relevant 10 mM of glucose solution in the VSFG spectra. Consequently, this methodology holds promise for blood sugar monitoring in diabetic individuals.

Kurzfassung

Leistungsstarke, energiereiche, ultrakurze Lasersysteme mit Wellenlängen λ im mittleren Infrarot (MID-IR), die mit hohen Wiederholraten arbeiten, sind von erheblichem Interesse für kohärente Schwingungsspektroskopie im sogenannten "Fingerabdruckbereich" ($6 < \lambda < 16\,\mu m$). Zunächst werden die optischen Eigenschaften von nichtlinearen Kristallen (NLC) auf Li-Basis für die MID-IR-Erzeugung unter Verwendung eines Hochleistungslasers bei 1030 nm mittels einer thermischen Bildgebungsmethode vermessen. Es zeigt sich, dass Lithium-Gallium-Sulfid (LGS) Kristall einen relativ niedrigeren linearen Absorptionskoeffizienten $< 0.002\,cm^{-1}$, den niedrigsten nichtlinearen Absorptionskoeffizienten $<3.2\times10^{-4}$ cm/W und einen nichtlinearen Brechungsindex $<6.4\times10^{-15}\,cm^2/W$ besitzt, was dieses Material zu einem vielversprechenden Kandidaten für Anwendungen im Bereich der MID-IR optisch parametrischen Verstärkung mit gestreckten Pulsen (OPCPA) macht.

Auf der Grundlage des LGS-Kristalls wurde ein vielseitiges Design eines MID-IR OPCPA Lasersystems entwickelt, das sich durch zwei komplementäre Betriebsmodi auszeichnet, welche sich in der Gruppenverzögerungsdispersion (GDD) des Signalpulses unterscheiden. Das eine Schema bietet eine in der Wellenlänge abstimmbare (von 4.2 bis 11 µm) Quelle bei ≈ 1 ps. Das andere Schema erzeugt breitbandige (von 7 bis 11 µm), auf 9 µm Wellenlänge zentrierte Pulse mit einer Pulsdauer von 114 fs, welches etwa 3 optischen Zyklen entspricht. Beide MID-IR-Betriebsmodi weisen eine hohe mittlere Leistung von über 200 mW und eine hohe Pulsenergie von 1.2 µJ bei 200 kHz auf, was ein erhebliches Potenzial für die Schwingungsspektroskopie und Mikroskopie von Molekülen bietet, indem charakteristische molekulare Fingerabdrücke im MID-IR Spektralbereich genutzt werden.

Darüber hinaus wird durch die Verwendung des breitbandigen ultrakurzen MID-IR-Pulses die ultrabreitbandige Schwingungs-Summen-Frequenz-Erzeugung (BB-VSFG) in Glukose Pellets als Proof-of-Principle Probe demonstriert, wobei 8 charakteristische Schwingungsmoden von 800 bis 1400 cm^{-1} sichtbar werden. Insbesondere die Streckschwingung der Kohlenstoff-Sauerstoff-Bindung bei 1035 cm^{-1} zeigt in den VSFG-Spektren eine hohe Sensitivität für eine biologisch relevante 10 mM Glukose Lösung. Folglich ist diese Methode ein Erfolg versprechender, Ansatz für die Blutzuckerüberwachung bei Diabetikern.

Contents

Chapter 1

Introduction

Early detection of health problems and prompt delivery of treatment are the key to maintaining good health and a long lifespan. Preventive healthcare is dependent on the ability to reliably detect a process from health to disease by efficient and sensitive screening techniques. In recent years, infrared vibrational spectroscopy of biofluids could offer that capacity, because abundant information of important biomolecules can be accessed within the infrared range from 6 to 16 μm which is also called "fingerprint region". For example, Krausz et al. have studied infrared fingerprints of plasma and serum samples from 1639 individuals, and found the distinct signatures of breast, bladder, prostate, and lung cancer[1]. By machine learning algorithm, individuals can be classified based on four types of cancer, thereby presenting a novel approach for cancer diagnosis.

Another application of the infrared technique is blood sugar sensing. It is estimated by the International Diabetes Federation (IDF) that, around 783 million adults, equating to 1 in 8 individuals, will be affected by diabetes by 2045[2]. For tackling diabetes, it is essential to monitor the blood glucose levels of individuals between 4-11 mM. However, the conventional method of using a finger pricker for measurement can be uncomfortable, and there may be variations in blood sugar readings between different test strips. Hence, developing a noninvasive and highly sensitive method of glucose detection is also of considerable interest. So far, some techniques with incoherent light sources were developed to observe the vibrational spectrum of blood sugar like: MID-IR spectroscopic imaging of the wrist[3] and Raman spectroscopy in vivo skin[4]. In general, the detection of glucose signal is quite challenging due to the absorption of light by non-glucose-specific components in vivo. Therefore, signal enhancement by the methods of nonlinear optics such as coherent anti-stokes Raman scattering (CARS)[5] and stimulated Raman scattering (SRS)[6] can improve sensitivity. Furthermore, field-resolved spectroscopy

(FRS)[7] by ultrashort MID-IR pulses owns higher sensitivity and accuracy to probe the glucose concentration until 0.1 mM.

To follow up on the above ideas, a high-power and energy MID-IR ultrashort pulses provided at high repetition rate are highly needed. In order to develop such a laser system for vibrational spectroscopy, several questions have to be addressed: first, what could be the suitable nonlinear crystal for MID-IR generation in realistic operational conditions? Second, how to build up a versatile high-power MID-IR laser system, which covers our interested spectral region and also allows for few-cycle (broad spectral bandwidth) operation? Third, what is the level of sensitivity in glucose detection using vibrational spectroscopy? For answering these questions, this research work is structured as following: Chapter2 explains the theoretical background of ultrashort laser pulse generation and characterization, nonlinear optics, OPCPA and vibrational sum-frequency generation spectroscopy. Chapter3 presents the optical properties of lithium-based nonlinear crystals under high-power laser pumping. By thermal investigation during operation, some optical parameters such as linear and nonlinear absorption coefficients and the nonlinear refractive index are obtained. The most promising candidate among these NLCs is lithium gallium sulfide (LGS) selected for MID-IR generation. Chapter4 introduces the home-built MID-IR OPCPA which exhibits two complementary operation modes by manipulating the chirped signal pulse when generating the MID-IR idler. One configuration shows wavelength-tunable MID-IR pulses with ≈ 1 ps pulse duration, while the other exhibits a broad MID-IR spectral bandwidth supporting ≈ 100 fs pulse duration. Chapter5 shows characteristic examples of broadband vibrational sum-frequency-generation spectroscopy from solid state samples (quartz) to biomolecules in aqueous solution (glucose). Moreover, the later concentration dependent experiments on glucose solutions demonstrate the high sensitivity required for sensing blood sugar levels.

Chapter 2

Theoretical Background

2.1 Ultrashort Laser Pulse

Ultrashort laser pulses are electromagnetic wave packets, fully described by the electric field representation in time and space domain. The propagation and interaction with matter are governed by Maxwell's equations with taking into account the polarization in material. In a simple case, we begin with the temporal dependence of the electric field amplitude neglecting its spatial and polarization dependence, i.e., $\mathbf{E}(x, y, z, t) = E(t)$. In general, the complex representation of the electric field is more convenient to be used, although all observables are real quantities[1]. Through Fourier transform, the field can be described in frequency domain and be transformed to time domain inversely:

$$\tilde{E}(\omega) = \mathcal{F}\{E(t)\} = \int_{-\infty}^{\infty} E(t)\mathrm{e}^{-i\omega t}\, dt \tag{2.1.1}$$

$$E(t) = \mathcal{F}^{-1}\{E(\omega)\} = \frac{1}{2\pi}\int_{-\infty}^{\infty} \tilde{E}(\omega)\mathrm{e}^{i\omega t}\, d\omega. \tag{2.1.2}$$

Practically, the functions of negative frequencies are not real, and the complex representation of the electric field in time domain is necessary. Both needs can be met by introducing an electric field in complex form as

$$\tilde{E}^{+}(\omega) = |\tilde{E}(\omega)|\mathrm{e}^{i\phi(\omega)} = \begin{cases} \tilde{E}(\omega) & \text{for } \omega \geq 0 \\ 0 & \text{for } \omega < 0, \end{cases} \tag{2.1.3}$$

where $|\tilde{E}(\omega)|$ denotes the spectral amplitude, and $\phi(\omega)$ is the spectral phase.

[1]Following the way of notation in the book (Diels & Rudolph, 2006, p.1-9)[8], the complex quantities related to the field are typically written with a tilde.

By the definition of the complex Fourier transform, $\tilde{E}^+(t)$ and $\tilde{E}^+(\omega)$ are related with one another

$$\tilde{E}^+(t) = \frac{1}{2\pi}\int_{-\infty}^{\infty} \tilde{E}^+(\omega)\mathrm{e}^{i\omega t}d\omega \tag{2.1.4}$$

$$\tilde{E}^+(\omega) = \int_{-\infty}^{\infty} \tilde{E}^+(t)\mathrm{e}^{-i\omega t}dt. \tag{2.1.5}$$

The actual physical electric field and its complex Fourier transform can be represented using the variables obtained from earlier equations, along with the corresponding variables $\tilde{E}^-(t)$, $\tilde{E}^-(\omega)$ for the negative frequencies. The electric field quantity can be expressed in this manner

$$E(t) = \tilde{E}^+(t) + \tilde{E}^-(t) \tag{2.1.6}$$

$$E(\omega) = \tilde{E}^+(\omega) + \tilde{E}^-(\omega). \tag{2.1.7}$$

In most practical cases relevant, the spectral amplitude is typically concentrated around an average frequency denoted as ω_ℓ , with significant values existing within a narrow frequency range $\Delta\omega$ that is considerably smaller than ω_ℓ. This implies the utility of incorporating a carrier frequency ω_ℓ and expressing $\tilde{E}^+(t)$ accordingly in the time domain

$$\tilde{E}^+(t) = \frac{1}{2}\mathcal{E}(t)\mathrm{e}^{i\phi_0}\mathrm{e}^{i\phi(t)}\mathrm{e}^{i\omega_\ell t} = \frac{1}{2}\tilde{\mathcal{E}}(t)\mathrm{e}^{i\omega_\ell t}, \tag{2.1.8}$$

the time-varying phase function ϕ(t) and the complex field envelope $\tilde{\mathcal{E}}(t)$ are defined, with $\mathcal{E}$ representing the real-field envelope. The constant phase term ϕ_0 is typically insignificant and can be disregarded, except in cases involving short pulses, where it influences the interaction with matter, known as the "carrier-to-envelope phase" (CEP). Monitoring and managing ϕ_0 can be crucial in such scenarios. The mathematical description of an ultrashort pulse is plotted in Fig.2.1

In practical terms, the intensity (W/cm^2) is a measurable quantity per unit area. As the laser pulse represents as a propagating electromagnetic wave packet, its spectrum lacks a direct current (DC) component, resulting in a value of zero in the time integral over the electric field. The intensity can also be expressed as

$$I(t) = \epsilon_0 cn\frac{1}{T}\int_{t-T/2}^{t+T/2} E^2(t')dt' = \frac{1}{2}\epsilon_0 cn\tilde{\mathcal{E}}^2(t) \tag{2.1.9}$$

The spectral characteristics of light are commonly determined by assessing the field's intensity at the output of a spectrometer, without temporal resolution. The quantity being measured is the spectral intensity.

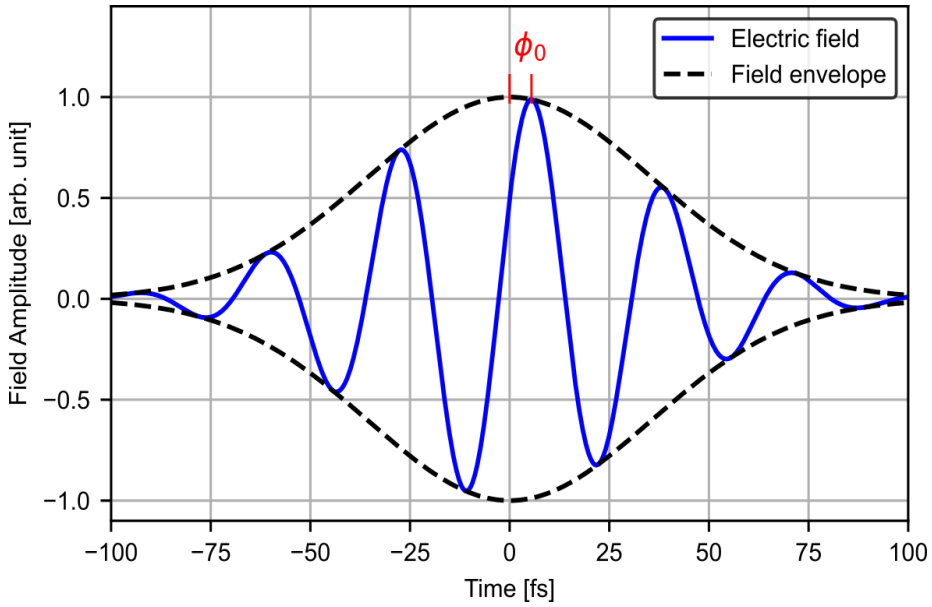

Figure 2.1: A 100 fs ultrashort pulse, which is composed of few optical cycles. CEP ϕ_0 denotes the offset between the peak of the pulse envelope and the nearest peak of the carrier-wave electric field.

$$S(\omega) = |\eta(\omega)\tilde{E}^{+}(\omega)|^2, \tag{2.1.10}$$

The parameter η represents a scaling factor that considers various factors such as losses, geometrical effects, and the limited resolution of the spectrometer. In the case of an ideal spectrometer, the value of $|\eta|^2$ can be calculated based on the principle of energy conservation

$$|\eta|^2 \int_{-\infty}^{\infty} |\tilde{E}^{+}(\omega)|^2 d\omega = 2\epsilon_0 cn \int_{-\infty}^{\infty} \tilde{E}^{+}(t)\tilde{E}^{-}(t)dt \tag{2.1.11}$$

and Parseval's theorem in mathematics

$$\int_{-\infty}^{\infty} |\tilde{E}^{+}(t)|^2 dt = \frac{1}{2\pi} \int_{0}^{\infty} |\tilde{E}^{+}(\omega)|^2 d\omega \tag{2.1.12}$$

from which follows

$$|\eta|^2 = \epsilon_0 cn/\pi. \tag{2.1.13}$$

The complete expression for the spectral intensity is thus:

$$S(\omega) = \frac{\epsilon_0 cn}{4\pi} |\tilde{\mathcal{E}}(\omega - \omega_\ell)|^2. \tag{2.1.14}$$

2.2 Nonlinear Optics

The study of phenomena that occur as the modifications of the optical properties in materials in the course of the light-matter interaction is called "nonlinear optics." Due to the high intensity of lasers, the field of nonlinear optics were opened up after the invention of laser. Literally, the nonlinear optical phenomena indicate that the response to an applied optical field in materials depends on the strength of the optical field in a nonlinear way. For example, the intensity of the second-harmonic generation increases along with the square of the intensity of the applied laser. For more precise description in physics, let's begin with the case of conventional optics, i.e. that the induced polarization $\tilde{\mathbf{P}}(t)$ of a material system depends linearly on the strength $\tilde{\mathbf{E}}(t)$of the applied electric field[2]

$$\tilde{\mathbf{P}}(t) = \epsilon_0 \chi^{(1)} \tilde{\mathbf{E}}(t), \tag{2.2.1}$$

where the constant of proportionality $\chi^{(1)}$ is known as the linear susceptibility and ϵ_0 is the permittivity of free space. Furthermore, Eq.2.2.1 can be generalized as a power series in field strength $\tilde{\mathbf{E}}(t)$ for expressing the polarization $\tilde{\mathbf{P}}(t)$ as

$$\begin{aligned} \tilde{\mathbf{P}}(t) =& \epsilon_0[\chi^{(1)}\tilde{\mathbf{E}}(t) + \chi^{(2)}\tilde{\mathbf{E}}^2(t) + \chi^{(3)}\tilde{\mathbf{E}}^3(t) + \cdots] \\ \equiv& \tilde{\mathbf{P}}^{(1)}(t) + \tilde{\mathbf{P}}^{(2)}(t) + \tilde{\mathbf{P}}^{(3)}(t) + \cdots . \end{aligned} \tag{2.2.2}$$

The quantities $\chi^{(2)}$ and $\chi^{(3)}$ are known as the second- and third-order nonlinear optical tensor, and $\tilde{\mathbf{P}}^{(2)}(t)$, $\tilde{\mathbf{P}}^{(3)}(t)$ are referred to as the second- and third-order nonlinear polarization, the higher-order terms can be derived and so on. Among the higher-order polarizations, the second-order nonlinear polarization are often used in the present work. Therefore, let's consider the common circumstance in which a second-order nonlinear optical medium interacts with two distinct frequency components, which is represented in the form

$$\tilde{\mathbf{E}}(t) = \tilde{\mathbf{E}}_1 \mathrm{e}^{i\omega_1 t} + \tilde{\mathbf{E}}_2 \mathrm{e}^{i\omega_2 t} + c.c. \tag{2.2.3}$$

[2]According to the book (R. W. Boyd, 2008, p.69-74)[9], the tilde (˜) denotes a quantity that varies rapidly in time. Constant quantities, slowly varying quantities, and Fourier amplitudes are written without the tilde. We begin to use this notation from this section to the end.

Then, we bring the superposition of electric fields into Eq.2.2.2, and the second-order term becomes:

$$\begin{aligned}\tilde{\mathbf{P}}(t) &= \epsilon_0\chi^{(2)}\tilde{\mathbf{E}}^2(t) \\ &= 2\epsilon_0 d_{\text{eff}}\big\{\tilde{\mathbf{E}}_1^2 e^{i2\omega_1 t} + \tilde{\mathbf{E}}_2^2 e^{i2\omega_2 t} + c.c. && \text{(SHG)} \\ &\qquad + 2\tilde{\mathbf{E}}_1\tilde{\mathbf{E}}_2 e^{i(\omega_1+\omega_2)t} + c.c. && \text{(SFG)} \\ &\qquad + 2\tilde{\mathbf{E}}_1\tilde{\mathbf{E}}_2^* e^{i(\omega_1-\omega_2)t} + c.c. && \text{(DFG)} \\ &\qquad + 2[\tilde{\mathbf{E}}_1\tilde{\mathbf{E}}_1^* + \tilde{\mathbf{E}}_2\tilde{\mathbf{E}}_2^*]\big\} && \text{(OR),} \end{aligned} \tag{2.2.4}$$

where d_{eff} is the so-called effective nonlinear optical coefficient, which is determined by the specific components of $\chi^{(2)}$. According to the frequency given on the power of exponential terms, the names of physical process are denoted, such as $2\omega_1$, $2\omega_2$ (second-harmonic generation, SHG), $\omega_1 + \omega_2$ (sum-frequency generation, SFG), $\omega_1 - \omega_2$ (difference-frequency generation, DFG), and optical rectification (OR). It is worth to note that, because each of these quantities has its complex conjugate, there is also a response at the negative frequency. Nevertheless, it is unnecessary to take account of both the positive and negative frequency components, so these terms at negative frequencies are presented in the denotation of *c.c.*.

Eq.2.2.4 can be understood that the second-order polarization generates new frequency components, which are very different to the incident radiation field, acting as sources of the electromagnetic field at new frequencies. From the aspect of observation, SHG can be seen as the destruction of two photons of frequency ω_1 (or ω_2) and the creation a photon of frequency $2\omega_1$ (or $2\omega_2$) simultaneously. Likewise, after absorbing two photons of frequency ω_1 and ω_2, SFG emits a photon of sum frequency, and the photon at the difference frequency is emitted via DFG. Lastly, the quasi-DC component creates a static electric field by optical rectification, leading to the radiation of an electromagnetic single-cycle pulse, whose central frequency is in the terahertz spectral region.

So far, the basic phenomena of the second-order polarization have been introduced. For describing the temporal evolution of the incident electromagnetic fields ($\tilde{\mathbf{E}}$ and $\tilde{\mathbf{B}}$) by means of the Maxwell equations, the polarization and the fields, which are generated from the polarization itself in the nonlinear optical medium, have to be involved. The formulas are written with the electric displacement field $\tilde{\mathbf{D}}$ and the magnetizing field $\tilde{\mathbf{H}}$ in the material

$$\nabla \cdot \tilde{\mathbf{D}} = \tilde{\rho}, \tag{2.2.5}$$

$$\nabla \cdot \tilde{\mathbf{B}} = 0, \tag{2.2.6}$$

$$\nabla \times \tilde{\mathbf{E}} = -\frac{\partial \tilde{\mathbf{B}}}{\partial t}, \tag{2.2.7}$$

$$\nabla \times \tilde{\mathbf{H}} = -\frac{\partial \tilde{\mathbf{D}}}{\partial t} + \tilde{\mathbf{J}}. \tag{2.2.8}$$

The region where we solve the equations has no free charge ($\tilde{\rho} = 0$) and no free current ($\tilde{\mathbf{J}} = 0$). Besides, the material is assumed to be nonmagnetic, and the polarization depends on the local strength of the electric field inside. Hence, the fields in material can be written as

$$\tilde{\mathbf{B}} = \mu_0 \tilde{\mathbf{H}}, \tag{2.2.9}$$

$$\tilde{\mathbf{D}} = \epsilon_0 \tilde{\mathbf{E}} + \tilde{\mathbf{P}}. \tag{2.2.10}$$

Then, we take the curl of both sides in Eq.2.2.7. On the left-hand side, the identity from vector calculus can be utilized ($\nabla \times \nabla \times \tilde{\mathbf{E}} = \nabla(\nabla \cdot \tilde{\mathbf{E}}) - \nabla^2 \tilde{\mathbf{E}}$), and the $\nabla \cdot \tilde{\mathbf{E}}$ term is always dropped, because of slowly varying envelope approximation. On the right-hand side, Eq.2.2.9 and 2.2.8 are used to replace $\nabla \times \tilde{\mathbf{B}}$ by $\mu_0(\partial \tilde{\mathbf{D}}/\partial t)$, so that the wave equation can be obtained as

$$\nabla^2 \tilde{\mathbf{E}} - \frac{1}{c^2} \frac{\partial^2 \tilde{\mathbf{E}}}{\partial t^2} = \frac{1}{\epsilon_0 c^2} \frac{\partial^2 \tilde{\mathbf{P}}}{\partial t^2} \tag{2.2.11}$$

As we are interested in the nonlinear response in the wave equation, it is often convenient to split $\tilde{\mathbf{P}}$ into linear and nonlinear parts

$$\tilde{\mathbf{P}} = \tilde{\mathbf{P}}^{(1)} + \tilde{\mathbf{P}}^{NL}, \tag{2.2.12}$$

and the displacement field $\tilde{\mathbf{D}}$ can be decomposed and expressed with a dielectric tensor[3] $\boldsymbol{\epsilon}^{(\mathbf{1})}$

$$\tilde{\mathbf{D}} = \tilde{\mathbf{D}}^{(1)} + \tilde{\mathbf{P}}^{NL} = \epsilon_0 \boldsymbol{\epsilon}^{(\mathbf{1})} * \tilde{\mathbf{E}} + \tilde{\mathbf{P}}^{NL}. \tag{2.2.13}$$

where * is a convolution symbol. From Eq.2.2.10 and 2.2.13 the wave equation 2.2.11 can be rewritten as

$$\nabla^2 \tilde{\mathbf{E}} - \frac{1}{c^2} \frac{\partial^2}{\partial t^2} [\boldsymbol{\epsilon}^{(\mathbf{1})} * \tilde{\mathbf{E}}] = \frac{1}{\epsilon_0 c^2} \frac{\partial^2 \tilde{\mathbf{P}}^{NL}}{\partial t^2} \tag{2.2.14}$$

[3] In dispersionless and lossless material, $\boldsymbol{\epsilon}^{(\mathbf{1})}$ is a real and frequency-independent dielectric tensor.

In the case of dispersive media, this equation is useful to describe the linear propagation of a pulse, which is composed of monochromatic waves at multi-frequencies in the absence of nonlinear polarization $\tilde{\mathbf{P}}^{\mathrm{NL}} \simeq 0$. To solve this equation is particularly straightforward in the frequency domain. Hence, we take the Fourier transform of both sides of Eq.2.2.14, and limit the propagation in z-direction for simplicity

$$\frac{\partial^2 \tilde{E}(z,\omega)}{\partial z^2} + \frac{\omega^2}{c^2} n(\omega)^2 \tilde{E}(z,\omega) = 0, \tag{2.2.15}$$

where n is a frequency-dependent refractive index and satisfies $\mathrm{n}(\omega)^2 = \boldsymbol{\epsilon}^{(1)}(\omega)$. The general solution of the field is

$$\tilde{E}(z,\omega) = \tilde{E}_p(\omega)\mathrm{e}^{-ik(\omega)z} + \tilde{E}_r(\omega)\mathrm{e}^{ik(\omega)z}, \tag{2.2.16}$$

where the wave vector $\mathrm{k}(\omega) = \omega\ \mathrm{n}(\omega)/\mathrm{c}$ is introduced and $\tilde{\mathrm{E}}_p(\omega)$, $\tilde{\mathrm{E}}_r(\omega)$ are the complex amplitudes of progressive and regressive waves, respectively. Finally, we take the inverse Fourier transform of the progressive term of field

$$\tilde{E}(z,t) = \frac{1}{2\pi} \int_{-\infty}^{\infty} \tilde{E}(\omega)\mathrm{e}^{i[\omega t - \phi]} d\omega, \tag{2.2.17}$$

here $\tilde{\mathrm{E}}(\omega)$ is the Fourier transform of $\tilde{\mathrm{E}}(z = 0, \mathrm{t})$. This mathematical form conveys an intuitive concept that a propagating pulse is a superposition of traveling monochromatic waves at frequency ω with a spectral phase $\phi = \mathrm{E}(\omega)z$, which is accumulated by each monochromatic wave along propagation. The dependence of ϕ on ω determines the pulse dispersion, which will be discussed in Sec.2.4.

2.3 Optical Parametric Amplification

In the previous section, the second-order polarization induced by applying fields and their wave equation in a material were derived. Actually, the mechanism of optical parametric amplification (OPA) is similar to DFG, except for the intensities of interacting fields. DFG occurs when the fields of pump and signal are at comparable intensities, while OPA happens when the field of the signal is much weaker than that of the pump. The principle of OPA is the following[10]: the high-intensity beam at higher frequency ω_3 pumps the nonlinear crystal, and transfers energy to the signal beam. The latter is at lower frequency ω_1 with lower incident intensity, which is thus amplified; in addition the idler beam at frequency ω_2 is generated via DFG.

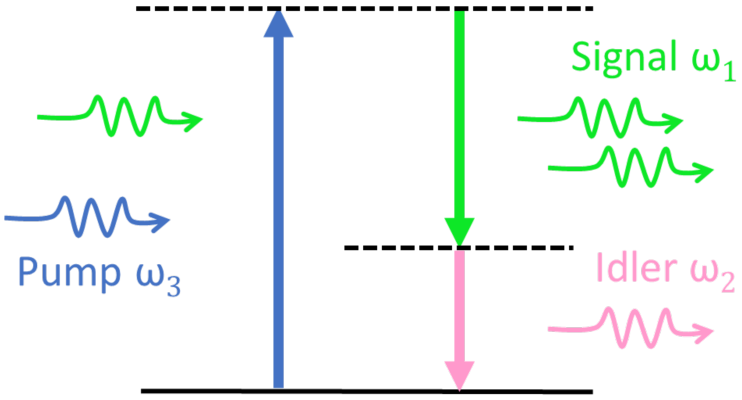

Figure 2.2: Optical parametric amplification can be seen as the stimulated emissions of signal and idler photons after pumping the virtual level in a nonlinear crystal.

As visualized in Fig.2.2, the OPA process can also be explained in the viewpoint of collision obeying conservation laws: a photon at frequency ω_3 is absorbed by the virtual level of a nonlinear crystal, and a photon at frequency ω_1 stimulates the emissions of two photons at frequencies ω_2 and ω_1. The OPA process has to fulfill the energy conservation Eq.2.3.1 and the momentum conservation Eq.2.3.2:

$$\hbar\omega_3 = \hbar\omega_2 + \hbar\omega_1, \tag{2.3.1}$$
$$\hbar\mathbf{k}_3 = \hbar\mathbf{k}_2 + \hbar\mathbf{k}_1 \tag{2.3.2}$$

where $\mathbf{k}_i$ are the wave vectors of the interacting beams. From Eq.2.3.2, the phase-matching condition is obtained as:

$$\Delta\mathbf{k} = \mathbf{k}_3 - \mathbf{k}_2 - \mathbf{k}_1 = 0 \tag{2.3.3}$$

Now, let's consider the propagation of three monochromatic waves along z-direction in nonlinear medium. From the form of Eq.2.2.17 the interacting electric field is

$$\begin{aligned}\tilde{E}(z,t) =& \frac{1}{2}\{\tilde{A}_1(z)\mathrm{e}^{i(\omega_1 t - k_1 z)} \\ &+ \tilde{A}_2(z)\mathrm{e}^{i(\omega_2 t - k_2 z)} + \tilde{A}_3(z)\mathrm{e}^{i(\omega_3 t - k_3 z)}\} + c.c.,\end{aligned} \tag{2.3.4}$$

where[4] the complex amplitude $\mathrm{A_i}$ of the wave is a slowly varying function of z. Its nonlinear second-order polarization $\tilde{\mathrm{P}}^{\mathrm{NL}}$ calculated by Eq.2.2.4 contains

[4]For convenience, the below discussions are in the scalar field approximation.

SHG, SFG, DFG terms, but only the terms at frequency $\omega_1(=\omega_3-\omega_2)$, $\omega_2(=\omega_3-\omega_1)$ and $\omega_3(=\omega_1+\omega_2)$ remain efficiently due to the phase-matching condition.

$$\begin{aligned}\tilde{P}^{NL}(z,t) =&\epsilon_0 d_{\text{eff}}\tilde{A}_2^*(z)\cdot\tilde{A}_3(z)\cdot \mathrm{e}^{i[\omega_1 t-(k_3-k_2)z]}\\ &+\epsilon_0 d_{\text{eff}}\tilde{A}_1^*(z)\cdot\tilde{A}_3(z)\cdot \mathrm{e}^{i[\omega_2 t-(k_3-k_1)z]}\\ &+\epsilon_0 d_{\text{eff}}\tilde{A}_1(z)\cdot\tilde{A}_2(z)\cdot \mathrm{e}^{i[\omega_3 t-(k_1+k_2)z]}+c.c.\end{aligned} \tag{2.3.5}$$

It is worth to note that the nonlinear polarization at one frequency is composed of the product of amplitudes at the other two frequencies, which means three waves are nonlinearly coupled.

By substituting Eq.2.3.5 into Eq.2.2.14, dividing the frequency components into three equations, and dropping the term $\partial^2\tilde{\mathrm{A}}(z)/\partial \mathrm{z}^2$ because of the slowly varying envelope approximation. The coupled wave equations of fields can be obtained

$$\begin{aligned}\frac{\partial\tilde{A}_1(z)}{\partial z} &= -i\sigma_1 A_2^*(z)\cdot\tilde{A}_3(z)\cdot \mathrm{e}^{-i\Delta kz}\\ \frac{\partial\tilde{A}_2(z)}{\partial z} &= -i\sigma_2 A_1^*(z)\cdot\tilde{A}_3(z)\cdot \mathrm{e}^{-i\Delta kz}\\ \frac{\partial\tilde{A}_3(z)}{\partial z} &= -i\sigma_3 A_1^*(z)\cdot\tilde{A}_2(z)\cdot \mathrm{e}^{i\Delta kz},\end{aligned} \tag{2.3.6}$$

where $\sigma_{\mathrm{i}} = \mathrm{d}_{\text{eff}}\omega_i/\mathrm{cn}_i$ and $\Delta\mathrm{k} = \mathrm{k}_3\text{-}\mathrm{k}_2\text{-}\mathrm{k}_1$, which is called wave-vector mismatch. Note that A_1 (signal) and A_2 (idler) have the identical form, which means the fields at frequency ω_1 (signal) and ω_2 (idler) are equally important to amplification and can be exchanged mutually. For solving the coupled wave equations, we assume that the pump beam is strong and undepleted during the interaction ($\mathrm{A}_3 \approx$ constant) and there is no idler beam in the beginning ($\mathrm{A}_2(0)=0$) as the boundary conditions. The solutions of signal and idler intensities are[5]:

[5]For the detailed manipulations the reader is referred to to the article (Manzoni & Cerullo, 2016, p.4-5)[10] and the book (Boyd, 2008, p.105-108)[9].

$$I_1(L) \simeq I_1(0)\left(\frac{\Gamma}{g}\right)^2 \frac{e^{2gL}}{4} \tag{2.3.7}$$

$$I_2(L) \simeq I_1(0)\frac{\omega_2}{\omega_1}\left(\frac{\Gamma}{g}\right)^2 \frac{e^{2gL}}{4} \tag{2.3.8}$$

$$\text{with } \Gamma^2 = \frac{2d_{\text{eff}}^2\omega_1\omega_2}{c^3\epsilon_0 n_1 n_2 n_3} I_3 \text{ and } g = \sqrt{\Gamma^2 - \frac{\Delta k^2}{4}},$$

where L is the interaction length in the NLC and the phase-matching condition $\Delta k = 0$. The exponential growth of intensities with the interaction length in Eq.2.3.7 and 2.3.8 indicates that an OPA behaves like a real amplifier, which is essentially different from the quadratic growth in the other second-order polarizations like SHG and SFG.

For designing a highly efficient OPA, several crucial parameters, which affect the parametric gain $G(L)=I_1(L)/I_1(0)$ according to Eq.2.3.7, have to be considered. Fist of all, the phase-matching condition $\Delta k = 0$ is one of key factors. The gain value rapidly decreases while there is any fine misalignment of interacting beams leading to the non-zero values of Δk. Second, the d_{eff} value of NLC plays a role from the value Γ, which shows that the higher d_{eff} has higher amplification efficiency. However, the other properties of NLC have to be included in OPA design as well, such as high optical damage threshold, which tolerates the large scaling of pump intensity I_3. Third, continued with the pump intensity I_3, it depends on the pulse duration, energy and the beam size. Hence, the ultrashort pulses are suitable for pumping OPAs, because of their high peak powers. Lastly, the crystal length obviously affects the efficiency. With longer interaction length L of the NLC, the exponential growth of intensities should have higher gain. On the contrary, if the spatial or temporal walk off of the idler beam from the pump gets larger along with longer L, the idler could be absorbed by the NLC or depleted by other parasitic processes, causing a lower gain value. In summary, it is essential to consistently consider the above factors when developing an OPA architecture.

2.4 Chirped Pulse Amplification

As the laser technology was pushed to high power and energy before 1980s, the peak intensity at the level of 10^{15}W/cm^2 could easily cause damages on laser components and detrimental nonlinear pulse distortion, which limited the development of high-power lasers. The experimental breakthrough was the

technique of chirped pulse amplification (CPA) introduced by Strickland and Mourou in 1985[11]. Since then, it revolutionized ultrafast science and was rewarded the Nobel prize in 2018. Currently, the intensity of ultrashort pulses is capable to reach the $10^{23}\,\mathrm{W/cm^2}$ level at the extreme light infrastructure (ELI) for nuclear physics[12].

The idea of CPA is depicted in Fig.2.3: we begin with a transform-limited pulse (the so-called "unchirped pulse"), which has the shortest pulse duration transformed from an optical rainbow spectrum. Before being sent to the optical amplifier, the unchirped pulse is temporally stretched to a much longer duration by a strongly dispersive element (e.g. a grating pair or fiber), becoming a "chirped pulse". In the amplifier, although the power of pulse largely increases, its peak power is reduced dramatically to a level, where the above-mentioned problems can be avoided, because of the long pulse duration. After the amplifier, another dispersive element is used to remove the chirp and temporally compress the pulse to a duration close to the unchirped pulse showing ultra-high peak power. The combination of OPA and CPA is the optical parametric chirped-pulse amplifier (OPCPA), which is the key concept applied in the present thesis for high-power MID-IR laser research and development.

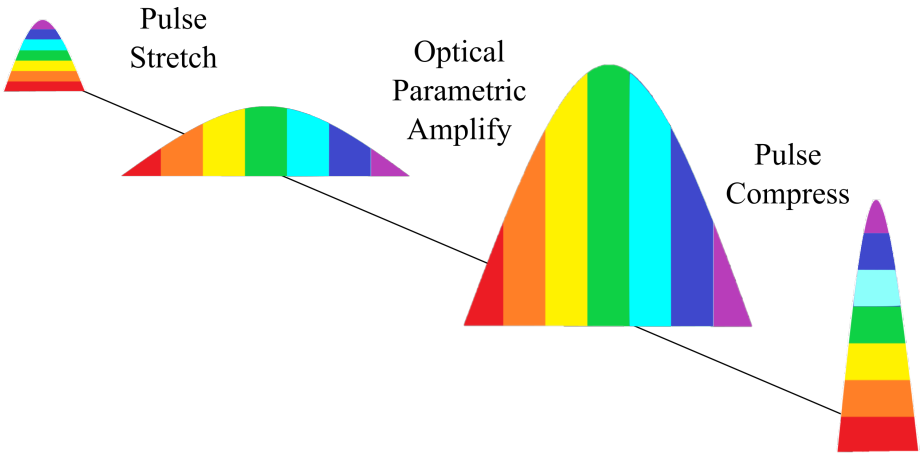

Figure 2.3: Diagram illustrating the methodology of chirped pulse amplification.

Based on the CPA's working principle, the management of chromatic dispersion including the introduction and removal of chirp has to be controlled finely. In order to quantify the chirp in a pulse, the spectral phase $\phi(\omega)$ in Eq.2.2.17, which conveys important information about the propagation of the pulse in a medium, is introduced. Since ϕ depends on ω, it can be described with a Taylor expansion around the pulse carrier frequency ω_ℓ (Manzoni & Cerullo, 2016, p.27-28)[10]

$$\phi(\omega) = \phi_0 + \frac{\partial\phi(\omega)}{\partial\omega}(\omega-\omega_\ell) + \frac{1}{2}\frac{\partial^2\phi(\omega)}{\partial\omega^2}(\omega-\omega_\ell)^2 + \frac{1}{6}\frac{\partial^3\phi(\omega)}{\partial\omega^3}(\omega-\omega_\ell)^3 + \cdots + \frac{1}{n!}\frac{\partial^n\phi(\omega)}{\partial\omega^n}(\omega-\omega_\ell)^n, \tag{2.4.1}$$

where ϕ_0 = carrier-envelope phase (CEP),

$\frac{\partial\phi(\omega)}{\partial\omega}$ = group delay (GD),

$\frac{\partial^2\phi(\omega)}{\partial\omega^2}(\omega-\omega_\ell)^2$ = group delay dispersion (GDD),

$\frac{\partial^3\phi(\omega)}{\partial\omega^3}(\omega-\omega_\ell)^3$ = third-order dispersion (TOD).

CEP is the phase shift between the envelope of the electric field and the carrier wave, which has been introduced in Eq.2.1.8. GD is the temporal delay of a wave packet centered around ω_ℓ after propagating through a dispersive medium. The higher order terms in the expansion, such as GDD and TOD, play a significant role in altering the shape of the pulse. GDD contributes to the stretching of the pulse duration, whereas a high TOD results in an asymmetric temporal profile and the emergence of multiple delayed replicas. Therefore, GDD serves as a crucial parameter for characterizing the chirp in the pulse, which must be accounted for during the CPA process. The correlation between pulse duration and GDD can be expressed as follows:

$$\tau_{out} = \tau\sqrt{1+\left(\frac{GDD}{\tau^2}\right)^2} \tag{2.4.2}$$

In the absence of GDD, the pulse duration is denoted as τ, while τ_{out} represents the broadened pulse duration following propagation through a dispersive medium. In cases where GDD $\gg \tau$ (indicating large dispersion or a short pulse), the equation can be simplified to $\tau_{\text{out}} \approx \text{GDD}/\tau$. This suggests that shorter pulse widths are more susceptible to dispersive broadening. This phenomenon can be conceptually grasped by recognizing that an ultrashort pulse encompasses numerous frequencies, each traveling at distinct group velocities within the medium. Conversely, when GDD $\ll \tau$ (indicating small dispersion or a long pulse), $\tau_{\text{out}} \approx \tau$, and the pulse experiences minimal prolongation.

Another consideration about CPA design is the pulse duration of pump and signal pulse, respectively. Both have to be largely overlapped in time domain for exchanging energy efficiently. For most commercial femtosecond lasers, the pulse duration of the signal pulse is longer than the pump pulse

duration. Thus, a limited number of frequency components of the signal overlapping temporally with the short pump pulse leads to a spectrally narrower amplification bandwidth, corresponding to a longer OPA pulse. Conversely, if the pump pulse is longer than the signal pulse and only limited energy can be transferred, and the OPA is still not efficient. In our case, in order to match the pulse duration of pump ($\approx 1\,\mathrm{ps}$), it is necessary to temporally stretch the signal pulse ($\approx 0.7\,\mathrm{ps}$). e.g. by propagation in dispersive glasses or chirped mirrors.

2.5 Ultrashort Pulse Diagnostics

2.5.1 Fourier-transform Infrared Spectrometer

Different to commercial spectrometers for the near-infrared and visible spectral range, the MID-IR spectrometers have substantial challenges[13]. First of all, well-performing photodetectors are not easily available in MID-IR spectral range. Some optical devices such as photodiode arrays, which are typically used for data acquisitions, are difficult to make for MID-IR frequences. Second, the emitted thermal radiations from all heat-absorbing objects at room temperature might be in the IR spectral range, causing a strong thermal background noise. In order to suppress the noise, MID-IR detectors have to be cooled down to 77 K with liquid nitrogen. Third, MID-IR radiation is strongly absorbed by common optical glasses (e.g. fused silica, BK7). Therefore, the optical devices and instruments in this range are customized and costly in general.

Based on the above difficulties, our solution is a home-built Fourier-transform infrared spectrometer (FTIR). As shown in Fig.2.4(a), the basic scheme of FTIR is a Michelson interferometer. The input MID-IR pulse splits into two replica pulses by the beam spliter (germanium coating on a 3 mm thick KBr substrate) propagating in two arms; one pulse is reflected back in a fixed beam path, while the length of the second beampath is controlled by a motorized delay stage. After recombination in the beam spliter, the two beams interfere with each other and are recorded by an HgCdTe (mercury cadmium telluride, MCT) detector, which is cooled by liquid nitrogen. A computer programm controls the delay stage, the data acquisition and calculates the MID-IR spectrum from the recorded interferogram according to the following operation principle. The MCT detector's output intensity is determined by the square of the interfered electric field of the two pulses, averaged over one light period T (Diels & Rudolph, 2006, p.65)[8]

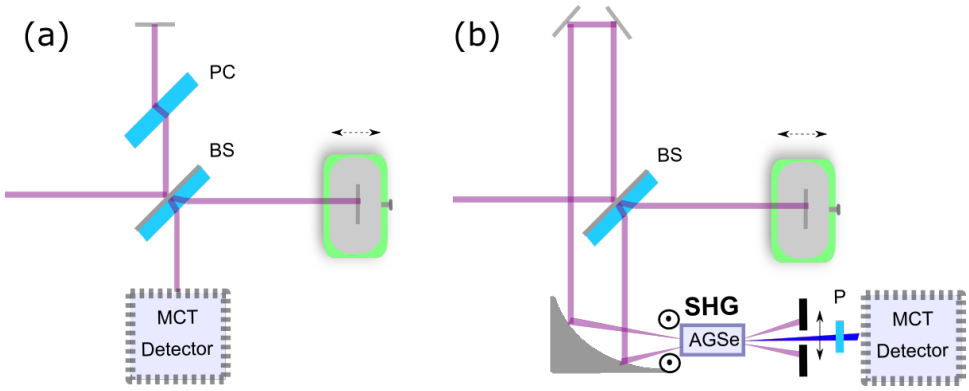

Figure 2.4: Figure (a) the scheme of FTIR. BS: beam spliter, PC: phase compensation. With a little adjustment and installation of the NLC, FTIR can switch to second-order autocorrelation, shown in Figure (b). $AgGaSe_2$ is the NLC used for SHG and the polarizer in front of the MCT detector effectively reduce the noise.

$$\begin{aligned} I(t,\tau) =& \epsilon_0 cn \frac{1}{T} \int_{t-T/2}^{t+T/2} [E_1(t'-\tau) + E_2(t')]^2 dt' \\ =& \frac{1}{2}\epsilon_0 cn \big\{ \mathcal{E}_1^2(t-\tau) + \mathcal{E}_2^2(t) \\ &+ \tilde{\mathcal{E}}_1^*(t-\tau)\tilde{\mathcal{E}}_2(t)\mathrm{e}^{i\omega_\ell \tau} + \tilde{\mathcal{E}}_1(t-\tau)\tilde{\mathcal{E}}_2^*(t)\mathrm{e}^{-i\omega_\ell t} \big\}. \end{aligned} \tag{2.5.1}$$

In realistic conditions, the intensity is averaged over the response time of the detector, which is much longer than the ultrashort pulse duration. Therefore, the measurement can be seen as the time integral $\int_{-\infty}^{\infty} I(t',\tau)dt'$.

$$\begin{aligned} I(\tau) = \frac{1}{4}\epsilon_0 cn \big\{ &\langle \mathcal{E}_1^2 \rangle + \langle \mathcal{E}_2^2 \rangle \\ &+ \int_{-\infty}^{\infty} [\tilde{\mathcal{E}}_1^*(t-\tau)\tilde{\mathcal{E}}_2(t)\mathrm{e}^{i\omega_\ell \tau} + \tilde{\mathcal{E}}_1(t-\tau)\tilde{\mathcal{E}}_2^*(t)\mathrm{e}^{-i\omega_\ell t}] dt \big\} \end{aligned} \tag{2.5.2}$$

The first two averaged terms are the DC-constant of the interferogram, and the time integral part is the oscillation caused by interference. It is worth to note that the time integral is equivalent to a correlation function. Furthermore, the Fourier transform of the correlation of two functions is the product of the Fourier transforms by the convolution theorem. Here, the negative spectral component of the complex electric field can not be measured. Hence, we only deal with the positive spectral component:

$$\begin{aligned} A_{12}(\omega) = \mathcal{F}[A_{12}(\tau)] =& \mathcal{F}[\int_{-\infty}^{\infty} \tilde{\mathcal{E}}_1^*(t-\tau)\tilde{\mathcal{E}}_2(t)\mathrm{e}^{i\omega_\ell \tau} dt] \\ =& \frac{1}{4}\tilde{\mathcal{E}}_1^*(\omega-\omega_\ell)\tilde{\mathcal{E}}_2(\omega-\omega_\ell) \\ =& \tilde{E}_1(\omega)\tilde{E}_2(\omega) \end{aligned} \tag{2.5.3}$$

For an ideal interferometer, the output from the two arms are identical, $\tilde{E}_1(\omega) = \tilde{E}_2(\omega)$, and the result of Fourier transform is simply the spectral intensity of the light, which is given by Eq.2.1.14.

2.5.2 Intensity Autocorrelator

In general, the principle of temporal diagnosis is always that a faster timer measures a slower event. If the event itself is a ultrashort pulse (femtosecond = 10^{-15} s, attosecond = 10^{-18} s) , what is the faster timer for the measurement? The answer is the autocorrelator, i.e. an ultrashort pulse can be used to measure its duration.

As shown in Fig.2.4(b), the working principle of an autocorrelator is the following: the MID-IR pulse is split into two delayed replicas in a Michelson interferometer, both replicas are focused by an off-axis parabolic mirror and spatially overlapped inside a 0.1 mm $AgGaSe_2$ (AGSe) crystal (type I phase-matching in the XY plane, $\theta = 44.2°$; $\phi = 45°$). The intensity of second-harmonic generation is recorded as a function of the delay. When both replicas have better temporal overlap inside the crystal, the second harmonic signal becomes higher. Due to the thin thickness of AGSe, the signal is typically week. Thanks to the polarization of SHG being perpendicular to two replicas, a polarizer before the MCT detector acts as a short-pass filter and increase the signal-to-noise ratio significantly. The intensity recorded by the MCT detector is given by

$$I_{AC}(\tau) = \int_{-\infty}^{\infty} I_{\mathrm{SHG}}(t,\tau)dt = \int_{-\infty}^{\infty} \hat{\chi}^{(2)} I_1(t) I_2(t-\tau)dt. \tag{2.5.4}$$

In the ideal case, the intensities of two replicas are identical, so the output result is an intensity autocorrelation. Because of the simple implementation, intensity autocorrelation is a widely used diagnostic technique and the first choice to measure a pulse duration.

However, there are some limitations in the information content of intensity autocorrelation measurements. First, it provides little information about

the pulse shape. Because autocorrelation is always a symmetric function in time domain, its deconvolution could be an infinite number of symmetric and asymmetric pulse shapes. Second, it does not provide any phase information of the pulse. Third, to estimate the pulse duration from the recorded autocorrelation trace, one has to make an assumption on the pulse shape. The most widely used pulse shapes are a sech^2 or a Gaussian function. The determination of the pulse duration in the reconstruction makes use of the known ratio between the FWHM of the measurement and that of the pulse.

2.5.3 Interferometric Autocorrelator

For coping with the limitations of intensity autocorrelation measurements, interferometric autocorrelation is implemented for providing more information about the MID-IR pulses. The only difference in the interferometric setup is the collinear beam path of the two replica pulses after beam combination. By detecting the second-harmonic generation and filtering the fundamental, the detected intensity is proportional to (Diels & Rudolph, 2006, p.458-464)[8]:

$$A(\tau) = A_0(\tau) + Re[A_1(\tau)e^{-i\omega_\ell \tau}] + Re[A_2(\tau)e^{-i2\omega_\ell \tau}], \tag{2.5.5}$$

where

$$A_0(\tau) = \int_{-\infty}^{\infty} [\tilde{\mathcal{E}}_1^4(t-\tau) + \tilde{\mathcal{E}}_2^4(t) + 4\tilde{\mathcal{E}}_1^2(t-\tau)\tilde{\mathcal{E}}_2^2(t)]dt \tag{2.5.6}$$

$$A_1(\tau) = 4\int_{-\infty}^{\infty} \tilde{\mathcal{E}}_1(t-\tau)\tilde{\mathcal{E}}_2(t)[\tilde{\mathcal{E}}_1^2(t-\tau) + \tilde{\mathcal{E}}_2^2(t)]\mathrm{e}^{i[\phi_1(t-\tau)-\phi_2(t)]}dt \tag{2.5.7}$$

$$A_2(\tau) = 2\int_{-\infty}^{\infty} \tilde{\mathcal{E}}_1^2(t-\tau)\tilde{\mathcal{E}}_2^2(t)\mathrm{e}^{2i[\phi_1(t-\tau)-\phi_2(t)]}dt. \tag{2.5.8}$$

The three contributions of detected signal are at three different frequencies. Typically, only the DC-term $\mathrm{A}_0(\tau)$ will be measured, because the detector works as a low-frequency pass filter. According to Eq.2.5.6, the result is composed of a background and the intensity autocorrelation described by Eq.2.5.4. The terms A_0, A_1, and A_2 can be determined from experimental data through the application of the Fourier transform. Besides, the components $\mathrm{A}_1(\tau)$ and $\mathrm{A}_2(\tau)$ contain phase terms ϕ_1(t-τ)-ϕ_2(t), so the information of linearly chirped pulses can be accessed.

Let us discuss more details in the above equations for the cross-correlation, where both fields $\mathcal{E}_1$ and $\mathcal{E}_2$ are equal to $\mathcal{E}$. When τ is equal to 0, the maximum value of the function $\mathrm{A}(\tau = 0)$ is calculated as $16\int_{-\infty}^{\infty} \mathcal{E}^4(\mathrm{t})\mathrm{dt}$. For

large delay τ in comparison to the duration of the pulse, terms involving E(t-τ)E(t) in the cross products become negligible, resulting in a residual value of A($\tau = \infty$) equal to $2\int_{-\infty}^{\infty} \mathcal{E}^4(\mathrm{t})\mathrm{dt}$. Consequently, the ratio of the peak value to the background value for the interferometric autocorrelation is 8 to 1. Furthermore, the DC component $\mathrm{A}_0(\tau)$ represents an intensity autocorrelation and exhibits a peak to background ratio of 3 to 1.

The interferometric autocorrelator utilized in this study is a commercially available system (APE autocorrelator). The specific model employed has the capability to assess pulse durations ranging from less than 5 fs to 500 ps within the wavelength range from 7 to 12 µm. The detection technology is based on two photon absorption (TPA)[14].

2.6 Vibrational Sum-frequency Generation

Vibrational sum-frequency generation (VSFG) spectroscopy is a nonlinear optical technique that involves the combination of infrared (ω_{IR}) and visible (ω_{VIS}) beams to produce a new electromagnetic wave whose frequency is the sum of the frequencies of the two input beams, denoted as $\omega_{\mathrm{SFG}} = \omega_{\mathrm{IR}} + \omega_{\mathrm{VIS}}$. The process of VSFG is illustrated in Fig.2.5. When the frequency of the infrared beam ω_{IR} excites a vibrational transition within a molecule and the visible beam ω_{VIS} interacts with the vibration as it decays back to its ground state, enabling the extraction of vibrational information by detecting the emitted photons from the molecule at the frequency ω_{SFG}. Unlike conventional linear spectroscopic methods such as infrared and Raman spectroscopy, VSFG is only observable in a medium where centrosymmetry is broken. Interfaces between two centrosymmetric or disordered phases satisfy this noncentrosymmetry criterion, such as surfaces, interfaces and monolayer molecules, making SFG a valuable technique for surface-specific vibrational analysis.

The principle of VSFG is based on the SFG term in Eq.2.2.3, so a general form expressing the VSFG intensity can be written as[16]

$$\begin{aligned} I_{\mathrm{SFG}} \propto & |\tilde{\mathbf{P}}(\omega_{\mathrm{SFG}})|^2 \\ \propto & |\chi^{(2)}_{\mathrm{NR}} + \sum_q \chi^{(2)}_{\mathrm{R}q} \mathrm{e}^{i\gamma_q} + \chi^{(3)} \mathrm{E}_{\mathrm{DC}}|^2 \mathrm{sinc}^2\Big(\frac{L\Delta\mathbf{k}}{2}\Big) L^2 I_{\mathrm{VIS}} I_{\mathrm{IR}}. \end{aligned} \tag{2.6.1}$$

In Eq.2.6.1 $\chi^{(2)}_{\mathrm{NR}}$ and $\chi^{(2)}_{Rq}$present the nonresonant and resonant part of the surface nonlinear susceptibility, and γ_q is the relative phase of the q_{th} vibrational mode characterized by bond-specific vibrational states ν. In

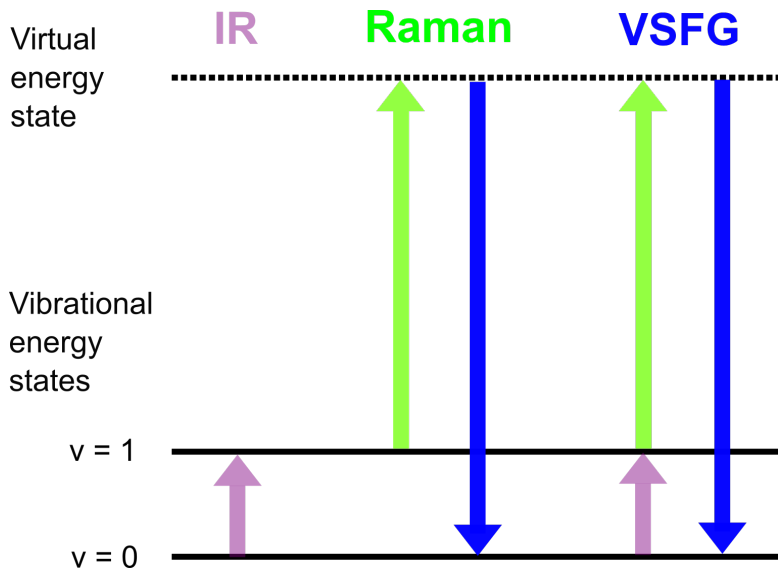

Figure 2.5: Illustration of vibrational sum-frequency generation (VSFG) with contributions arising from IR absorption of vibrational modes characterized by bond-specific vibrational energy states $\nu = 0, 1.$ (horizontal lines) and Raman scattering from a virtual energy state of the molecule (horizontal dotted line). Adapted with permission from [15].

some cases, third-order contributions $\chi^{(3)}$ will also show up, if there is a net electrical field E_{DC} within the system of interest, e.g., ionic species adsorb at the water surface[17]. The component involving the sinc function is the synchronization factor, which accounts for the phase matching between the incoming and SFG beams ($\Delta\mathbf{k} = \mathbf{k}_{SFG} - \mathbf{k}_{VIS} - \mathbf{k}_{IR}$) in the specified dimension (L) as they propagate through the sample.

In experiments, the enhancement in the SFG responses can be observed when the frequency of infrared radiation is resonant with sum-frequency active vibrations. Moreover, VSFG can be viewed as a combination of a resonant infrared transition with a nonresonant Raman transition, based on the energy-level diagram in Fig.2.5[18]. In other words, the generation of a VSFG signal primarily depends on infrared activity, while Raman activity (polarizability change) acts as an enhancement factor but is not a necessary condition.Therefore, a rank-3 tensor $\chi^{(2)}_{Rq}$, which is a direct product of the Raman transition polarizability $\alpha_{i,j}$ and the IR transition dipole moment μ_k with a Lorentzian function can be defined as:

$$\chi^{(2)}_{\mathrm{R}q\mathrm{i,j,k}} \propto \frac{\alpha_{\mathrm{i,j}} \cdot \mu_{\mathrm{k}}}{\omega_q - \omega_{\mathrm{IR}} - i\Gamma_q}, \tag{2.6.2}$$

where the vibration is mathematically described with the resonant frequency ω_q and the natural line width of the transition Γ_q.

Lambert et al.[19] extensively discussed various tensor elements examined through different polarization combinations. In the context of VSFG spectroscopy, spectra are commonly denoted with polarization combinations like "PPP," "SSP," or "SPS," indicating the polarizations of the three beams in decreasing frequency order. For instance, SSP signifies that the SF and VIS light are S-polarized, while the IR light is P-polarized. Among the eight potential combinations, only four are relevant when detecting a VSFG signal from a molecule: PPP, SSP, SPS, and PSS.

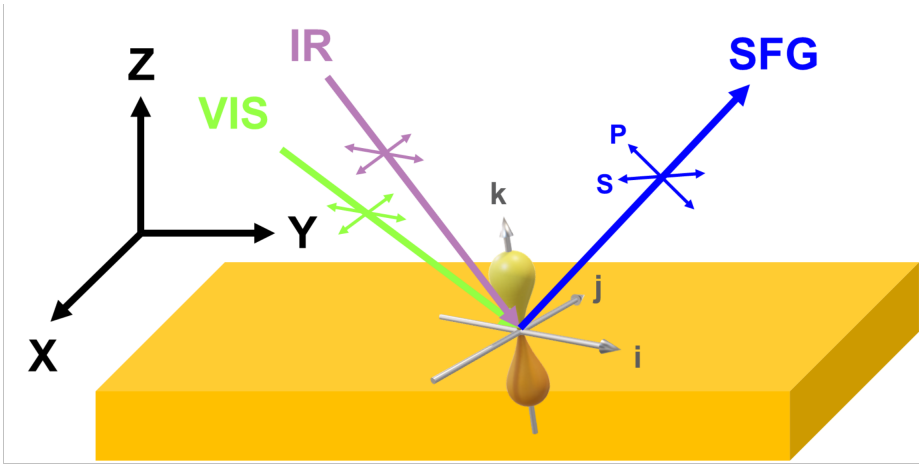

Figure 2.6: An illustration of a VSFG experimental setup with the IR beam in purple, the VIS beam in green, and the SFG beam in blue. The laboratory and molecular frames are represented in black and gray, respectively, with the surface plane as the XY-plane and the incidence plane as the XZ-plane. The linear polarization orientations of each beam (S or P) are indicated by colored double-headed arrows. A molecule positioned at an angle to the surface is displayed. Reflected IR and VIS beams are omitted for clarity.

At a microscopic level, the $\chi^{(2)}_{Rq}$ tensor is derived from a molecular (i, j, k) frame coordinate system that is transformed into the laboratory (X, Y, Z) frame, as illustrated in Fig.2.6. The orientation of a molecule relative to the surface, which is the angle between these frames, influences the values of the individual elements of the $\chi^{(2)}_{Rq}$ tensor. Consequently, VSFG is inherently sensitive to the alignment of molecules and molecular groups with respect to the surface. Examining the angle dependence of specific tensor elements can aid in the analysis of the orientations of molecules or specific molecular groups in relation to the surface.

From the perspective of experiment, the selection of appropriate angles of incidence for the IR and VIS beams is crucial for optimizing the SFG signal through the maximization of the so-called Fresnel factors. These factors, also known as "local field-correction factors," are significantly influenced by the incident angles. Typically, angles ranging between 40° and 60° are found to have good results across a wide range of samples and wavelengths. However, it is advisable to compute the Fresnel factors tailored to the specific experimental conditions. By utilizing the equations derived by Zhuang et al.[20] and the Python script written by Pickering et al.[21, 22], the relevant Fresnel factors as a function of incident angle for the most common polarization combinations (SSP, SPS, PSS, and PPP) are plotted in Fig.2.7.

In our setup, the wave-mixing of broadband MID-IR (from 900 to 2500 cm^{-1}) and visible (515 nm) up-converts the molecular vibrations into the visible range (from 480 to 492 nm) for detection. Therefore, the incident angle of VIS and MID-IR are aligned at 53° and 45° respectively, and the combination of SFG, VIS and MID-IR are at SSP polarization.

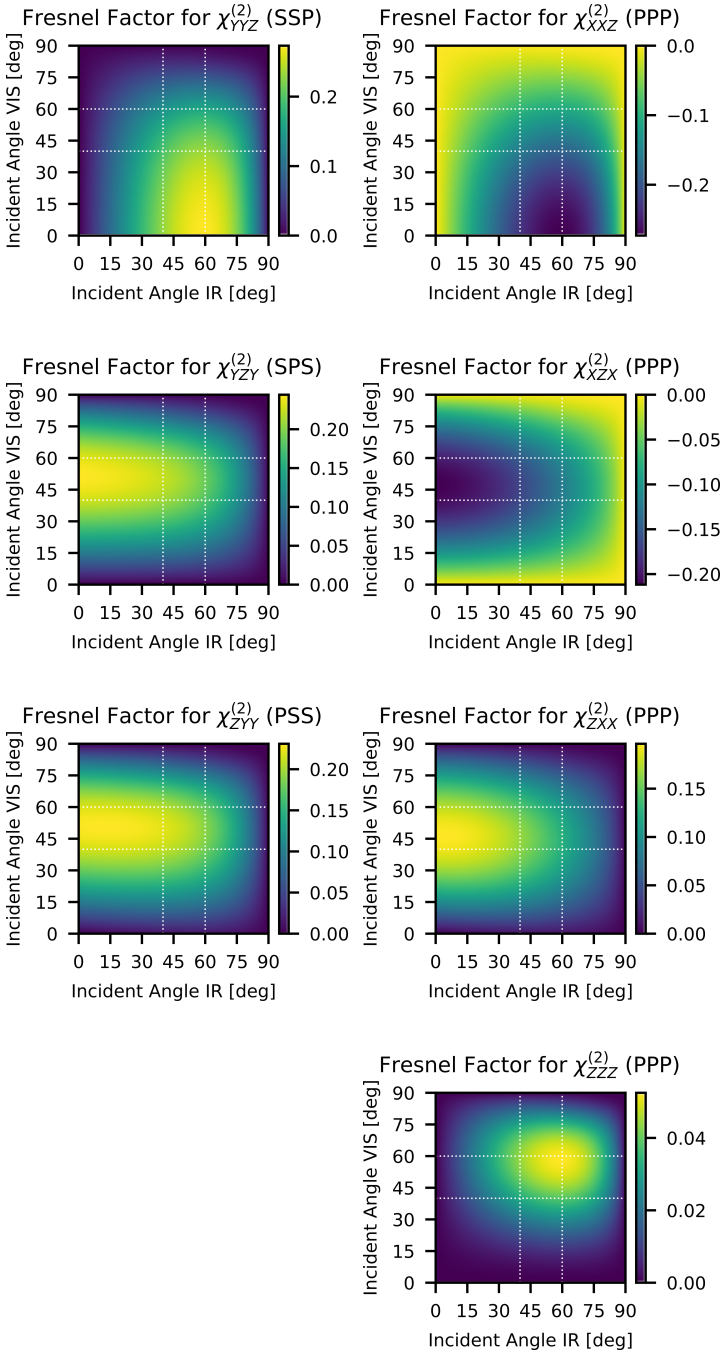

Figure 2.7: Fresnel factors for the tensor elements probed in the most common SFG polarization combinations as a function of IR and VIS incident angles, for a typical air-water interface as applied in the present research project. The area between the white dashed lines illustrates the angles commonly used in VSFG instruments.

Chapter 3

Optical Properties of Nonlinear Crystals

3.1 Motivation

Mid-infrared optical parametric chirped-pulse amplification (MID-IR OPCPA) laser systems, which operate at wavelengths above 5 µm and generate short pulses at high repetition rates and power levels, are of significant interest. Some applications of MID-IR OPCPA like vibrational spectroscopy, label-free microscopy, and ultrafast dynamic studies[23] are promising to effectively observe and manipulate matter, materials, and biological samples. This desire is pushing advancements in both MID-IR laser technologies and advanced laser pulse shaping capabilities within this spectral range[24].

By the impressive power scalability of 1 µm Ytterbium (Yb) pump lasers, optical parametric amplifiers (OPAs) operating between 3 and 4 µm have been developed, enabling the generation of femtosecond laser pulses at multi-MHz rates with power outputs in the multiple-watt range[25, 26, 27, 28, 29, 30]. These systems utilize wide-bandgap oxide crystals for parametric frequency down-conversion, which are available commercially in sizes larger than 1 cm. Various nonlinear optical materials, such as $LiNbO_3$, $KNbO_3$, and $KTiOAsO_4$, can be successfully pumped by high-power lasers with short pulses (< 1.5 ps) at 1 µm, showing minimal two-photon absorption and high damage thresholds[31, 32]. However, due to the high multi-photon absorption by oxide crystals in the spectral range above 5 µm, an OPA-DFG cascade must be extended to the longer mid-infrared range. In such laser setups, the OPA stages use oxide crystals, while the DFG stage employs non-oxide semiconductor crystals like $AgGaSe_2$[33, 34], GaSe [24, 35, 36, 37], $AgGaS_2$[38, 39], $CdSiP_2$[40] and $ZnGeP_2$[41, 42, 43]. However, these crystals have relatively

small bandgaps around 2.4 eV, which is very close to the two-photon energy of high-power commercial Yb pump lasers, making efficient DFG processes at 1 µm challenging[44].

Typically, the energy conversion efficiency from pump to MID-IR in OPA/DFG cascades is usually less than 0.5 % at a central wavelength of approximately 8 µm. The improvement of efficiency relies on the availability of novel non-oxide Li-based materials like $LiGaS_2$ (LGS), $LiGaSe_2$ (LGSe), $LiInS_2$ (LIS), and $LiInSe_2$ (LISe) that are transparent across a wide spectral range (from 6 to 16 µm) and have high damage thresholds. Combined with high-power 1 µm Yb pump lasers, this advancement enables the extension of ultrashort high-power laser pulses for various R&D projects, and industrial applications towards the longer-wave infrared (LWIR) region. Some progress has been achieved by using LGS crystals, which show transparency from 0.32 to 11.61 µm and a large bandgap of around 4 eV. Notably, ultrashort pulses at the nanojoule level with pulse durations close to the Fourier-transform limit at central wavelengths spanning from 7 to 11 µm have been successfully demonstrated in OPA[45, 46, 47], DFG[35], and intra-pulse DFG laser systems[29, 48, 49].

For increasing the pulse energy and average power of LGS-based MID-IR lasers in DFG and OPA schemes, the size and length of the LGS crystal play a role, having the current limitation of crystal aperture size ($\approx 7 \times 7\,\mathrm{mm}^2$) and length (≈ 5–7 mm), respectively. The higher pulse energies beyond 100 µJ and watt-level average power could be achieved by utilizing longer crystals (several mm) and pump pulse widths (≈ 10 ps)[23]. However, the damage threshold of LGS at peak intensity, approximately $50\,\mathrm{GW/cm}^2$, becomes a critical factor[45]. Managing thermal loads when pumping at 1 µm with ultrashort pulses at MHz repetition rates is crucial to prevent spatially inhomogeneous refractive index changes that can affect phase-matching conditions, average power, spectral bandwidth, beam quality, and long-term performance stability. Therefore, a thorough understanding of the optical properties of converter materials under realistic high-power and high-energy conditions is essential for designing robust MID-IR laser architectures[50]. Nonetheless, studies on material properties related to ultrafast laser-induced damage in nonlinear crystals above a few kHz repetition rates are rare[51].

In the present thesis project, a straightforward thermal imaging technique offers a reliable estimation of the linear and nonlinear absorption coefficients, as well as the nonlinear refractive index, "under realistic conditions"[52]. This approach involves measuring material parameters using laser pump settings consistent with those intended for high-power and high-energy OPCPA applications. Specifically, a high-power laser is directed at the entire surface area of a large crystal with an aperture of approximately $9 \times 9\,\mathrm{mm}^2$. These

measurements provide more accurate estimation of absorption and nonlinear coefficients by averaging over large crystals that may contain local defects, impurities, and surface irregularities. Consequently, the thermal imaging method provides more realistic upper limits compared to techniques that focus on localized measurements within small perfect crystals[52]. In contrast, the widely-used photothermal common-path interferometry (PCI) method[53] primarily determines linear absorption within the crystal volume with high precision using a low-power continuous wave laser, but the multi-photon absorption coefficient can not be obtained. Furthermore, the z-scan method, pioneered by van Stryland and co-workers[54] in 1990, accurately determines the nonlinear refractive index n_2 within a limited volume of the crystal.

3.2 Thermal Imaging Scheme

For the current investigation, a selection of non-oxide nonlinear crystals (NLC) is analyzed to derive their linear and two-photon absorption coefficients, as well as the nonlinear refractive index at 1030 nm by utilizing a commercial AMPHOS laser system, which is based on the Innoslab amplifier technology[56]. Fig.3.1 shows the basic design of the Innoslab amplifier. It consists of two key components: an edge pumped slab crystal inside the amplifier resonator. In edge pumping geometry, pump and signal intensity can overlap along the whole slab, which leads to high intrinsic efficiency. The resonator

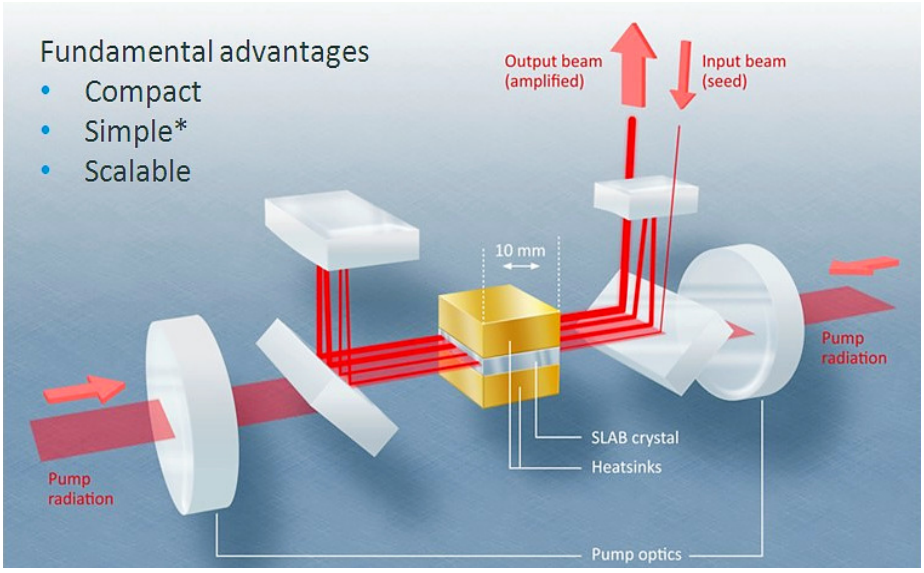

Figure 3.1: AMPHOS innoslab laser. Adapted from [55]

folds the laser beam several times through the pumped slab, largely reducing the thermal lensing effect. Besides, the large surfaces provide one-dimensional heat flow, which is efficient for heat removal by heat sinks. The scalability of the output power can be easily achieved by increasing the crystal width without increasing the demand on brightness of the pump diodes. This laser system generates pulses with a full width at half maximum (FWHM) duration of $\tau = 0.92\,\text{ps}$, centered at $\lambda_o = 1030\,\text{nm}$ with a spectral bandwidth of approximately 1.1 nm, $M^2 < 1.3$, and offering a tunable repetition rate ranging from 200 kHz to 1 MHz. Comparable average power levels can be achieved at both repetition rates, with a maximum output power of $P = 200 \pm 2\,\text{W}$.

The experimental configuration is illustrated in Fig.3.2. The NLCs are positioned on ceramic stands in such a way that only the bottom corners contact with the crystals, and they are secured from the top by a nylon tip screw. This setup makes sure that all surfaces of the crystals are exposed to ambient airflow, minimizing thermal conduction to the holder. The "free standing" NLCs are exposed to the AMPHOS laser beam under the realistic conditions. The experiments are carried out at repetition rates of 1 MHz and 200 kHz, respectively. By using a half-wave plate and polarizer, the average power at each repetition rate can be adjusted. The laser beam sizes are consistent in both scenarios (with $1/e^2$ radius $\omega = 2.1\,\text{mm}$), tailored to fill the entire crystal aperture ($9 \times 9\,\text{mm}^2$) to achieve uniform heat distribution across the crystal. The NLCs, which are studied in this scheme, includes LGS (type II-XY plane, $\theta = 90°; \phi = 37.5°$), LGSe (type II-XY plane, $\theta = 90°; \phi = 33.5°$), LIS (type II-XY plane, $\theta = 90°; \phi = 31.5°$), LISe (type II-XY plane, $\theta = 90°; \phi = 33.0°$) and AGS (type II-XY plane, $\theta = 90°; \phi = 39.5°$) crystals, each 2 mm thick (Ascut Ltd. & Co.KG)[50]. The crystals are uncoated on both sides, and the cut angle is chosen for 10 μm idler wavelength when pumped at 1030 nm.

All measurements were conducted with the pump laser in "e" polarization. The power inside the crystal and Fresnel reflections at the front and back surfaces were estimated by measuring the reflected and transmitted pump laser powers, resulting in a 13.4 % reduction in total power. The beam profile of the transmitted beam was monitored using a Basler camera (Basler Aca 1300gm) by reflecting a small portion of it with a wedge. Thermal equilibrium thermal images of the crystals were captured using an IR camera (FLUKE Ti25, spectral range from 7.5 to 14 μm. An illustrative example of the heat distribution in a pumped crystal is shown in Fig.3.2 (bottom, left).

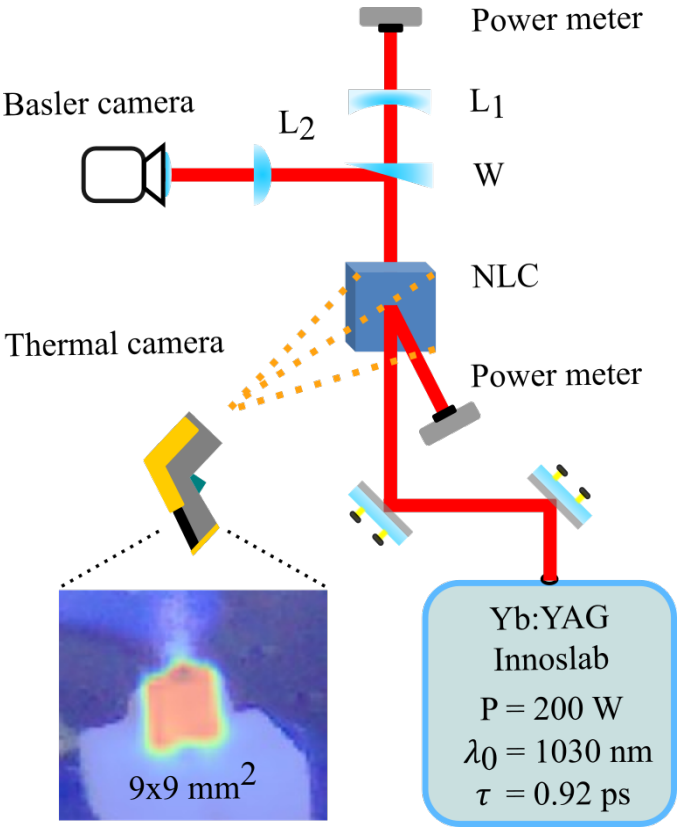

Figure 3.2: Experimental setup for thermal imaging. The NLCs utilized in the study are $9\times9\times2\,\mathrm{mm}^3$ in size and positioned in a "free-standing" configuration. Power meters are employed to approximate the power contained within the crystal and validate the expected Fresnel reflections at the front and back surfaces. Thermal imaging is conducted to assess the temperature distribution over the crystal surfaces. An illustrative thermal image captured by the thermal camera is presented in the lower left section. Additionally, a Basler camera is utilized to capture beam profiles that are altered by the nonlinear behavior of the NLCs. Adapted with permission from[57].

3.3 Results and Discussion

3.3.1 Linear and Nonlinear Absorption Coefficients

The main limitations to increasing the average power levels of OPCPAs are the thermal effects caused by the absorption of pump, signal, and idler pulses in NLCs. In the case of MID-IR OPCPAs (ranging from 6 to 16 µm), the relatively low conversion efficiency suggests minimal absorption of the idler pulse, while the absorption effects of the signal wavelengths are expected

to be similar to those of the pump wavelength. Therefore, the thermal equilibrium of the crystals should be mainly influenced by the pump pulse[52, 58]. A thermal model is utilized under thermal equilibrium to calculate the linear and nonlinear absorption coefficients, using established laser and material parameters, with the absorption coefficients α (linear) and β (multi-photon) as variables. The heat equation is developed by considering energy transfer during laser interaction, taking into account black body radiation and convection under thermal equilibrium[52, 59]. This method is considered suitable for high repetition rate Yb pump lasers, as the thermal relaxation time significantly surpasses the time between successive pulses. Essentially, the thermal model assumes that the absorbed laser power P_{abs} can be represented as[60]

$$P_{\text{abs}} = C_1\alpha I + C_2\beta I^2, \tag{3.3.1}$$

is re-emitted. Thus, total heat H exchanged is given by

$$H = H_{\text{black-body}} + H_{\text{convection}} = \sigma\epsilon A(T_{\text{C}}^4 - T_{\text{R}}^4) + hA(T_{\text{C}} - T_{\text{R}}) \tag{3.3.2}$$

which finally results in

$$\sigma\epsilon A(T_{\text{C}}^4 - T_{\text{R}}^4) + hA(T_{\text{C}} - T_{\text{R}}) = C_1\alpha I + C_2\beta I^2. \tag{3.3.3}$$

The thermal energy emitted through black-body radiation is influenced by the Stefan-Boltzmann constant ($\sigma = 5.669\times10^{-8}\,\text{W m}^{-2}\text{K}^{-4}$)[59]. The surface emissivity of the crystals are calibrated against a thermal reference, because the transparency range of the thermal camera is falling in the transmission window of the MID-IR NLCs. In the case of LGS, the emissivity value $\epsilon_{\text{LGS}} = 0.6$, while for other crystals, the values are as follows: $\epsilon_{\text{AGS}} = 0.37$, $\epsilon_{\text{LGSe}} = 0.42$, $\epsilon_{\text{LIS}} = 0.6$ and $\epsilon_{\text{LISe}} = 0.44$. Parameters such as the crystal's surface area A, crystal temperature T_{C} , room temperature T_{R}, and a typical heat convection coefficient $h = 10\,\text{Wm}^{-2}\text{K}^{-1}$ as reported in literature[59] are considered. The coefficients C_1 and C_2 are determined by the laser pulse characteristics, including the repetition rate f, radial beam waists $\omega_{\text{x}}\omega_{\text{y}}$ perpendicular to the propagation direction, pulse duration τ, and crystal length L. The integration of the squared hyperbolic secant (sech) function representing the pulse shape is performed to derive the final results

$$\begin{aligned} C_1 &= fL(1.206\omega_{\text{x}}\omega_{\text{y}}\tau) \\ C_2 &= fL(0.426\omega_{\text{x}}\omega_{\text{y}}\tau). \end{aligned} \tag{3.3.4}$$

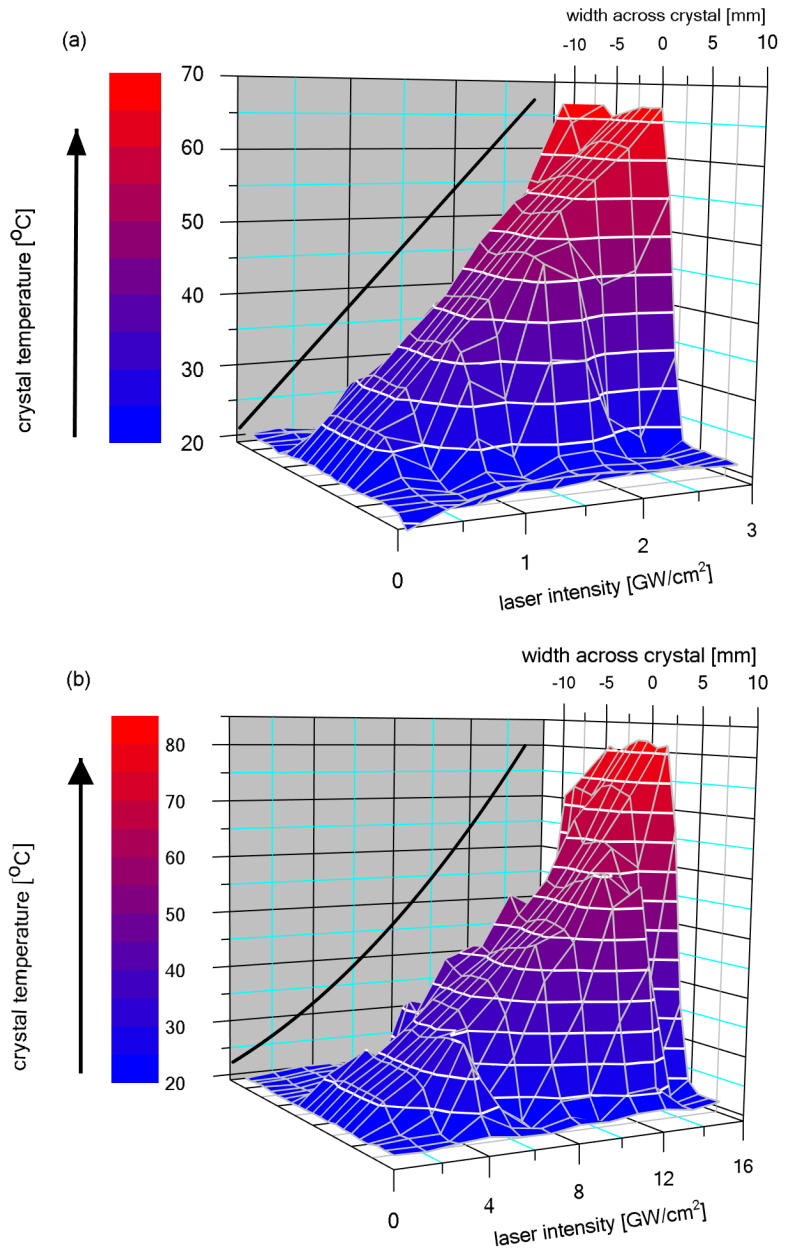

Figure 3.3: An illustrative temperature profile was obtained utilizing the LGS crystal, derived from thermal imaging data captured by progressively increasing the irradiation power levels within the crystal at repetition rates of 1 MHz (a) and 200 kHz (b). The black line depicts the average temperature distribution throughout the crystal relative to the laser intensity. Adapted with permission from[57]

The figure presented in Fig.3.3 illustrates the change in average temperature across the surface of the crystal as the pump laser intensity increases, specifically focusing on the LGS crystal. The temperature is obtained from the central region of the crystal aperture in the thermal image. The experiments are conducted at repetition rates of 1 MHz and 200 kHz, respectively. The average power within the crystal is calculated by considering losses from Fresnel reflections, which are measured by analyzing the reflected power from the crystal surfaces. The pulse duration and spatial beam profiles are similar in both experimental sessions. When analyzing data at high repetition rates of 1 MHz with lower pulse energies, linear absorption played a larger role, while at 200 kHz with higher pulse energies, nonlinear absorption is more dominant, as depicted in Fig.3.4. This pattern is consistent across all non-oxide NLCs, except for LGSe, where strong multi-photon absorption is obvious even at low energy per pulse at 1 MHz. By evaluating the total heat as a function of pump laser intensity from the recorded thermal images and fitting the data according to Eq.3.3.3, approximate values of the linear and nonlinear absorption coefficients are obtained for various NLCs. The linear absorption coefficient α is determined through a linear fit of the 1 MHz data, which is then utilized in a nonlinear curve fit of the 200 kHz data to derive the nonlinear absorption coefficient β. Independent measure of α enhances the accuracy of the fitting process for estimating β. An illustration of the data analysis for the LGS crystal is provided in Fig.3.4.

The estimated values of the linear and nonlinear absorption coefficients for different crystals are presented in Tab.3.1, with the bandgap and d_{eff} values sourced from references [61] and [62], respectively. The fitting error across all graphs is below 0.2 %. Nevertheless, it is important to mention that systematic errors usually result in an overestimation of values when using these methods[52]. Therefore, all experimentally obtained values are presented as upper limits.

Additionally, in the case of non-oxide NLCs, the generation of second-harmonic "green" light and increased lensing effects at high intensities are observed, although these effects are deemed negligible for the analysis conducted in this study. Notably, the AGS crystal exhibited a significant Kerr-lensing effect at an average power of 45 W, evident in both the 1 MHz and 200 kHz datasets, corresponding to peak intensities of approximately 0.8 GW/cm^2 and 4.2 GW/cm^2, respectively. Consequently, experiments on AGS are not extended to higher power levels to prevent crystal damage. A similar trend was observed with LISe. In the case of the AGS crystal, a linear increase in temperature is the predominant observation for both repetition rates within experimental error margins. Hence, only the linear absorption coefficient is determined for AGS.

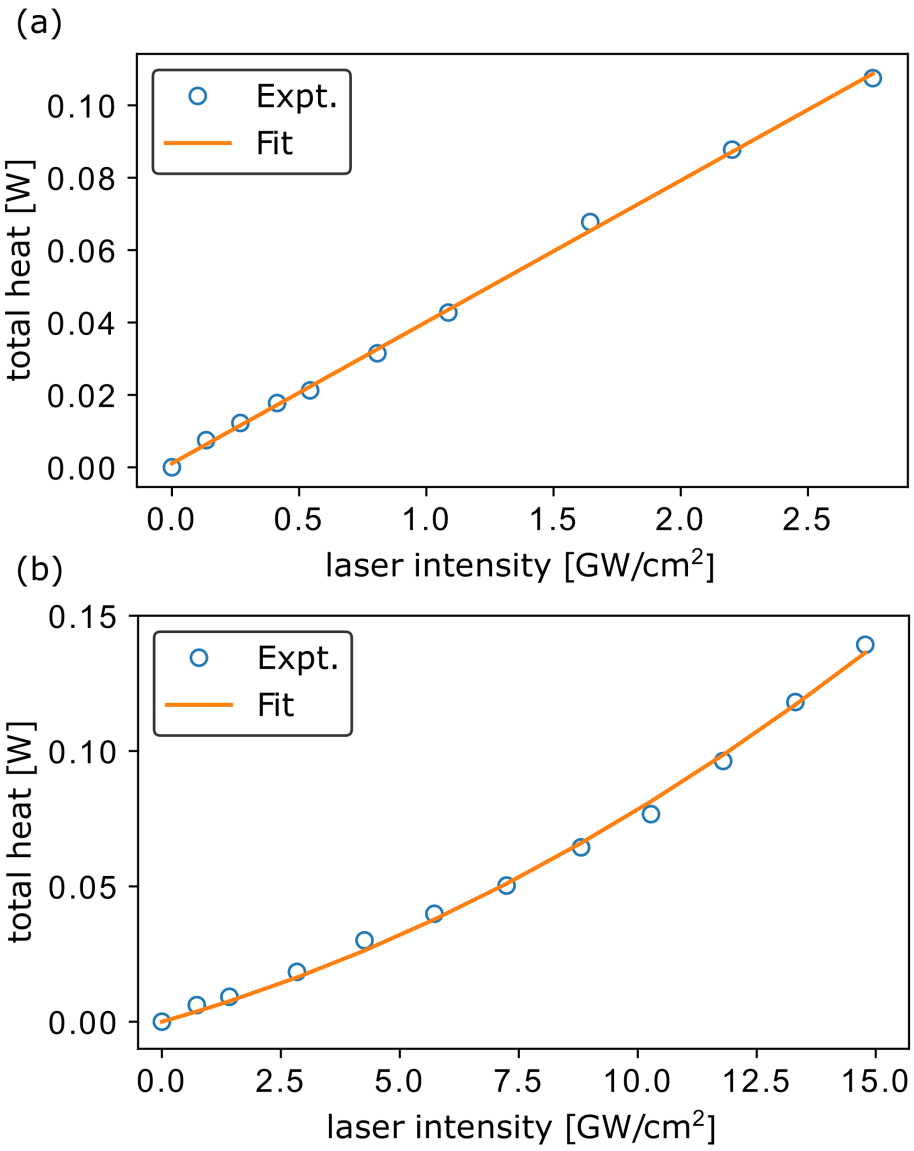

Figure 3.4: A linear curve fitting was performed at 1 MHz (a), while a nonlinear curve fitting was conducted at 200 kHz (b) to determine the linear and nonlinear absorption coefficients based on the analytical model correlating total heat with intensity for the LGS crystal. Reproduced with permission from

3.3.2 Nonlinear Refractive Index

In this section, a straightforward and reliable approach is presented for estimating the upper limit of the second-order nonlinear refractive index n_2 of NLCs. The approach are under realistic high-power user conditions and beam

			derived constants for 1030 nm wavelength		
nonlinear crystal	Bandgap[61] [eV]	d_{eff}[62] [pm/V]	α [cm^{-1}]	β [cm/GW]	n_2 [cm^2/W]
$AgGaSe_2$ (AGS)	2.70	15.9	<0.005	-	$< 140.6\times10^{-15}$
$LiGaS_2$ (LGS)	4.15	5.60	<0.002	$<3.2\times10^{-4}$	$< 6.4\times10^{-15}$
$LiGaSe_2$ (LGSe)	3.34	9.27	<0.002	$<2.0\times10^{-3}$	$< 27.4\times10^{-15}$
$LiInS_2$ (LIS)	3.57	6.90	<0.001	$<2.6\times10^{-4}$	$< 9.4\times10^{-15}$
$LiInSe_2$ (LISe)	2.86	9.48	<0.01	$<1.6\times10^{-3}$	$< 16.2\times10^{-15}$

Table 3.1: Optical properties of MID-IR non-oxide, Li-based nonlinear crystals. Adapted with permission from[57].

parameters, based on beam profile measurements after traversing the crystal. It is important to note that an effective n_2 can be influenced by cascaded second-order effects and Kerr lensing[63, 64], which are significant factors in the design of OPCPA systems. To validate our measurements, we selected uncoated LGS as the sample material due to its recently reported effective n_2 values of $3.5 \times 10^{-15}\,cm^2/W$[45] and $4.1 \times 10^{-15}\,cm^2/W$[51] under high-power 1 µm pumping. The z-scan method, initially introduced by van Stryland and colleagues in 1990[54], is employed for this purpose.

The Basler camera captures images after the beam has passed through the "free-standing" NLC and is projected into the camera using a wedge (W) and a lens (L_2) with a focal length of 400 mm as depicted in Fig.3.2. The results for the LGS crystal are illustrated in Fig.3.5. At 1 MHz, characterized by relatively low intensity, the beam profiles exhibit consistency with and without the NLC crystal, thereby allowing the neglect of thermal lensing effects. However, at 200 kHz, the beam profiles display a reduction in diameter with increasing pump intensity due to Kerr lensing effects. The beam profile measurements are conducted to monitor these phenomena and to detect any potential irreversible damage during the assessment.

According to the electro-optic (Kerr) effect, a Kerr lens is formed with focal length f_K given by

$$f_K = \omega^2/(4n_2IL). \tag{3.3.5}$$

Here, ω is the $1/e^2$ beam radius (determined by the knife-edge method), I describes the peak intensity and L denotes the length of the crystal. As the pump intensity increases, the NLC acts like a lens, causing the original size of the pump profile to decrease. This original pump profile is observed in the

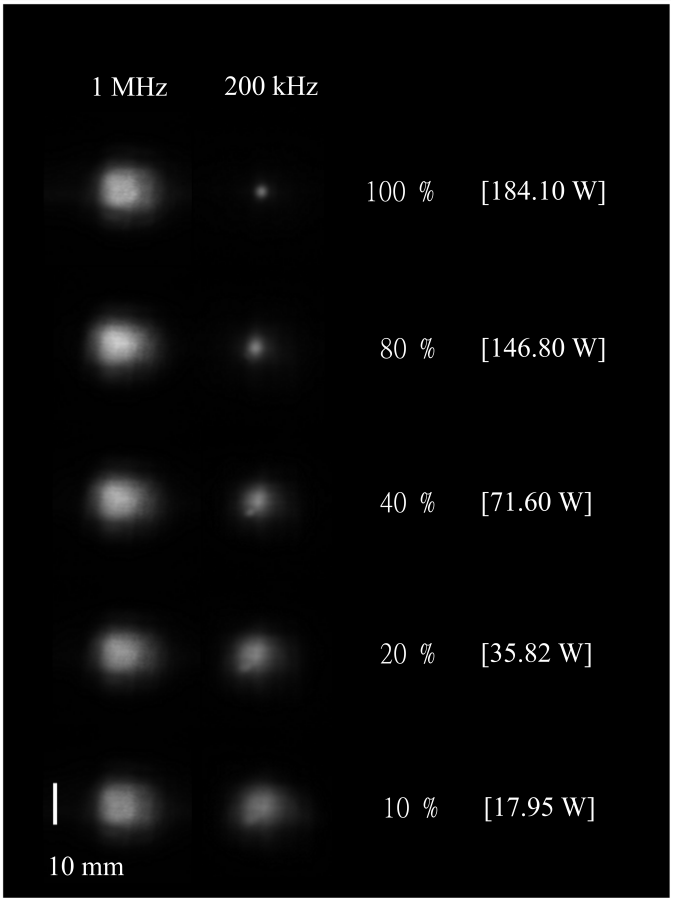

Figure 3.5: Basler camera images are utilized to observe the beam profile of crystal LGS as the pump intensity increased, showcasing a nonlinear response at both 1 MHz and 200 kHz repetition rates. The beam profiles displayed a progression from top to bottom, corresponding to laser pump power levels of 100 %, 80 %, 40 %, 20 %, and 10 % of the total power, with the estimated internal power of the crystal indicated in square brackets. Adapted with permission from[57]

absence of the NLC or at very low intensities. Assuming the propagation of Gaussian beams and known laser, crystal, and imaging optics, the parameter f_K is determined through a comparison of images at different intensities with a simulation of Gaussian beam propagation employing idealized lenses. For the LGS crystal, an upper estimate of the second-order nonlinear refractive index n_2 is provided, which is approximately $6.4 \times 10^{-15}\,cm^2/W$, aligning well with the published results. The calculated n_2 values for other crystals under investigation are presented in Tab.3.1.

In summary, only a limited number of suitable nonlinear crystals are

accessible in the MID-IR range (from 6 to 16 μm). While the widely used AGS crystal exhibits a high d_{eff}, it possesses a lower bandgap and significantly higher nonlinear refractive index (n_2) compared to other Lithium-based crystals when pumped at 1030 nm (refer to Tab.3.1), making it unsuitable for high-energy and power applications. For low-power applications, LIS and LISe show promise due to their relatively high d_{eff}. Conversely, for high-energy and power applications, LGS crystal offers a combination of substantial d_{eff} and a comparatively high optical damage threshold owing to its large bandgap and broad transparency range. Furthermore, LGS demonstrates the lowest multi-photon absorption coefficient and nonlinear refractive index (see Tab.3.1), positioning it as a highly promising candidate among non-oxide NLCs for high-power ultrashort MID-IR OPCPA applications directly pumped at 1030 nm.

Chapter 4

Versatile MID-IR OPCPA

4.1 Motivation

Ultrashort laser pulses, characterized by a limited number of optical cycles within the 6–16 µm spectral range, present numerous research opportunities in the fields of materials and life sciences. The advancement of versatile femtosecond (fs) sources is essential for investigating intricate physical, chemical, and biological processes through sophisticated experimental techniques like 2-dimensional vibrational [65, 66, 67, 68], label-free microscopy[69, 70], nonlinear optics[71, 72], and nonlinear phononics[73]. The ability to stimulate and probe low-energy excitation is crucial for elucidating a wide range of diverse phenomena, spanning from high-temperature superconductivity in solid-state materials to the structure and dynamics of proteins in the liquid phase.

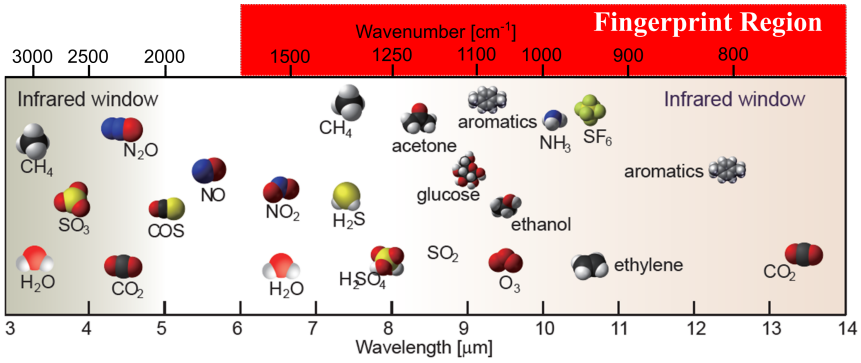

Figure 4.1: Resonant absorption of important biomolecules as a function of wavelength. The region from 6-16 µm is often called the "fingerprint region". Figure adapted from [74]

In the MID-IR wavelength range, numerous essential biomolecules exhibit distinct vibrational absorption bands, commonly referred to as the fingerprint region as illustrated in Fig.4.1. Vibrations such as amide vibrations within the range from 1200 to 1700 cm^{-1}, aromatic breathing, and out-of-plane CH bending modes (occurring in the range from 900 to 1000 cm^{-1}) can be directly probed using wavelength-tunable MID-IR sources [65, 66]. Presently, these vibrational characteristics of biological molecules observed in spectroscopic studies play a crucial role in disease diagnostics, for instance, detecting glucose Raman peaks in people with diabetes[5].

Apart from the well-established one-photon excitations, the high peak power of ultrashort laser pulses with high pulse energy induces nonlinear absorption, leading to the excitation of higher vibrational states through multi-photon processes. These final states may not be accessible using continuous-wave IR sources due to dipole selection rules in single-photon transitions. Moreover, the integration of long-wavelength sources with pulse-shaping capabilities for tailored waveform generation introduces a new dimension to the coherent-control toolbox, primarily aimed at directing photophysical and photochemical processes using light [75, 76, 24]. For example, the enhanced selective excitation of ground-state vibrational modes in the fingerprint region could be utilized to differentiate various cellular components in an image based on their intrinsic vibrations in a non-invasive manner[77]. This concept has been validated through two significant demonstrations in the past. Firstly, MID-IR pulse shaping has been employed to efficiently excite vibrational energy levels in NO molecules through step-wise excitation ("vibrational ladder climbing") using tailored electromagnetic waveforms accounting for the anharmonic molecular potential [78]. Secondly, MID-IR-induced vibrational absorption has been applied in photothermal imaging applications, where the spatially resolved photothermal effect is achieved using a visible laser beam. This approach overcomes the spatial resolution limitations associated with longer-wavelength MID-IR sources, and chemical-specific contrast images are obtained [69].

In recent years, the advancement of novel fs MID-IR laser architectures has been facilitated by two key factors: the availability of nonlinear crystals transparent in the MID-IR range and the development of high-power pump lasers capable of operating at high repetition rates up to 1000 W with sub-picosecond (picosecond = 10^{-12} s) pulse duration. Various research groups globally have contributed to this progress through power-scaling strategies utilizing diverse pump-laser technologies such as fiber[79, 80], thin-disk[81], and Innoslab lasers[82], operating at pump wavelengths of 1 µm and 2 µm[45, 33]. The selection of NLCs that can be effectively pumped at 1 µm plays a key role. As what have been concluded in Chapter3, LGS has emerged as a

preferred choice.

In OPAs, the two primary methods for converting the pump photon into the MID-IR idler involve either intra-pulse or inter-pulse difference-frequency generation (DFG) processes[36]. In the case of intra-pulse DFG, which is driven by pulses possessing a wide spectral bandwidth, the idler is generated through the difference frequency mixing of the blue side (pump for DFG) and red side (signal for DFG) of its spectrum via nonlinear interaction (wave-mixing) within the NLC. Intra-pulse DFG offers advantages such as a straightforward optical setup and the production of broadband MID-IR with a pulse duration similar to that of the pump pulse. However, the tunability of intra-pulse DFG is generally limited due to the requirement of the best phase-matching angle of the crystal for achieving the broad bandwidth. On the other hand, inter-pulse DFG needs two separate signal and pump laser pulses, enabling a broader tunable spectral range compared to intra-pulse DFG. This is because independent wavelength tuning of the signal is feasible along with NLC angle tuning. To prevent the generation of angular-dispersive idler pulses in inter-pulse DFG, the optical setup geometry must be collinear. However, this also poses a significant challenge in the development of the MID-IR OPA, as separating the MID-IR from the high-intensity pump pulse and the signal pulse requires special filters and coatings with high damage thresholds and low group-delay-dispersion (GDD) materials[83, 62]. The goal of the MID-IR laser research and development project within the present PhD project is to construct a versatile source capable of delivering both broadband, few-cycle, high-energy pulses and wavelength-tunable, high-energy pulses for spectroscopic applications. The outcome is a robust OPCPA system with two complementary operational modes at a repetition rate of 200 kHz, requiring minimal readjustment when switching between modes.

4.2 Experimental Scheme

Fig.4.2 presents an overview of the MID-IR OPCPA configuration, consisting of the AMPHOS pump laser, two complementary chirped signal NOPA architectures allowing for wavelength tunability or short pulse operation mode, an OPA/DFG stage in LGS crystal, and MID-IR diagnostics. The optical layout and details regarding spectra, power levels, and pulse energies at each stage will be provided in subsequent sections. On top of the MID-IR OPCPA, the remaining portion of the pump laser and MID-IR are employed to excite the vibrational sum-frequency generation (VSFG) spectra from the target samples, which will be discussed in more detail in Chapter5.

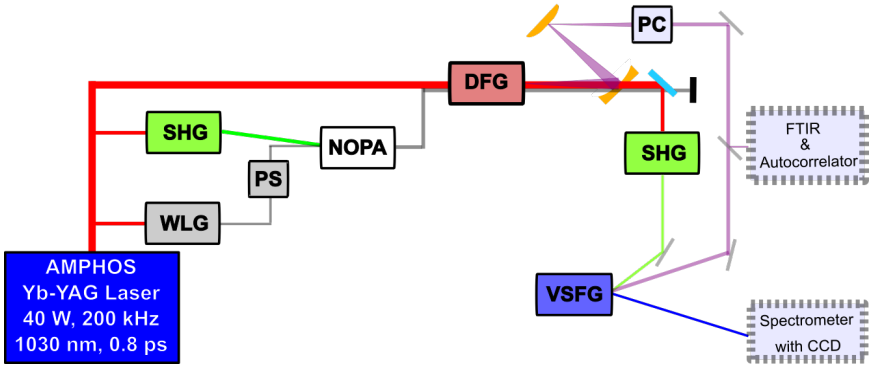

Figure 4.2: The schematic of MID-IR OPCPA. WLG: white-light generation, PS: pulse stretcher, SHG: second-harmonic generation, NOPA: non-collinear optical parametric amplifier, DFG: difference-frequency generation, BS: beam separator, PC: pulse compressor, VSFG: vibrational sum-frequency generation.

4.2.1 Two Chirped-signal NOPA Architectures

The optical configuration of the NOPA is illustrated in Fig.4.3. The system is driven by a total of 40 W output at 200 kHz repetition rate from the AMPHOS laser, equivalent to a pulse energy of 200 μJ. This energy is distributed among three branches: White-light generation (WLG), SHG, and the pump for DFG. By utilizing a combination of a half-wave plate and thin film polarizer, the power ratio between the branch of WLG and SHG can be adjusted as needed. A portion of approximately 8 μJ from the total energy is directed towards generating the signal pulse through the WLG process within an undoped bulk yttrium aluminum garnet (YAG) crystal of 10 mm length. A 10 mm YAG crystal was demonstrated to have the broadest, most stable and robust supercontinuum, pumped with sub-picosecond pulses at 1030 nm[84]. Consistent with the study, the power stability of the white-light output is presented in Fig.4.4, indicating minimal fluctuation of only 0.8 % over a period of 24 hours.

To increase the duration of the signal pulse, either positive or negative group delay dispersion (GDD) needs to be introduced. Let's consider the scenario of the positively chirped pulse first. SF11 is a highly dispersive glass among the commonly used optical materials, and frequently employed to add dispersion either as a simple glass block or in a prism setup. In our configuration, two SF11 blocks with a combined length of 100 mm are placed in the beam path, resulting in a GDD of 12570 fs^2 and a TOD of 11950 fs^3 in the signal pulse. When dealing with the negatively chirped signal, chirped mirrors (CMs) are chosen for their stability, resistance to beam misalignment, and flexibility through adjusting the number of bounces. The

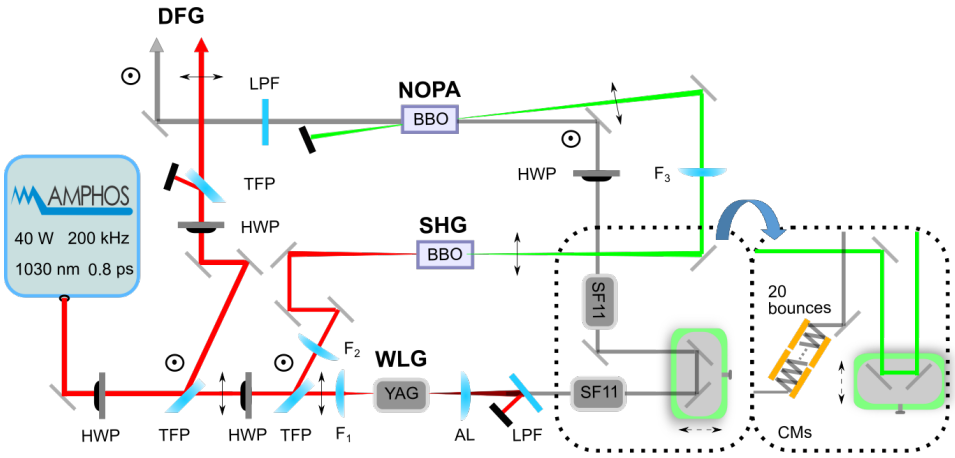

Figure 4.3: Schematic of positively and negatively chirped-signal NOPA allowing for complementary wavelength tunability or short pulse operation mode, respectively. HWP: half-wave plates, TFP: thin film polarizer, AL: Achromatic lens, LPF: long pass filter, CMs: chirped mirrors, Lenses: F_1= 100 mm, F_2= 500 mm, F_3= 500 mm, YAG: yttrium aluminium garnet for WLG; BBO: BaB_2O_4 for SHG and OPA. The two operation modes dependeing on the NOPA architecture can be switched by minimum re-adjustment indicated by the two dotted boxes.

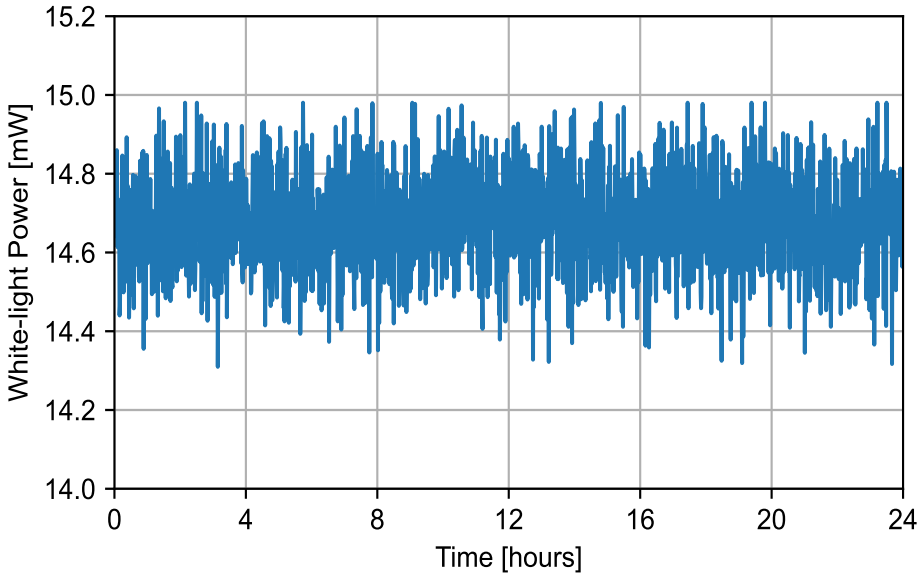

Figure 4.4: White-light power as a function of operation time shows an average value of 14.67 mW with a standard deviation of 120 µW.

dispersion caused by CMs can be modified in small increments, allowing for precise dispersion tuning by adding dispersive materials to the beam's path.

However, CMs have drawbacks such as their higher cost and the need for custom design and fabrication processes, which may not always be available in the interested MID-IR range. Practically, the SF11 stretcher can be replaced with custom-made CMs (Layertec), and the shift of beam path is compensated with minimal readjustment of the setup. In total, the signal pulse obtains the GDD of -11000 fs^2, as it travels 20 bounces between chirped mirrors.

For the 515 nm pump of NOPA, another portion of 26 µJ is directed towards a 1 mm thick β-Barium Borate (BBO) (type I phase-matching). The diameter of the pump beam at the SHG crystal location is ≈260 µm, resulting in an intensity of around 80 GW/cm^2 (which is near the damage threshold of the 1 mm BBO crystal). This process achieves a conversion efficiency of ≈ 53 %. Following the reflection of the pump beam by two high reflective mirrors, the SHG pump energy at the NOPA position is measured at 15 µJ with a beam diameter of ≈ 300 µm, corresponding to an intensity of 27 GW/cm^2. The NLC utilized in the NOPA is a 3 mm type I phase-matching BBO crystal with an external angle of 4.1° between the SHG and the signal beam.

The spectra and pulse energy curves of the two chirped-signal NOPA schemes are shown in Fig.4.5. For the case of positively chirped signal in Fig.4.5 (a) and (b), the maximum power of the signal is 460 mW, corresponding to an energy of 2.3 µJ around 1.15 µm, resulting in a conversion efficiency of ≈ 15.3%. The central wavelength of the signal can be adjusted within the range of 1.14 to 1.36 µm by manually adjusting the time delay between the signal and the pump. Furthermore, the energy profile indicates that energy levels rise as the wavelength decreases, with optimal amplification occurring between 1.12 and 1.16 µm signal wavelength. For the case of the negatively chirped signal in Fig.4.5 (c) and (d), a peak power of 200 mW is reached, which corresponds to a pulse energy of 1 µJ at around 1.15 µm, leading to an estimated conversion efficiency of about 6.7%. The reason causing lower power and pulse energy is the limited available spectral range of the CMs, which only have high reflection (> 99.8 %) and introduce GDD in the spectral range from 1.14 to 1.21 µm. Therefore, some parts of signal, which are out of the available spectral range of the CMs, are unable to participate in the NOPA process, resulting in lower amplification and narrower wavelength-tunable range.

4.2.2 OPA/DFG Scheme in LGS Crystal

Following the NOPA setup, Fig.4.6 shows that, the remaining pulse energy of the pump ≈155 µJ with a peak intensity ≈ 15 GW/cm^2 is used as the pump in the final OPA/DFG stage consisting of an LGS crystal (type II

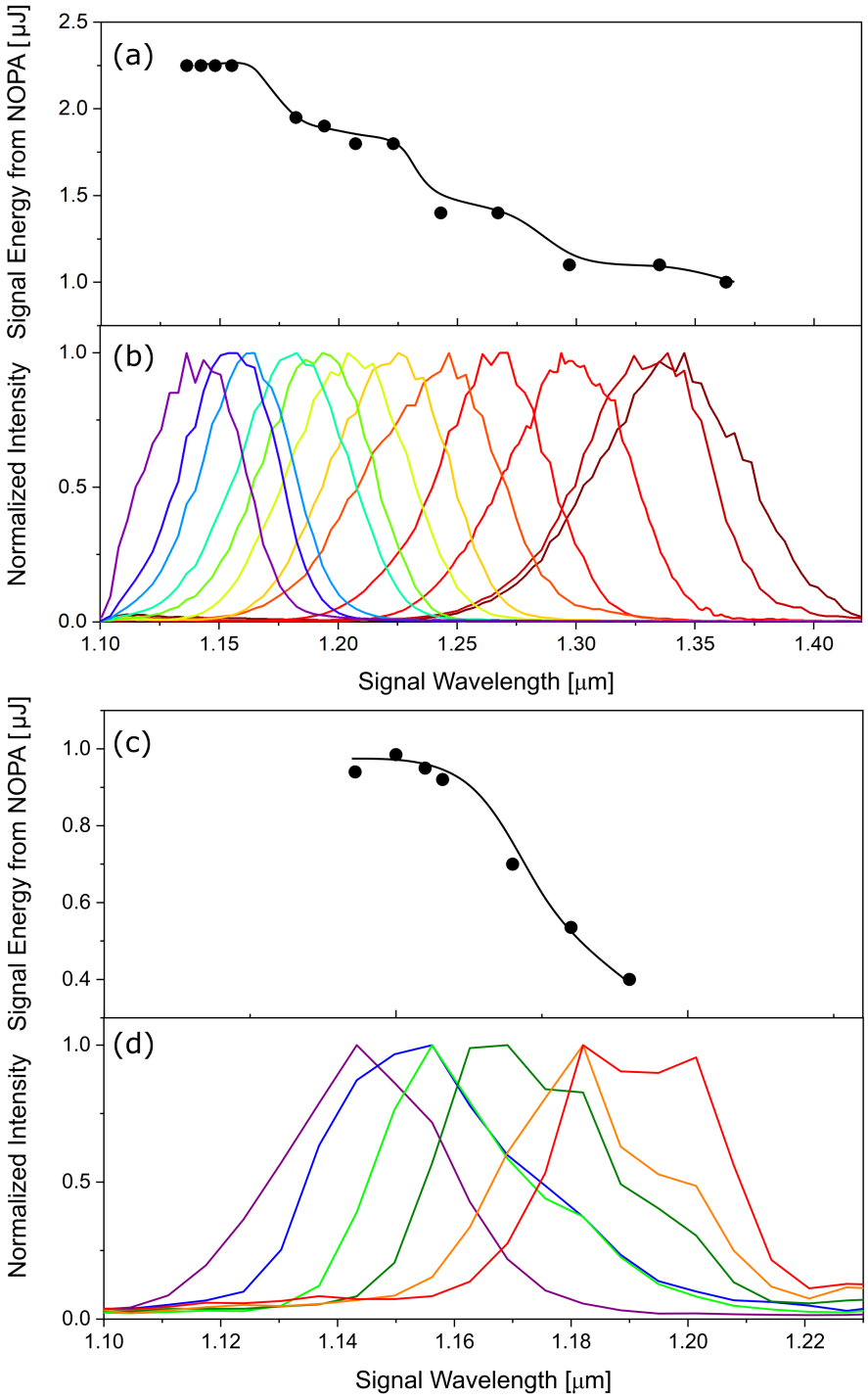

Figure 4.5: The pulse energy curve (a) and the spectra (b) from the positively chirped signal NOPA. The pulse energy curve (c) and the spectra (d) from the negatively chirped signal NOPA.

phase-matching in the XY plane, $\theta = 90°$; $\phi = 37.5°$). Additionally, the power levels of the signal and pump pulses can be adjusted separately to maximize energy extraction. A dichroic beam combiner (Semrock) is used to align the pump and the signal after the NOPA.

It is worth to mention that a specially designed beam separator on a 3 mm-thick ZnSe substrate was utilized to remove the pump and signal pulses, as well as residual chirp in the idler pulse. However, the beam separator required water cooling for long-term use. Due to the high-power pump and signal pulses, the coating on ZnSe substrate was damaged after 30 minutes without cooling. Another successful approach that we used involved taking advantage of the greater divergence in the long-wavelength idler. By combining a two-inch Herriott cell mirror coated with gold (f = 200 mm, center hole diameter of 4 mm) and a protected gold convex mirror (f = -150 mm), a part of the MID-IR can be easily separated and collimated. The central hole of the Herriott cell mirror allows the high-power pump and signal pulses, along with $\approx 65\,\%$ of the MID-IR idler, to pass through. This method is primarily suitable for MID-IR pulse characterization and setup optimization due to the inherent losses. Following the separation of the MID-IR from the pump, a 3 mm ZnSe component acts as a temporal pulse width compressor to reduce remaining positive GDD in the MID-IR pulses. It also serves as a long pass filter to block any remaining signal beam.

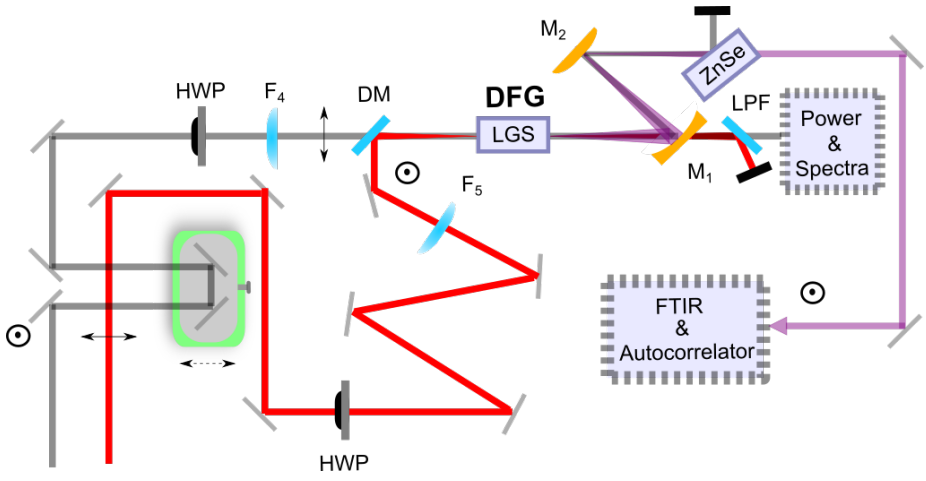

Figure 4.6: Schematic of OPA/DFG. HWP: half-wave plates, DM: dichroic mirror, LGS-5 mm thick: $LiGaS_2$ crystal for OPA/DFG, LPF: long pass filter transmits above 1030 nm, ZnSe-3 mm thick: the temporal pulse width compressor and long pass filter for MID-IR, Lenses: F_4= 1000 mm, F_5= 1000 mm, M_1: Herriott cell mirror f = 200 mm with center hole diameter of 4 mm, M_2: gold convex mirror f = -150 mm.

After the long pass filter, which transmits above 1030 nm, the pulse energy and spectra of the amplified signal in the final OPA/DFG stage can be recorded, as shown in Fig.4.7 and Fig.4.8.

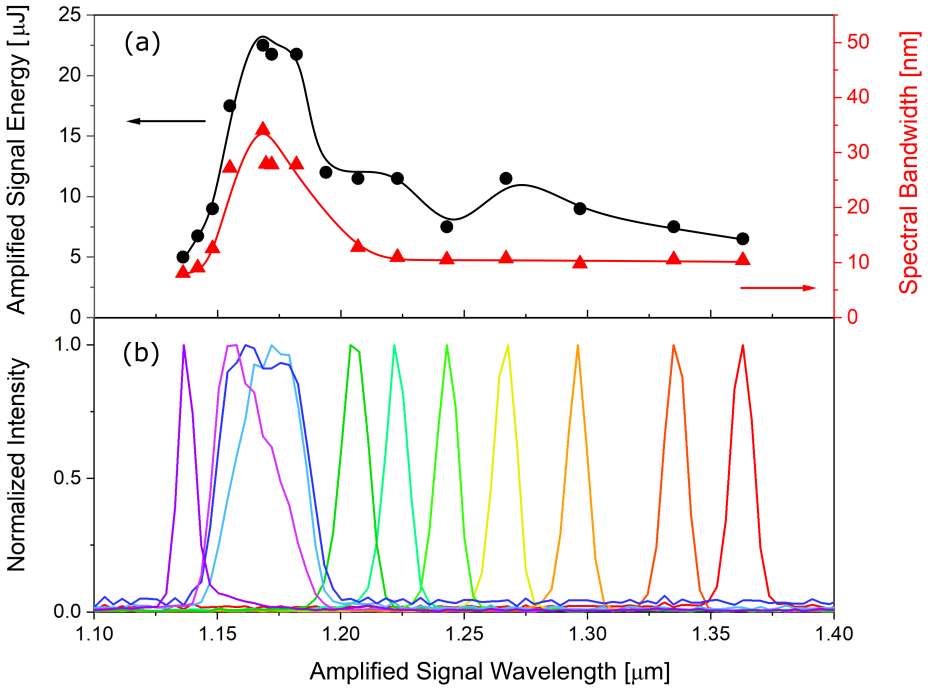

Figure 4.7: Positively chirped signal pulse energy curves behind the final pumped-OPA/DFG stage employing an LGS crystal (a) and the corresponding spectra (b). The spectral bandwidth is derived from the FWHM of spectra.

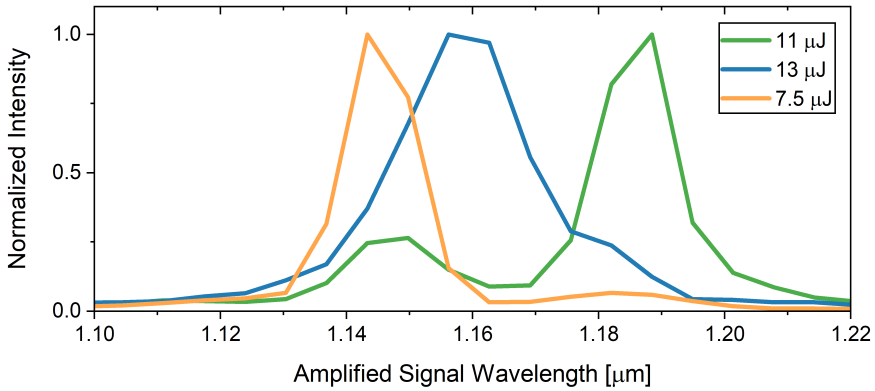

Figure 4.8: Negatively chirped signal pulse spectra behind the final pumped-OPA/DFG stage employing an LGS crystal. The pulse energy levels are around 10 µJ.

Due to the distinct characteristics of two NOPAs, the amplified signal pulses exhibit specific spectra and amplifications. In the case of the positively chirped signal, the spectra in Fig.4.7, show a broad wavelength-tunability from 1.14 to 1.36 µm, which is inherited from its NOPA. Notably, a wide spectral bandwidth of 35 nm is centered at 1.175 µm, and the energy curve displays a peak ≈ 22 µJ with a gain of 10. These phenomena can be explained by the phase-matching of LGS, which is calculated by the software "SNLO V76" and presented in Fig.4.9. For the OPA/DFG pumped at 1030 nm, the spectral range from 1.165 to 1.175 µm of signal pulses have the phase-matching angle ≈ 36.75° in LGS crystal. Therefore, a broad spectral range of signal pulse participates in the OPA process at the same time, showing a broad spectrum and high pulse energy around 1.175 µm. Conversely, inheriting features from the negatively chirped signal NOPA, the signal is amplified up to the maximum of 13 µJ through the OPA/DFG stage, maintaining a broad bandwidth around 1.16 µm with limited wavelength-tunability between 1.14 and 1.21 µm as depicted in Fig.4.8. The two NOPA architectures result in complementary MID-IR pulse properties. The selected operation mode

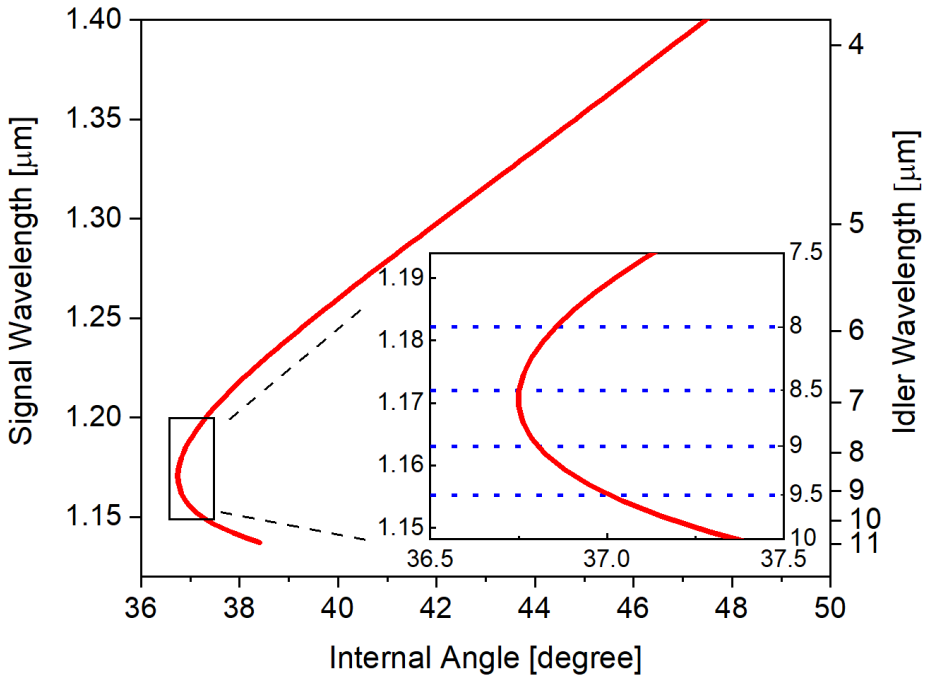

Figure 4.9: The phase-matching of LGS crystal for OPA/DFG pumped at 1030 nm. The signal and idler wavelengths are displayed on separate y-axes. A magnified view of the spectral range from 1.15 to 1.19 µm is shown. The result is generated using the "Opoangles" function in SNLO v76[62].

offers either a large MID-IR wavelength tunability range or a few-cycle, broad spectral bandwidth MID-IR pulse. Their characteristics will be discussed in the following section.

4.3 MID-IR Pulse Characterization

4.3.1 Spectral Properties

Due to the symmetry of signal and idler, the MID-IR idler pulses exhibit similar characteristics to the amplified signal pulses. First, the spectra and the energy profile of the MID-IR generated from the positively chirped signal are shown in Fig.4.10. Being down-converted in frequency from the wide tunable spectra of the amplified signal pulses, which is displayed in Fig.4.7,

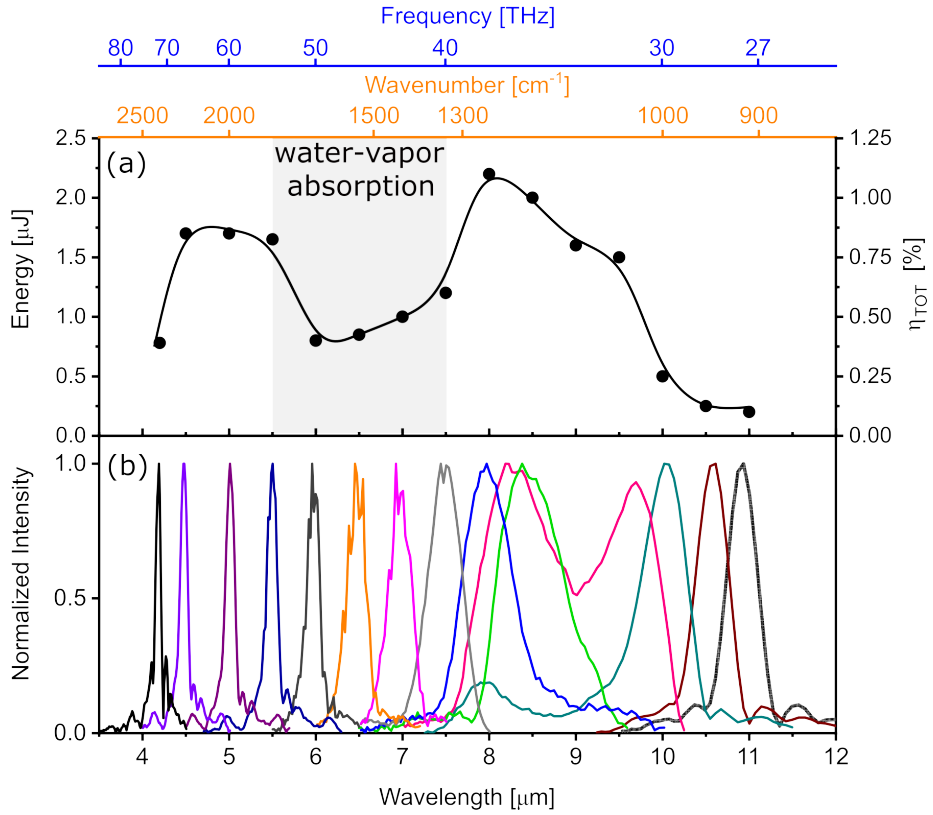

Figure 4.10: MID-IR pulse energy curve (a) and the total efficiencies of the MID-IR spectra (b) generated from the positively chirped signal NOPA scheme. The gray area denotes the spectral range of water-vapor absorption. Adapted with permission from [85].

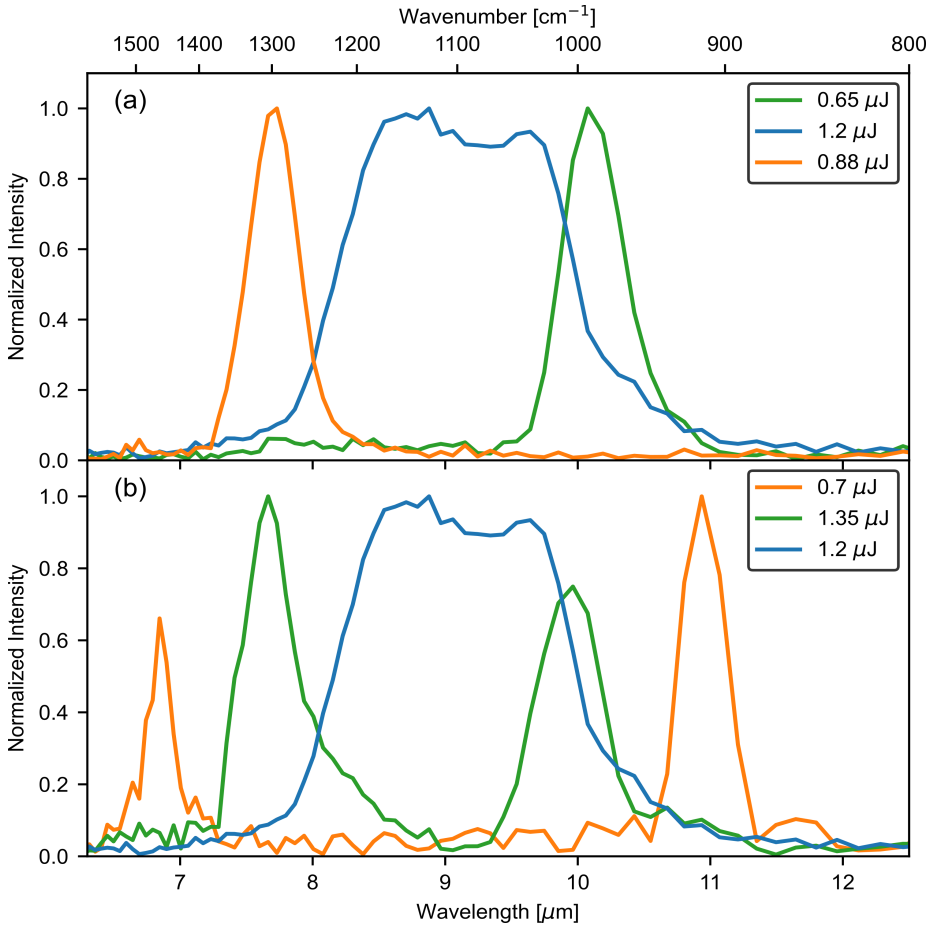

Figure 4.11: The MID-IR spectra generated from the negatively chirped signal NOPA scheme, which can be tuned between 7.8 to 10.2 µm (a). By detuned LGS crystal θ angle from the perfect phase-matching, the MID-IR spectra present double peaks at 7.8 and 10 µm, and the peaks can even be separated further to 6.8 and 11 µm for larger detuning angles (b).

the MID-IR pulses own the wavelength-tunability from 4.2 to 11 µm as well. By achieving perfect phase matching, a maximum pulse energy of $\approx 2.2\,\mu J$ and an average power of $\approx 450\,mW$ are obtained at 8.5 µm. It is worth to note that a bradband spectrum is also amplified with peaks at 8.3 µm and 9.7 µm. Due to the fine mismatch from the perfect phase-matching in the degenerate OPA, multiple signal wavelengths can be involved in the condition of $\Delta k=0$, resulting in broader spectra of the signal and idler. Further details about the calculation of wave–vector mismatch and expected gain bandwidth can be found in the OPA tutorial (Manzoni & Cerullo, 2016, p.15)[10]. Overall, the MID-IR pulses have high energy levels exceeding 1 µJ, except for a dip

at 5.5–7.5 µm, attributed to water-vapor absorption in air, which can be mitigated using beam propagation in vacuum.

In the case of the negatively chirped signal NOPA, converted from the amplified signal spectra shown in Fig.4.8, the MID-IR idler spectra are depicted in Fig.4.11 (a). The measured MID-IR spectra can be adjusted within the range of 7.8 to 10.2 µm by tuning the central wavelength of the signal in the NOPA. The spectrum at a central wavelength of 9 µm has an average power of around 240 mW, which is corresponding to ≈ 1.2 µJ. It is important to note that the LGS transmission near 9 µm is only about 20%, which is evident as a dip in the spectrum. Another crucial factor of changing the spectral profile is the phase-matching of the LGS crystal. The optimal amplification of MID-IR (1.35 µJ) exhibits two peaks at 7.8 and 10.2 µm in the spectrum, which are similar to the spectrum in Fig.4.10 (b). If the θ angle of the LGS crystal deviates from the perfect phase-matching, the two peaks will separate further at 6.8 and 11 µm, respectively. To cover a broad spectral range and achieve a Gaussian-like spectrum for temporal pulse compression, the spectrum at a central wavelength of 9 µm is chosen and the pulse fully characterized in time domain as it will be discussed in the

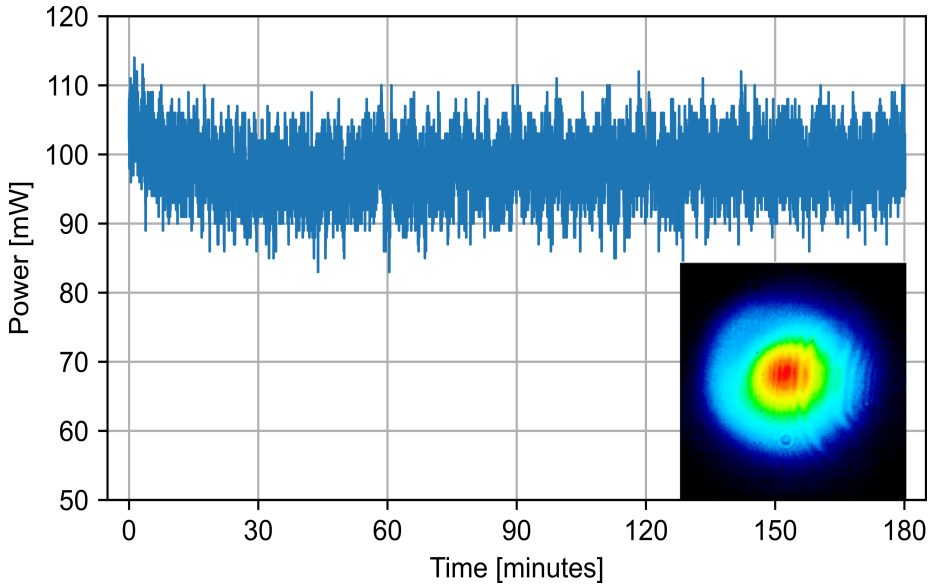

Figure 4.12: The MID-IR power monitoring has been done for 3 hours and demonstrates an average power of 98.4 mW with a standard deviation of 3.795 mW. The $1/e^2$ diameter along the horizontal and vertical direction are 3.8 and 3.1 mm, showing an effective diameter of 3.4 mm with $M^2 \approx 1.4$ using a commercial beam profiler (WinCamD-IR-BB).

following subsection. We note in passing that some characteristics such as beam profile measurements and long-term power monitoring have been done as well. The results are given in Fig.4.12, exhibiting a beam diameter of ≈ 3.4 mm and 3.8 % power fluctuation. The broad 9 µm spectrum remains the same spectral shape after an overnight measurement.

4.3.2 Temporal Properties

Regarding the temporal characteristics of the MID-IR pulses in the positively chirped signal scheme, the spectral bandwidth from 7.5 to 10.2 µm in Fig.4.10 (b) supports a theoretical Fourier-transform-limited pulse duration of 77 fs. However, residual GDD and TOD from SF11 are challenging to eliminate entirely using germanium (Ge) bulk material. Because of introducing additional TOD from Ge, an asymmetric temporal profile and multiple delayed replicas may cause problems for the temporal diagnosis. Hence, a pulse duration of 1042 fs without compressing is calculated by the program, which will be introduced in the Appendix (Sec.7.2).

For the MID-IR generated from the negatively chirped signal scheme, the temporal characterization of pulses are done using a home-built intensity and a commercial interferometric autocorrelator, respectively. As illustrated in Fig.2.4, the beam splitter in the intensity autocorrelator is a KBr substrate (thickness, 4 mm) with a Ge coating on one side (Spectral Systems). Due to the GDD introduced by the KBr substrate (17 mm path length gives -3953.74 fs^2), the transmitted part of the MID-IR gets additional chirp. Therefore, the convolution of chirped and unchirped MID-IR pulses is actually a cross-correlation, instead of an autocorrelation. The details of deconvolution are given in the Appendix (Sec.7.2). In short, the cross-correlation width τ_{CC} (FWHM) results in a MID-IR pulse width of $\tau_p \approx 74 \pm 2$ fs (FWHM).

The challenges associated with the cross-correlator include the inability to directly measure the pulse width and the necessity of making assumptions and approximations when performing deconvolution through mathematical methods. Hence, the utilization of a commercial interferometric autocorrelator for the direct assessment of pulse duration offers advantages. First, the reflected and transmitted beams travel the equal distance in the balanced beam splitter, so two identical replicas of MID-IR pulses can undergo autocorrelation. Furthermore, interferometric autocorrelation demonstrates sensitivity to the chirp of pulses that is not discernible through intensity autocorrelation measurements.

The interferometric autocorrelation trace, which has been fitted with a Gaussian envelope, is depicted in Fig.4.13 (a). The measurement perfectly matches the mathematical descriptions of the autocorrelation: (1) the ratio

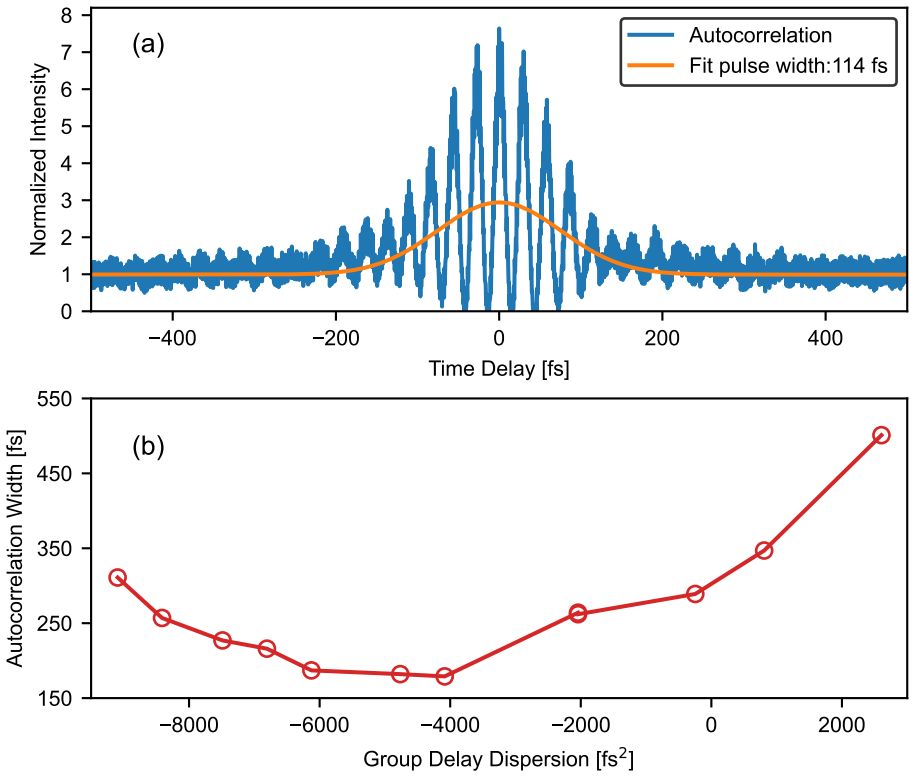

Figure 4.13: The autocorrelation trace of the MID-IR pulse fitted with a Gaussian function (a) and the shortest autocorrelation width 168 fs extended by adding group delay dispersion from bulk materials, e.g, Ge for +GDD and ZnSe for -GDD (b).

of the peak to the background is 8:1 and (2) the interference-free component, which is actually an intensity autocorrelation, exhibits a peak to background ratio of 3:1 from the Gaussian fitting. Furthermore, the narrowness of interference pattern can be used to approximately measure the linear chirp of pulses. For instance, if the pattern of lower and upper envelope is much narrower than the intensity autocorrelation component, it indicates that a large chirp exists in pulses. In our case, the lower and upper envelopes of the interference pattern split evenly from the background level and merge along with the intensity autocorrelation at large time delay, showing that the MID-IR is close to an unchirped pulse. For pushing towards the shortest pulse width, Ge and ZnSe bulk material are inserted into the MID-IR beam path to remove the residual GDD. Fig.4.13 (b) demonstrates that the shortest autocorrelation width can be achieved at around 168 fs by introducing about -4000 fs^2 GDD with a 6 mm thick ZnSe. Due to the chirp (–1430 fs^2 GDD) caused by the balanced beam splitter in the autocorrelator, an unchirped pulse width has

to be derived by Eq.2.4.2. In summary, an interferometric autocorrelation reveals a pulse width of 114 fs, which corresponds to 3.8 optical cycles at a central wavelength of 9 µm. This measurement is near the transform-limited pulse width of 80 fs.

4.4 Performances of MID-IR OPCPAs

To summarize, a versatile design of a MID-IR OPCPA laser system is presented by using an LGS crystal for efficient frequency-down conversion of high-power 1030 nm pump pulses. The two discussed operation modes differ in the GDD of the signal pulse in the final DFG stage. Depending on the application, the laser architecture can be easily switched between complementary MID-IR pulse parameters in frequency and time domain, which are characterized by means of FTIR and autocorrelators, respectively. On the one hand, the scheme with the positively chirped signal provides a wavelength-tunable source (from 4.2 to 11 µm) that is well-suited for vibrational spectroscopy of gas phase molecules and liquids. The vibrational line widths of molecules are in the few $\approx$ 1–10 ps region, therefore the system without the pulse width compressing is an ideal tool for vibrational imaging and related applications including

Authors	Spectral range [µm]	Power [mW]	Energy [µJ]	Width [fs]
This	4.2–11	450 at 8.5 µm	2.2	1042
work	7.8-10.2	245 broadband	1.2	114
[29]	6.7–18	103 broadband	0.001	66
[45]	6–11	1300 at 8.5 µm	0.034	110
[23]	-	140 at 9 µm	14	142
[86]	6.5–9.2	105 at 8.1 µm	1.05	121
[87]	5.7–10.5	53 at 7.8 µm	0.53	98
[46]	3–7.5	40 at 7.5 µm	0.04	540
[35]	6.5–12	31 at 7 µm	0.16	120
[47]	5–11	11 broadband	0.22	32
[88]	4.6–9.2	0.04 at 9.2 µm	8	2000

Table 4.1: Performance parameters of MID-IR laser systems based on lithium gallium sulfide (LGS) nonlinear crystals. Adapted with permission from [85].

microscopy. On the other hand, the negatively chirped signal scheme provides a broadband MID-IR pulses centered at 9 μm that can be compressed to a shortest pulse width of 114 fs. These schemes are of considerable interest for coherent nonlinear spectroscopy and imaging applications involving multi-photon physics and time-resolved studies. It is important to note that both schemes generate pulses with 1–2 μJ energy at 200 kHz repetition rate, reaching similar pulse-energy levels as other published works. The state-of-the-art laser parameters from recent literature using LGS crystals in the final DFG stage in comparison to the present thesis work are summarized in Tab4.1.

Chapter 5

Vibrational Sum-frequency Generation Spectroscopy from Quarz to Biomolecules in Solution

5.1 Motivation

According to the estimation from International Diabetes Federation (IDF), 10.5 % of the adult population (20-79 years) has diabetes in 2021, and there will be around 783 million adults, equating to 1 in 8 individuals, affected by diabetes by 2045[2]. Therefore, monitoring the blood glucose levels of individuals is a crucial task for preventing and controlling the disease. However, conventional finger pricking measurement makes it uncomfortable and there are variations in blood sugar readings between test strips. Hence, sensitive and accurate non-invasive glucose monitoring techniques (NIGM) are of considerable interest.

Some techniques with vibrational spectroscopy were developed to observe the carbon-oxygen bond stretching modes between 1000 and 1200 cm^{-1}, which are sensitive to the concentration of glucose solution. Using infrared light sources such as commercial FTIR[89] and quantum cascade laser (QCL)[90], the absorption band at 1035 cm^{-1} shows highly linearity with glucose concentration until 5.5 mM, which is close to the blood sugar level of 4- 11 mM, but does not cover the entire range. Raman spectroscopy can detect even lower concentration down to 1 mM with a peak at 1125 cm^{-1}[91]. However, the Raman glucose peak is often a weak signal in vivo detection, because of the light absorption by non-glucose components. Therefore, some enhanced Ra-

man techniques are utilized like, surface-enhanced Raman scattering (SERS), which could increase the signal strength by 8 orders of magnitude and shorten the acquisition time to 30 second[92], and graphene-enhanced Raman scattering (GERS), which is sensitive up to 0.5 mM[93]. In addition, to remove the fluorescence background, which is caused by laser irradiation in spontaneous Raman scattering, coherent Raman methodologies are implemented by probing the third-order susceptibility $\chi^{(3)}$ with ultrashort pulses. For example, coherent anti-stokes Raman scattering (CARS) typically shows stronger signals than Raman scattering with mitigated background[5]. Furthermore, stimulated Raman scattering (SRS) is able to provide a background-free glucose spectrum that can be recorded in a phenomenal 0.6 second integration time[6].

Recently, ultrashort MID-IR pulses at wavelength in the spectral fingerprint region offer more opportunities in glucose sensing. For example, MID-IR field-resolved spectroscopy (FRS)[7] breaks through the limit of detection (LOD) down to 0.1 mM. Besides, enhanced selective excitation of ground-state vibrational modes, MID-IR pulses could be used to identify different cellular components by means of hyperspectral imaging[77]. Vibrational sum-frequency generation (VSFG) spectroscopy is a powerful surface-sensitive method, which relies on a second-order nonlinear process (the explaination can be found in Sec.2.6). Hence, the application range from studies of structural characteristics, chemical composition, and molecular orientation by probing vibrational resonances at liquid-solid, liquid-gas, and solid-gas interfaces. Furthermore, the spatial resolution in VSFG microscopy can exceed that of IR microscopy by focusing the visible (VIS) wavelength laser beam for frequency upconversion down to the sub-μm range.

For typical applications, there are two types of setups, which are commercially available[94]. One realization is narrowband scanning-SFG (typical spectral bandwidth 6 cm^{-1}) with wavelength-tunable IR (from 1000 to 4300 cm^{-1}) picosecond pulses. In this scheme, the IR wavelength is step-scanned across the complete spectral range of interest. Here can excite only one vibrational band without coupling the other states. Another realization is broadband-SFG (BB-SFG) with broadband IR (spectral bandwidth from 150 to 450 cm^{-1}) femtosecond pulses ($\approx$ 100 fs). BB-SFG can simultaneously probe many vibrations at once. If the spectral window of interest is completely covered by the spectral range of the IR pulse, there is no need for IR scanning. More variants of SFG can be realized by manipulating the VIS beam. For example, high-resolution SFG (0.6 cm^{-1}) has been demonstrated using an extremely long VIS pulse ($\approx$ 90 ps) in time domain[95], and doubly-resonant SFG applying a wavelengh-tunable VIS pulse is another option[96]. Furthermore, advanced experimental schemes like, time-resolved SFG[97], phase-sensitive SFG[98]

and momentum-dependent SFG[99] open many windows for characterizing molecular vibrations at surfaces and interfaces.

Since 1999, the vibrational fingerprint of glucose from 2800 to 3000 cm^{-1} has been studied by VSFG spectroscopy[100, 101, 102]. However, to the best of my knowledge, there is no publication on VSFG studies on vibrations between 1000 and 1200 cm^{-1}, which are crucial for glucose sensing in aqueous solution. The potential constraints may arise from low MID-IR power and pulse energy generated from $AgGaS_2$ crystal. For example, the commercially available BB-SFG of the EKSPLA company[94] offers only 0.5 mW and 0.5 μJ at 10 μm (corresponding to 1000 cm^{-1}). Research and development in recent years allowed for BB-SFG by making use of an LGS crystal in a single OPA stage. This scheme generates broadband pulses around 1180 cm^{-1} at significantly higher output power of 48 mW[87]. Following this strategy, the MID-IR pulses generated at 200 kHz from our home-built OPCPA at higher pulse energy of 1.2 μJ and higher power of 245 mW around 1100 cm^{-1} paves the way for observing characteristic glucose absorption bands in VSFG spectroscopy. Furthermore, the developed VSFG spectroscopy setup makes perfect use of the two complementary operation modes of the MID-IR OPCPA, i.e. the wide wavelength scanning range from 800 to 2500 cm^{-1} and the ultra-broadband (few-cycle pulse) from 800 to 1400 cm^{-1}. More details will be introduced in the following sections.

5.2 Experimental Scheme

5.2.1 Vis-IR Sum-frequency Generation Setup

After the DFG process shown in Fig.4.6, the 1030 nm beam and the MID-IR beam are separated using a concave mirror with a center hole diameter of 4 mm. The beam path of the MID-IR is illustrated in Fig.5.1. To control the power of the MID-IR beam, a combination of a half-wave plate (HWP) and a wire-grid polarizer (WGP) is used. Due to the broad spectral bandwidth of the MID-IR, a single HWP cannot cover this entire spectral range, necessitating the use of at least three HWPs individually for the measurements. However, this approach significantly increases the complexity of the experiment. Furthermore, the small apertures of the HWPs (with a typical diameter of 6 mm) introduce losses in the MID-IR beam. Thus, the setup shown in Fig.5.1 uses a different approach. The MID-IR beam is maintained at P-polarization as it was initially generated, and the power can be adjusted by rotating the WGP, which reflects all polarization along the wire length. The WGP not only transmits the P-polarized MID-IR beam but also eliminates any light leakage from the

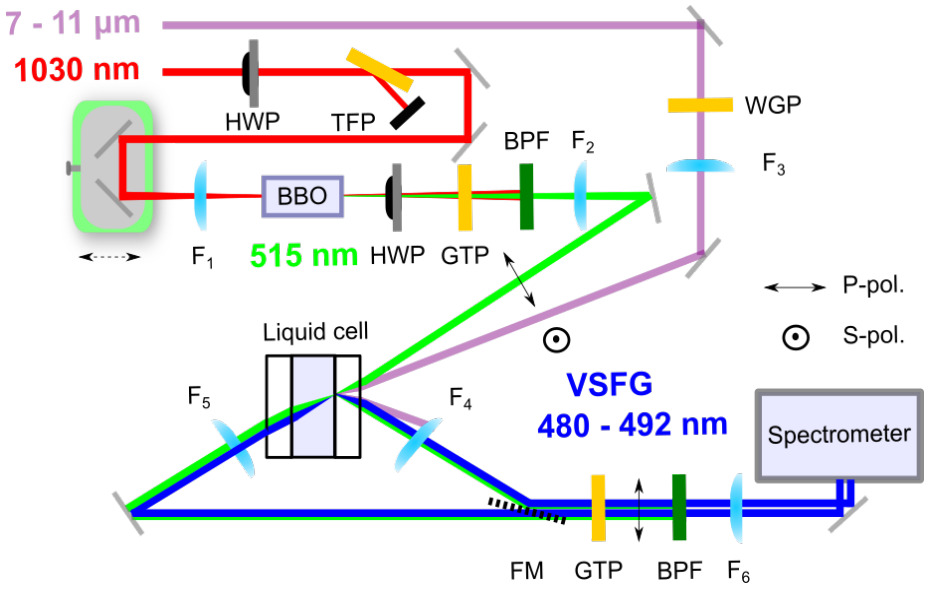

Figure 5.1: Schematic of the ultra-broadband VSFG spectroscopy setup. HWP: half-wave plate, TFP: thin film polarizer, BBO: BaB_2O_4, GTP: Glan-Thompson polarizer, WGP: wire-grid polarizer, BPF: bandpass filter, Lenses: $F_1 = 150\,\text{mm}$, $F_2 = 75\,\text{mm}$, $F_3 = 200\,\text{mm}$, $F_4 : 30\,\text{mm}$, $F_5 : 75\,\text{mm}$, $F_6 : 150\,\text{mm}$, FM: flip mirror. Adapted with permission from [15].

previous DFG stage. Finally, the MID-IR power of 120 mW is focused onto the sample using a ZnSe lens, resulting in an intensity of $\approx 1.5\,\text{GW/cm}^2$ at a beam diameter of 675 µm according to calculations. It is important to note that the thickness of the ZnSe lens can precisely compensate for the remaining GDD in the MID-IR pulse.

After setting the MID-IR to P-polarization, it is beneficial to adjust the VIS to S-polarization to enhance the response of the S-polarized SFG, as indicated by the Fresnel factors in Fig.2.7. When focusing the P-polarized 1030 nm beam onto a 1 mm type I BBO crystal, the SHG process generates an S-polarized 515 nm beam with an efficiency of $\approx 20\,\%$, and the pulse width is on the order of ≈ 1 ps generated by 0.8 ps width of AMPHOS laser pulse. The VIS power can be adjusted between 0 and 1 W by using a combination of the HWP and Glan Thompson polarizer (GTP). It is important to clean the VIS beam with a band pass filter (BPF) to remove unwanted light from the previous DFG stage. Once the beam is filtered, focusing 1 W of power on the sample position results in an intensity of $\approx 7\,\text{GW/cm}^2$ at a beam diameter of around 300 µm according to calculations.

Having generated the necessary pulses for VSFG, the next step is to direct MID-IR and VIS towards the sample followed by collecting and sending the

SFG to the detection system, commonly known as "the bridge" in VSFG experiments[22]. The first thing to decide is the geometry of combining MID-IR, VIS and SFG, i.e. between collinear or non-collinear SFG. On the one hand, collinear SFG, because a appropriate dichroic mirrors for MID-IR and VIS are typically rare and expensive, can be pretty-well achieved by a simple D-shape mirror. In practice, the D-shape mirror reflects VIS and let MID-IR pass by as close as possible without clipping. One benefit is that the collinear SFG spatially overlaps with the VIS beam, making it straightforward to locate and direct the beam into the spectrometer. However, the VIS beam also cause a trouble, because the leakage from the filter in front of the spectrometer saturates the charge-coupled device (CCD) detector during long exposure times or for high pumping intensity. On the other hand, non-collinear geometry can block the unwanted propagation of the VIS beam onto the CCD easily by passing the SFG through a pin hole. This results in better signal-to-noise ratio. It is important to point out that because of the phase-matching condition, non-collinear SFG results in angular dispersion, which causes a divergent distribution of sum-frequency wavelengths. However, the impact of this dispersion on the recorded SFG spectra is minimal due to the small angle ($< 8°$) between incident beams and the small magnitude of MID-IR k-vector ($\approx 5\,\%$ of 515 nm k-vector). Furthermore, the angular dispersion can be managed by setting a wider spectrometer's slit width (from 300 to 500 µm).

The molecular VSFG signal is typically weak in intensity, so the strategy of searching for the SFG involves starting with samples that exhibit a strong response, such as $LiNbO_3$, GaSe and LGS nonlinear crystals. Once the spatial and temporal overlap are determined, the SFG can be visually observed. Moreover, the transmitted SFG is significantly more intense than the reflected SFG by up to 3 orders of magnitude, attributed to the longer coherence length[16]. Due to its high transparency at 515 nm and MID-IR wavelength, LGS is an optimal crystal for detecting SFG signal in our configuration. Practically, a needle is utilized to mark the sample surface position, facilitating the identification of the signal, which becomes more straightforward and reproducible when changing samples.

To improve the collection and collimation of scattered SFG from samples with rough surfaces, a lens with a short focal length of 30 mm is used. The gathered SFG is directed into the detection branch separately by a flipping mirror for both transmitted and reflected SFG beams. The GTP selectively transmits the S-polarized SFG, while the BPF blocks the 515 nm beam and allows the transmission of the SFG beam in the spectral region of interest from 480 to 492 nm. Finally, a lens positioned before the spectrometer focuses the light onto a slit to enhance the spectral resolution and transmission intensity

of the SFG[22].

5.2.2 Low-noise Spectrometer with Cooled CCD

After directing the light into the spectrometer, the frequencies of SFG beam are dispersed by the grating of the spectrograph (Andor Shamrock SR-500i) and then captured with a CCD camera (Newton 940) based on a Czerny-Turner optical design. Depending on the application one can choose between different gratings. Each grating has a specific groove density, where higher densities provide better spectral resolution but reduce efficiency. Each grating is also blazed to maximize efficiency at a particular wavelength. Additionally, gratings with higher groove densities cover a smaller spectral range, as the enhanced frequency resolution essentially zoom into a specific part of the spectrum. The Shamrock SR-500i spectrograph is a fully motorized device to control the slit width from 10 to 2500 µm and switch between gratings, which are listed in Tab.5.1.

The spectrograph is equipped with a CCD camera. CCD cameras used for VSFG spectroscopy must be highly sensitive to detect the rather small signal intensity generated in experiments. A low background level is crucial for achieving a high signal-to-noise ratio. It can originate from various sources such as residual light in the lab and stray light from the OPCPA. In general, a conventional CCD camera that is cooled down can be utilized. Cooling the CCD helps to reduce dark current to a minimum and ensures that any

Groove density	Blaze wavelength	Efficiency	Resolution	
[l/mm]	[nm]	[%]	[nm]	[cm^{-1}]
150	500	73	0.52	22
300	500	81	0.26	10
300	860	15	0.26	10
1200	850	20	0.06	2.5
1800	400	65	0.04	1.67
2400	300	45	0.03	1.25

Table 5.1: Parameter of gratings comprising the spectrograph. Note the efficiency applies to the SFG wavelengh (from 480 to 492 nm) and the given spectral resolution is only valid for minimized scattered light, e.g., the narrowest slit width of 10 µm.

incoming light generates a strong signal compared to the background. The Newton 940 CCD camera series features a 2048×512 array of 13.5 µm sized pixels and is equipped with thermoelectric cooling down to -100 °C (typically -50 °C in our setting) for exceptional performance. The spectrograph is calibrated by using a Hg/Ne lamp that emits a well-known spectrum, which helps determine the wavelengths corresponding to each pixel on the CCD.

5.3 Results and Discussion

5.3.1 Sum-frequency Phonon Spectroscopy on Quartz for VSFG Alignment

The experimental campaign has been started by recording a strong SFG signal from the LGS crystal. However, this signal is only suitable for rough alignment. Achieving precise alignment with nonlinear crystals is difficult for several reasons. Firstly, the signal is so intense that it can easily saturate the CCD camera. Secondly, the signal may primarily come from the bulk of the crystal rather than from the surface, where centrosymmetry is broken and the liquid sample will be positioned. Thirdly, LGS may not show "flat" phase-matching in the long-wavelength range, causing differences between the generated SFG spectral profile, which should be the up-converted MID-IR pulse spectrum, and the actual MID-IR spectral profile. Therefore, it is necessary for precise alignment to replace LGS with a material that generates a much weaker nonresonant SFG response.

Experimental studies have demonstrated that a gold (Au) film on wafer[103] and quartz[16] are well-suited materials because of their spectral flatness at somewhat higher photon energies (2000-4000 cm^{-1}). This means that the SFG spectrum only reflects the spectral profile of the MID-IR pulse. The SFG from Au and quartz are solely generated by a nonresonant process, having a constant $\chi^{(2)}_{\mathrm{NR}}$ and no resonant contributions $\chi^{(2)}_{Rq}$ in Eq.2.6.1. In our spectral range of interest, quartz crystal has been demonstrated to show strong zone-center optical phonon absorption peaks at 1065 and 1160 cm^{-1}[104]. In the present work, the quartz sample allows for easy alignment and first calibration of the VSFG spectrometer providing a strong resonance-enhanced SFG signal. A 5 mm thick z-cut α-quartz is used in the experiments, as both transmitted and reflected SFG from quartz can be measured. By adjusting the sample position, temporal/spatial overlaps, and the OPCPA in real-time, the intensity and spectrum of SFG is optimized. Once the signal is correctly directed onto the CCD camera, the measurement can proceed under optimized experimental conditions by switching from quartz to the glucose samples.

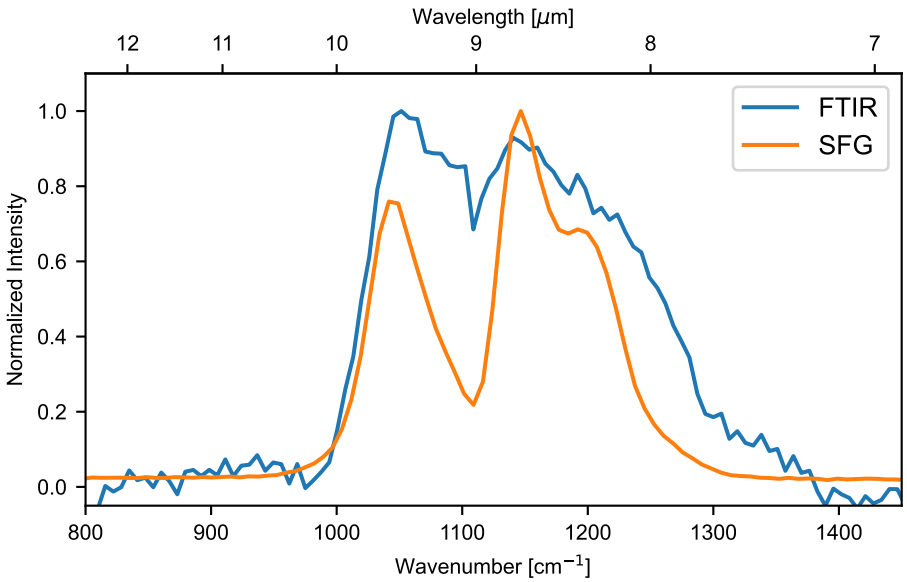

Figure 5.2: The FTIR spectrum of broad 9 µm and the SFG spectrum from the quartz surface. The latter spectrum is generated by 10 mW of 515 nm and 100 mW of MID-IR. The spectral resolution of the VSFG and the FTIR spectrometer is 32 cm^{-1} and 2 cm^{-1}, respectively.

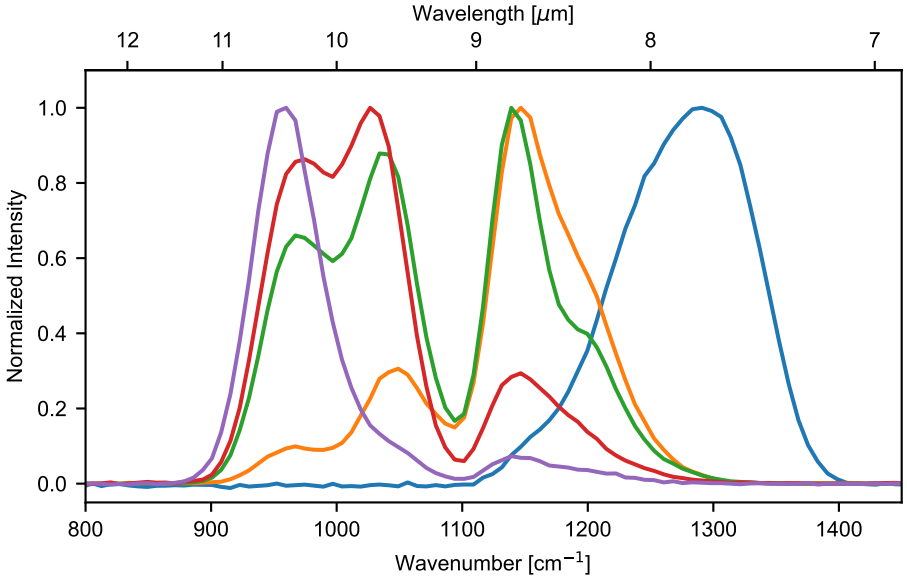

Figure 5.3: The SFG spectra from the quartz surface, which can be adjusted between 900 and 1400 cm^{-1} by tuning the central wavelength of the signal in NOPA.

Fig.5.2 displays the reflected SFG spectrum from quartz. The excitation energy of characteristic optical phonon modes of the α-quartz crystal lies well within the MID-IR pulse spectrum. Additionally, the SFG spectrum can be tuned between 900 and 1400 cm^{-1} by adjusting the central wavelength of the signal in NOPA, as depicted in Fig.5.3.

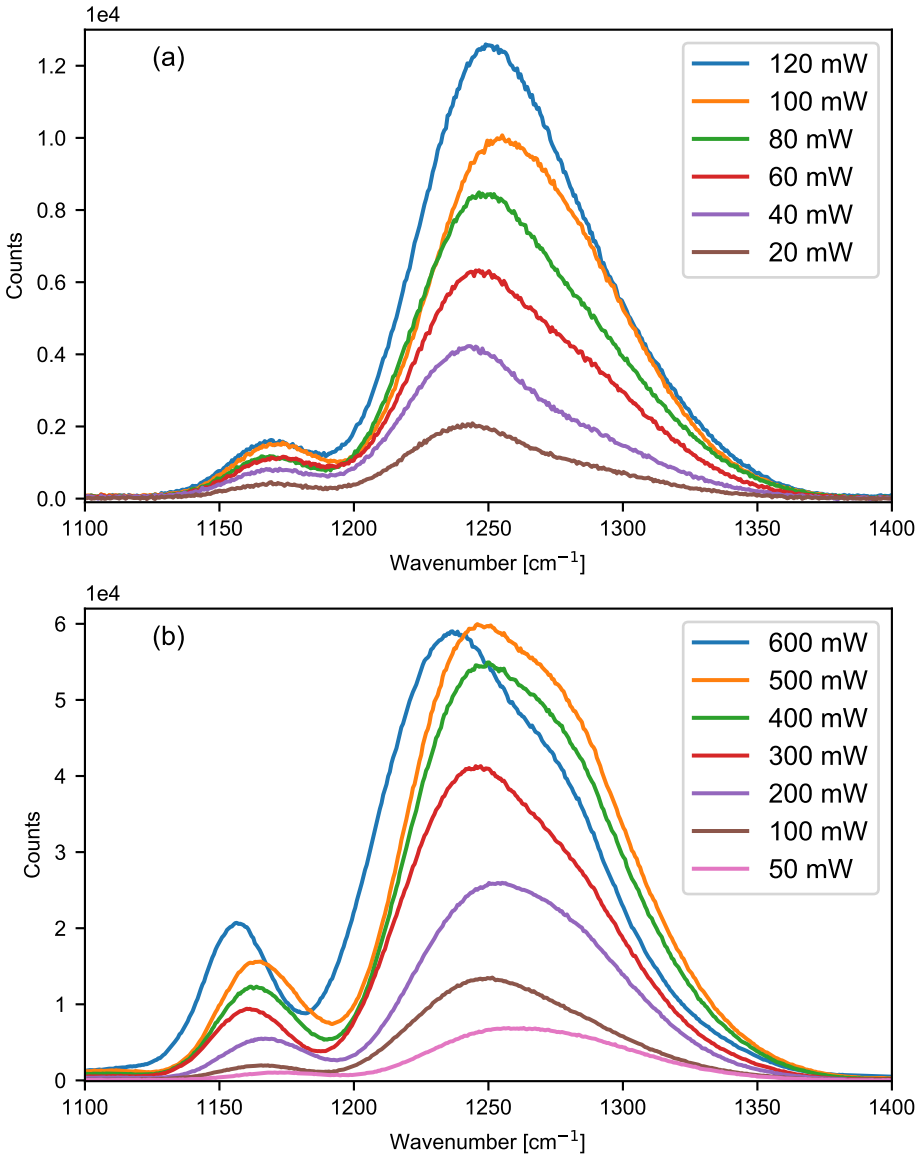

Figure 5.4: The MID-IR power-dependent SFG spectra with the fixed 515 nm power of 50 mW (a) and the 515 nm power-dependent SFG spectra with the fixed MID-IR power of 100 mW (b).

To improve the signal-to-noise ratio, it is necessary to use higher power levels of VIS and MID-IR pumping without causing damage to the samples of interest. The average power range of VIS and MID-IR are tested using quartz. Thereby it is ensured that the pulses generate similar spectra as a function of laser average power without causing higher-order nonlinear effects. The spectral profiles of the SFG signal remain overall consistent as the power level of the MID-IR increases, as shown in Fig.5.4 (a) when excited with a fixed 515 nm power of 50 mW. Slight shifts in the center of mass are likely due to experimental uncertainties. The maximum values of the spectra vary linearly with the power of MID-IR, as depicted in Fig.5.5 (a). The SFG intensity, described as a second-order process in Eq.2.6.1, is directly proportional to the intensity of MID-IR (or VIS) with fixed VIS (or MID-IR) intensity, in agreement with our experimental result. When the MID-IR power is fixed at 100 mW, the SFG spectra dependent on the 515 nm power exhibit a linear relationship up to 400 mW, with a slight blue shift at 600 mW, as shown in Fig.5.4 (b). Above 500 mW of VIS power the spectra show intensity saturation, as seen in Fig.5.5 (b). The following experiments on cellulose and glucose samples are all carried out in the linear power-level region.

5.3.2 Setup Calibration Using Cellulose Pellets

Before doing experiments on the glucose samples of interest, it is advisable to measure a well-characterized test sample to showcase the capabilities of the VSFG setup. Additionally, the fine calibration of the spectrograph (usually below $\pm 10\,\mathrm{cm}^{-1}$ accuracy) using a known sample is essential, as the rough calibration with Hg/Ne lamp is only accurate to $\approx \pm 30\,\mathrm{cm}^{-1}$.

In the MID-IR spectral range of interest for the present study, Kim et al. have investigated crystalline cellulose. The data provides spectroscopic details on its structure, chain orientation, and vibrational modes using IR, Raman, and SFG techniques[105, 95]. Moreover, cellulose acts as a valuable substrate for the initial alignment of the SFG setup, because of its ability to generate strong SFG signals that scatter in various directions. The beam alignment can be achieved with a rapid refresh rate (0.5 seconds per spectral reading), enabling real-time optimization of the SFG signal. Therefore, crystalline cellulose is chosen as our test sample.

Microcrystalline cellulose powder with a particle size of $\approx 50\,\mu\mathrm{m}$ (Sigma-Aldrich) is a pure form of cellulose that has been partially depolymerized through acid hydrolysis of specialty wood pulp. It is hand-pressed into a pellet with a diameter of 10 mm. To prevent damage, the power levels for exciting at 515 nm and MID-IR are limited to 50 mW and 10 mW, respectively. A

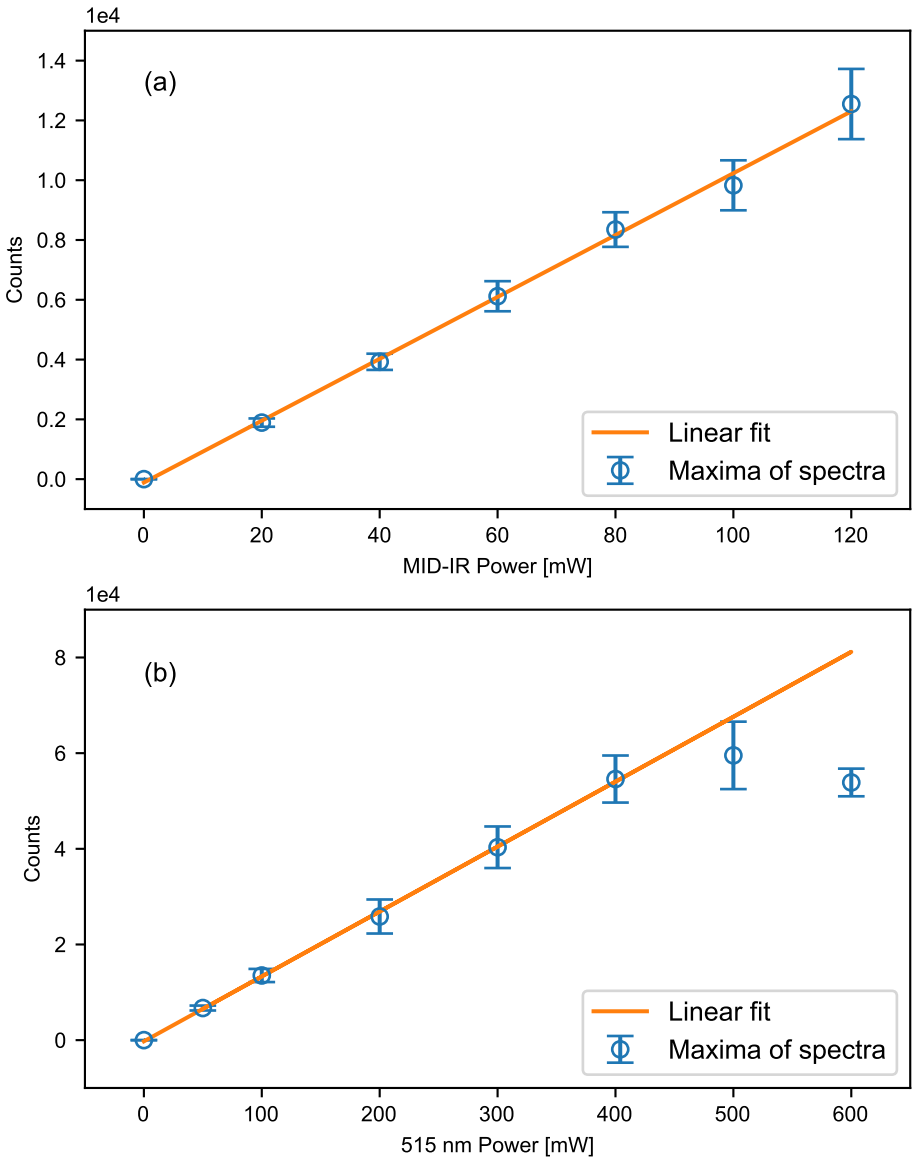

Figure 5.5: Linear fitting of the maximum values from MID-IR power dependent VSFG spectra (a) and of the maximum values from 515 nm power dependent VSFG spectra (b)

comparison between the present experimental results using VSFG spectroscopy and published data[16] on cellulose is shown in Fig.5.6. The vibrations in the range of 1000 to 1250 cm^{-1} are attributed to various C-C and C-O stretching modes, as well as C-C-H, O-C-H, and C-O-H bending modes. The peak at 1100.3 cm^{-1} is particularly sharp and useful for precise calibration. By

using a Lorentz model to fit this peak, two specific wavenumbers from our measurement and the literature can be determined. Ultimately, we can adjust our wavenumber axis by $+5.7\,\mathrm{cm}^{-1}$ to align with the $1106\,\mathrm{cm}^{-1}$ peak position from the literature for accurate calibration.

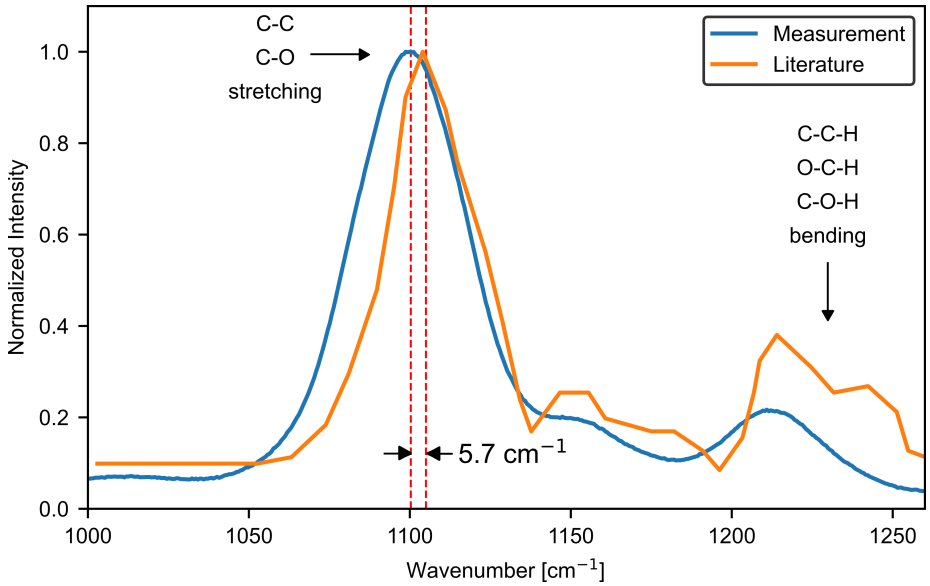

Figure 5.6: VSFG spectrum of cellulose pellet for fine spectral calibration.

5.3.3 VSFG of Glucose Pellets

Glucose, with the chemical formula $C_6H_{12}O_6$, is a vital sugar in the energy metabolism for all living organisms. It is stored as starch and amylopectin in plants and as glycogen in animals. In animals, glucose is found circulating in the blood as blood sugar. The naturally occurring form of glucose is D-glucose, while its synthetic stereoisomer, L-glucose, is less biologically active and produced in comparatively small quantities. As shown in Fig.5.7, the glucose molecule can be found in both an open-chain (acyclic) and ring (cyclic) form. In a solution, the open-chain form of glucose is in equilibrium with various cyclic isomers (pyranose and furanose forms), each with a ring of carbons closed by an oxygen atom. In an aqueous solution, over 99 % of glucose molecules are in pyranose forms. The open-chain form makes up around 0.25 %, and furanose forms are present in very small amounts. Besides, the other forms, which referred to as "$\alpha-$" and "$\beta-$", differ by the hydroxyl group position in the Haworth projection[106]. The cyclic forms of glucose are frequently referred to as D-glucose. The D-glucose powder (Sigma-Aldrich)

utilized in our experiments is hand-pressed into a pellet with a diameter of 10 mm.

In order to prevent the glucose surface from melting, the power levels used for exciting at 515 nm and MID-IR are restricted to 50 mW and 40 mW, respectively. The VSFG spectra are captured as images using a CCD camera. When dealing with optically flat surface samples like NLCs or quartz, the SFG signal can be gathered with a small vertical bin size setting, typically around 5 bins. However, for samples with highly scattering SFG signals such as glucose and cellulose, the vertical beam size on the CCD camera exceeds 200 bins. Consequently, each VSFG spectrum is obtained by averaging 150 bins in the brighter region of the image. Fig.5.8 illustrates the glucose VSFG spectra obtained using gratings with groove densities of 150, 300, and 1200 l/mm. A higher groove density results in improved spectral resolution of VSFG, resulting in the observation of distinct and multiple vibrational peaks. The increased frequency resolution allows for a more detailed analysis of the recorded spectra, but it also leads to a reduction in the maximum number of counts on the CCD. For instance, the grating with 300 l/mm has only one-tenth of the counts compared to the 150 l/mm grating. Consequently, longer exposure times are required to capture a clear image, such as 900 seconds for the 1200 l/mm grating, which has a low efficiency of 20 % at the SFG wavelengths. To optimize the signal intensity and spectral resolution of VSFG

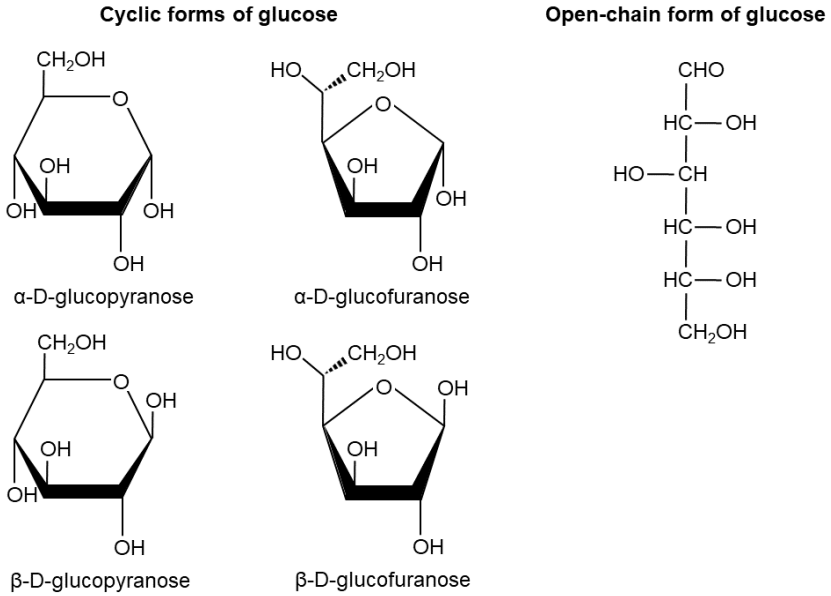

Figure 5.7: Cyclic forms and open-chain form of glucose in the Haworth projection.

for glucose samples, the 1800 l/mm grating is used. A distinct cumulative spectrum is obtained with an exposure time of 30 seconds repeated five times.

The glucose pellet VSFG spectrum is shown in Fig.5.9 (b), displaying 8 distinct vibrational modes ranging from 800 to 1400 cm^{-1}. The quartz reference spectrum in Fig.5.9 (a) suggests an optimal probing range between 1000 and 1300 cm^{-1}. However, observed peaks at 1351.2, 956.3, and 844.0 cm^{-1}, which are out of this range, indicate that our VSFG setup has a wide detecting range and a very good signal-to-noise ratio for weak signals, i.e. exhibit high sensitivity. Notably, the VSFG vibrations coincide with IR and Raman peaks, as shown by red dashed lines in Fig.5.9 (c), as each VSFG vibration results from an IR and Raman transition according to Eq.2.6.2. By comparing with

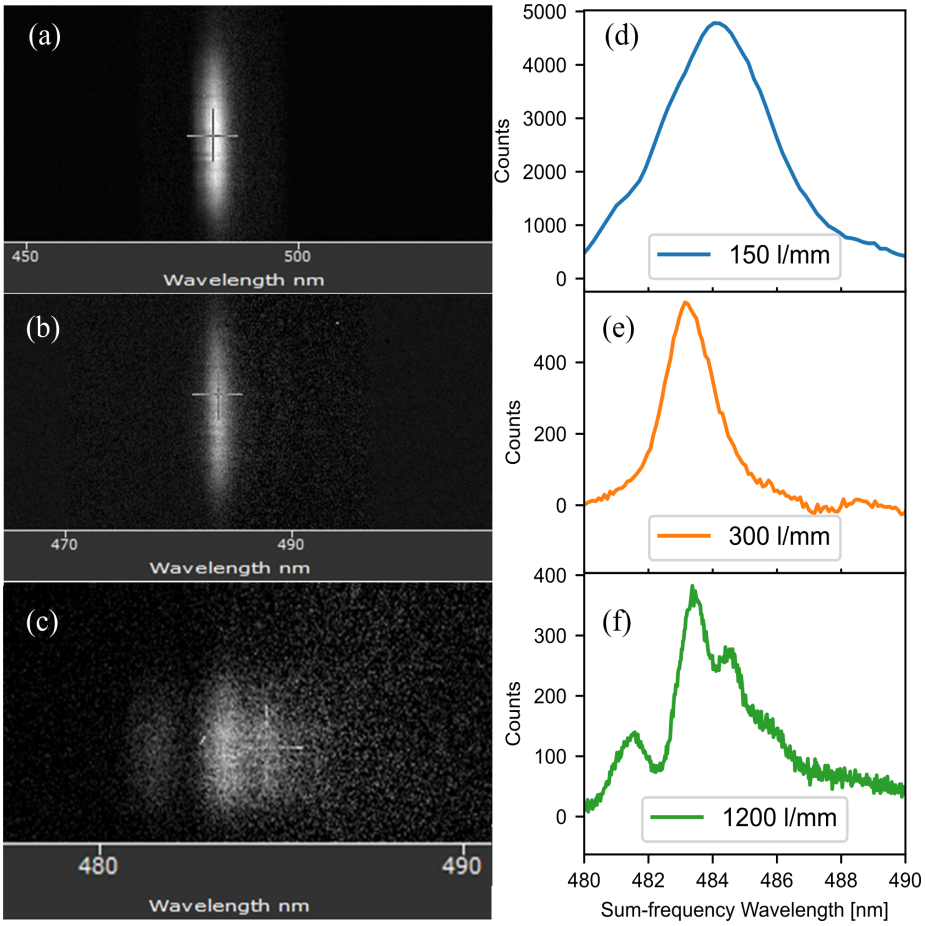

Figure 5.8: The VSFG images (a), (b), and (c) and spectra (d), (e), and (f) of glucose pellets with gratings of 150, 300, 1200 l/mm, respectively. The exposure time of measurements are both 300 seconds for 150 and 300 l/mm, but 900 seconds for 1200 l/mm due to the low grating efficiency.

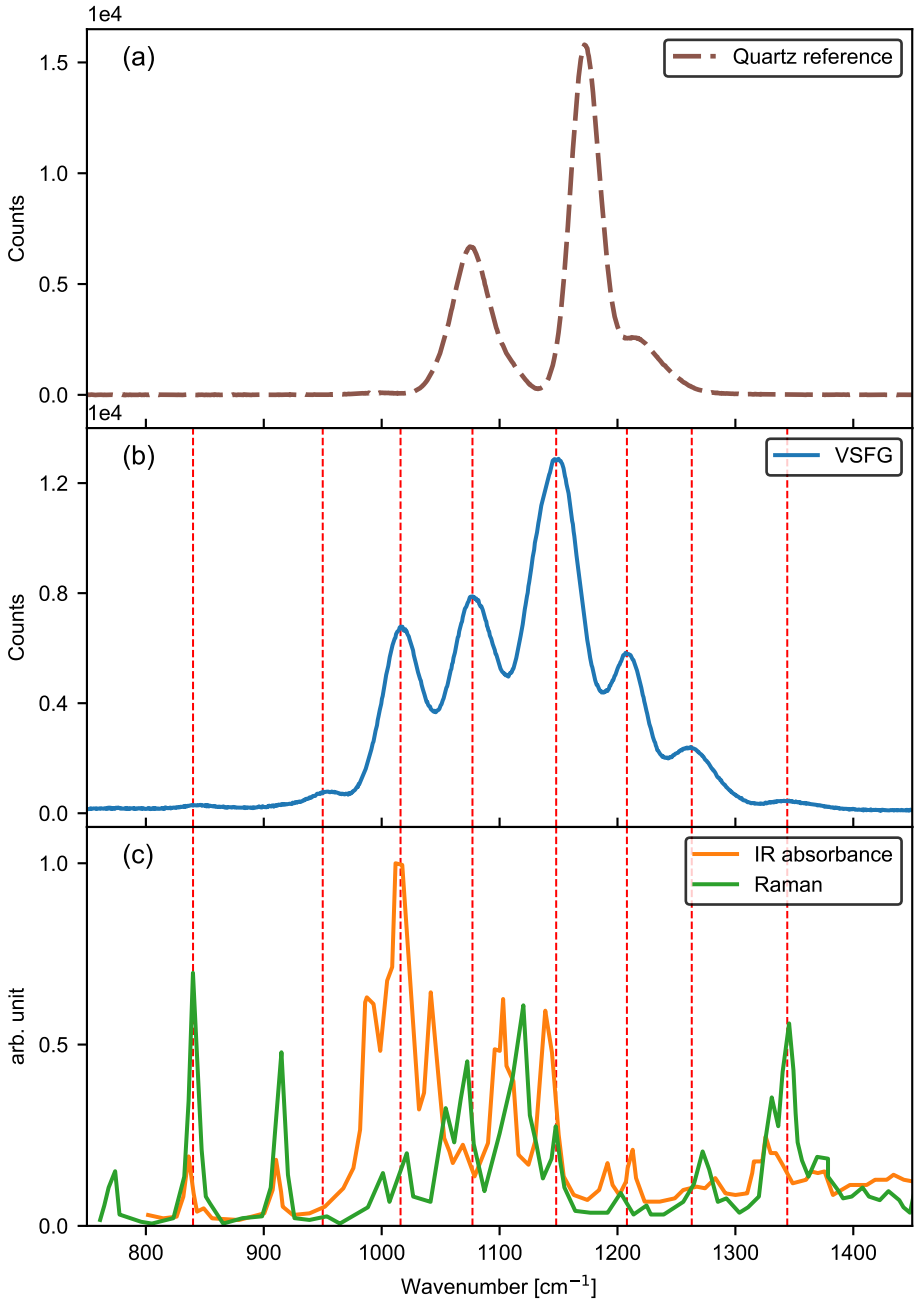

Figure 5.9: The SFG reference spectrum from quartz (a). The VSFG spectrum from glucose pellets measured with the 1800 l/mm grating (b). The observed 8 vibrational modescan be assigned to vibrational peaks in IR and Raman spectra from the online database[107, 108] (c). The red dashed lines indicate the positions of VSFG resonant frequencies.

the IR and Raman literatures of glucose[109, 110], the VSFG vibrational modes can be easily assigned, as detailed in Tab.5.2. Because the MID-IR pulse has nonuniform spectral intensity, determining the intrinsic amplitudes of the vibrational modes involves dividing the VSFG signal spectrum by the quartz nonresonant reference spectrum. However, this approach has not been applied here, because of the central dip in the MID-IR spectral pulse profile and the observed phonon bands in the quartz SFG response spectrum. In particular, weak vibrational structures might be obscured by noise at the processed spectrum's rising and falling edges, where the MID-IR pulse spectral intensity is close to zero.

Vibrational modes between 1000 and 1200 cm^{-1} have been used in the following to detect low concentrations (< 10 mM) of glucose in aqueous solution. Specifically, the C-O stretching mode at 1015.6 cm^{-1} is IR sensitive[89], while the C-O-H bending mode at 1147.5 cm^{-1} is Raman active[91], making them key indicators for monitoring concentration changes in glucose solutions.

5.3.4 VSFG of Glucose in Aqueous Solution

A healthy individual typically has a blood sugar level ranging from 4 to 6 mM when fasting and less than 8 mM after eating. For diabetics, the recommended range is between 5 and 7 mM when fasting and less than 10 mM after meals. Hypoglycemia is diagnosed when blood sugar levels drop below 3 mM, leading to symptoms like clumsiness, confusion, and seizures. On the other hand,

Vibrational frequency [cm^{-1}]	Line width [cm^{-1}]	Amplitude [a.u.]	Vibrational mode reference
1351.2	7.77	0.25	CH_2 wagging
1265.2	16.51	6.42	CH_2 twisting
1211.2	13.39	13.12	CH_2 twisting
1147.5	24.79	75.92	C-O-H bending
1076.8	18.59	28.09	C-O stretching
1015.6	18.62	27.33	C-O stretching
956.3	23.81	3.85	C-O-H bending
844.0	17.30	0.61	C-O stretching

Table 5.2: The fitting parameters of the intensity-normalized VSFG spectrum from glucose pellet by 8 Lorentz models.

hyperglycemia occurs when blood sugar levels exceed 11 mM, resulting in symptoms such as excessive thirst, hunger, fatigue, and increased urination. Therefore, the glucose concentrations range from 3 to 11 mM are the main measuring targets for developing VSFG as a concentration sensing technique. Various concentrations (from 400 to 10 mM) of Glucose in aqueous solution are prepared by dissolving different amounts of glucose in 100 ml of deionized water. For instance, a concentration of 10 mM is made by dissolving 180 mg of glucose powder. Additionally, a saturated solution (> 1000 mM) is prepared for the initial detection of signal due to its stronger VSFG intensity.

A demountable liquid cell (Specac Ltd.) is utilized to sandwich the glucose solution between two BaF_2 windows with a 5 mm thick spacer. The high transparency of the solution allows for the measurement of the transmitted SFG, which is more intense than the reflected SFG. Following the developed successful measurement strategy, the transmitted quartz SFG reference spectrum must be obtained first. It is important to optimize the spatial and temporal overlaps again to deal with the slight shifts caused by differences in refractive indexes and group delays of the 515 nm and MID-IR beams in the BaF_2 window. After that, the quartz is replaced by the glucose solution with minimal changes to the liquid cell setup. Due to the low solubility of BaF_2 in water (1.61 g/l at 25°C), window transparency decreases over time. To compensate for this effect, higher pumping power levels of 515 nm and MID-IR at 1 W and 120 mW, respectively, are utilized for the solutions. Note, blurred BaF_2 windows in the solution experiments result in reduced transparency. To compensate for this effect, rather high pumping power are chosen assuming that the glucose interaction is still below saturation. Since the SFG signal from liquid samples is generally weaker than that from solid samples, a longer exposure time of 30 minutes is required to achieve a satisfactory signal-to-noise ratio spectrum.

Fig.5.10 (b) displays the two VSFG spectra of the saturated glucose solution when excited by two MID-IR spectral profiles shown in Fig.5.10 (a). The VSFG spectra of the quartz reference and the saturated solution are presented with dashed and solid lines of the same color, respectively. The high intensity 515 nm pumping leaks through the bandpass filter affecting the spectral region below 1000 cm^{-1}. It makes the analysis in the highlighted spectral range challenging. To mitigate the leakage background, the spectrometer's detection range is limited to 1010 cm^{-1} by controling the grating when measuring the orange spectra. The wavelength drive hardware sets the system to the target wavelength and also allows control of the grating selection. On the one hand, the VSFG spectrum of the saturated solution shown in green exhibits at least three vibrational modes between 1000 and 1400 cm^{-1}, resembling the characteristics of the glucose pellet VSFG spectrum presented in Fig.5.9 (b).

On the other hand, the corresponding VSFG spectrum excited by a lower central frequency of MID-IR pulse shows a distinct vibration at 1035 cm^{-1}, corresponding exactly to the IR-sensitive C-O stretching mode[89, 90].

It is important to note that, a flat spectrum shown in grey from deionized water is recorded to confirm that the observed vibrational structure originated from the glucose molecules. The data indicate that the SFG signal of water at the BaF_2 interface is at or near the noise background level. Moreover, some dissolution is expected, when a BaF_2 surface is exposed to liquid water. Experiments carried out by Khatib et al. could show how the pH value of water affects the recorded VSFG signal from a similar CaF_2/water interface

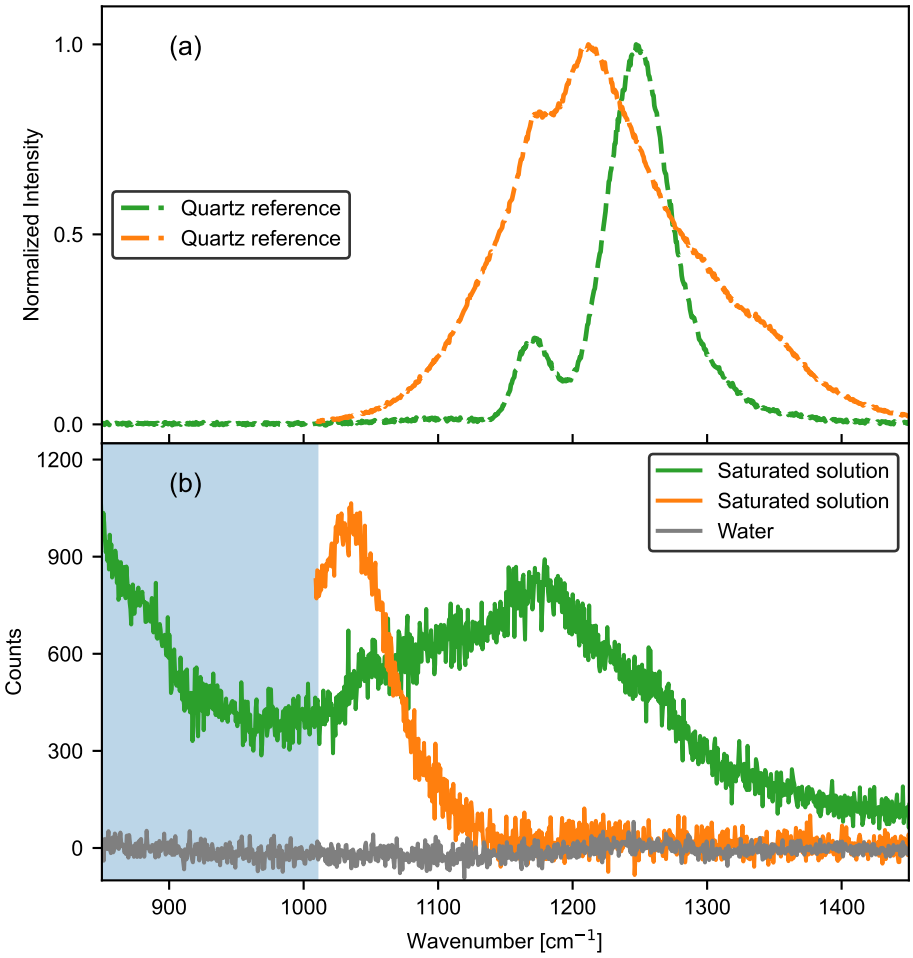

Figure 5.10: The SFG reference spectra from quartz (a). The VSFG spectra from the saturated glucose solution and water (b). The blue area shows where the VSFG spectra are affected by significant background signal on the CCD chip originating from the VIS beam.

in the spectral range from 2800 to 3200 cm^{-1} [111]. At low pH, a positively charged fluoride vacancy $(FCa^{+})_{surf}$ is created at the crystal surface because of the excess of hydronium ions. At high pH, the hydroxide ions are expected to react with CaF_2 leading to $(CaFOH)_{interf}$ at the interface. However, at neutral pH the interface carries little charge as only a minor amount of CaF_2 will dissolve and the VSFG signal vanishes as the result of a more random orientation of the interfacial water molecules[111]. This is consistent with our measurements, where we don't observe SFG signal from the BaF_2/water interface between 900 and 1400 cm^{-1}.

Next, VSFG spectra of glucose concentrations at 400 and 10 mM, which

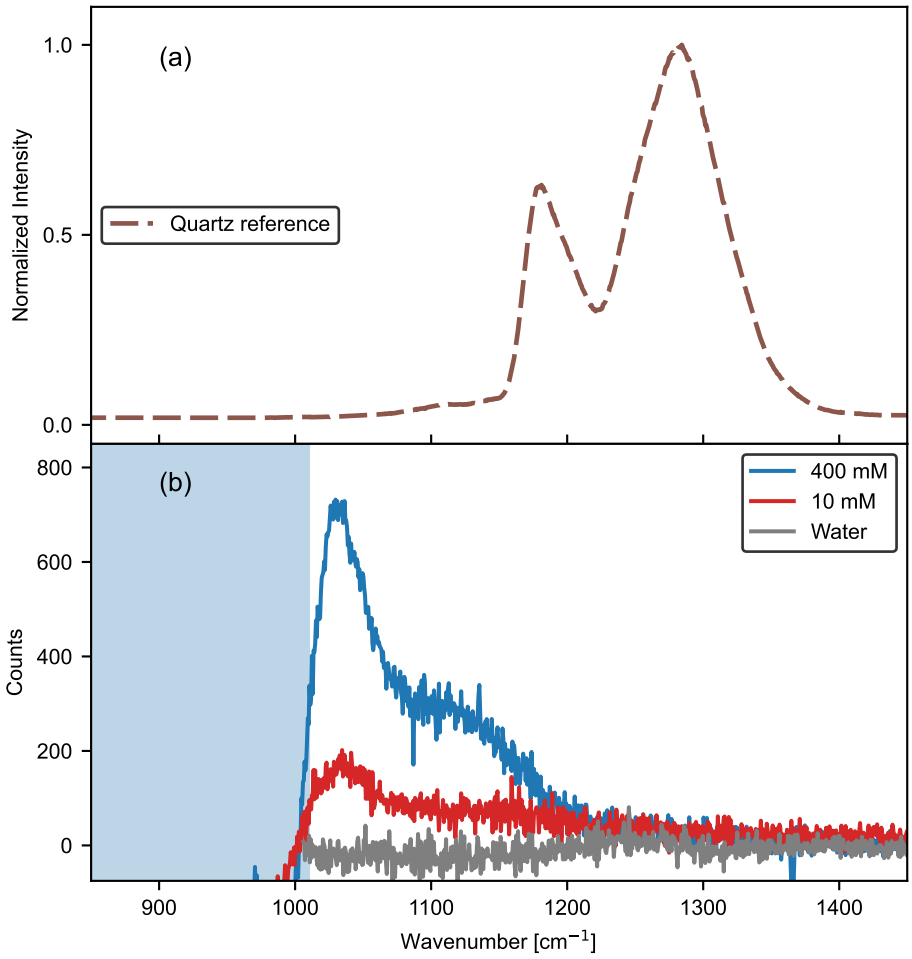

Figure 5.11: The SFG reference spectra from quartz (a). The VSFG spectra from the glucose solution of 400 and 10 mM (b). The blue area shows where the VSFG spectra are affected by significant background signal and stray light, respectively.

are pumped by the same MID-IR spectral profile, are measured and shown in Fig.5.11 (a) and (b). Both spectra show the characteristic C-O stretching mode at 1035 cm^{-1}. Its signal strength depends on the glucose concentration. The fitting parameters for the C-O stretch vibration in different solutions can be found in Tab.5.3. It is worthy to mention that glucose adsorption on the BaF_2 window could form Ba-O and hydrogen bonds at the solid-liquid interface of the liquid cell[112]. Thus, we cannot exclude that the signal strength of the C-O stretch vibration could be affected to some extent by both, the glucose concentration and adsorption at the interface. In any case, our data clearly demonstrates that the VSFG peak can be employed for detecting low glucose concentrations in aqueous solution with high sensitivity. The data benchmark the performance of the spectrometer for spectral fingerprinting of low-concentration specimen at complex interfaces.

Glucose solution [mM]	Vibrational frequency [cm^{-1}]	Line width [cm^{-1}]	Amplitude [a.u.]
> 1000 (saturated solution)	1034.6*	32.72	107163.14
400	1033.4*	23.62	47046.50
	1113.7	59.08	47815.19
10	1035.2*	24.69	10227.41
	1134.4	84.78	13277.83

Table 5.3: The fitting parameters of the VSFG spectrum from glucose solutions by Lorentz models. The IR sensitive peaks of the three solutions are denoted with *. The peaks at 1113.7 and 1134.4 cm^{-1} are assigned to the C-O-H bending mode[91].

Chapter 6

Conclusion and Outlook

In the present work, the optical characteristics of lithium-based nonlinear crystals for MID-IR generation have been examined under high-power laser irradiation at 1030 nm wavelength using thermal imaging techniques. The LGS crystal stands out due to its low linear/nonlinear absorption coefficients and high optical damage threshold, making it an ideal candidate for high-power few-cycle MID-IR pulse generation. In recent years, some novel materials also show promises of MID-IR generation beyond 10 µm such as $BaGa_4S_7$[86] and $Cd_{0.65}Hg_{0.35}Ga_2S_4$[113]. Another interesting avenue is to employ a high-power 2 µm laser for driving an OPCPA laser system. For instance, generating MID-IR pulses at 7 µm with pulse energies reaching mJ levels has been achieved by using the highly nonlinear crystal $ZnGeP_2$ ($d_{eff} \approx 75$ pm/V) pumped at 2 µm[42]. However, the main challenge lies in enhancing the pulse energy and average power of these 2 µm pump lasers further to fully utilize the significant effective nonlinearity of the available nonlinear crystals.

Moreover, a versatile home-built MID-IR OPCPA laser system has been developed using the identified superior performing LGS crystal. This system has been fully characterized and offers two different modes of operation: wavelength-tunable and few-cycle schemes. Both modes generate MID-IR ultrashort pulses with high average power exceeding 200 mW and a pulse energy of 1.2 µJ at 200 kHz. By increasing the AMPHOS laser power used for pumping the OPCPA to 200 W at 1 MHz, the OPCPA system could achieve an average power of over 2 W at the same pulse energy level without causing damage to optics and the LGS nonlinear crystal.

As a first application of the developed MID-IR laser system, the vibrations of glucose in solid form and in aqueous solution have been first studied by vibrational sum-frequency generation (VSFG) spectroscopy. Developing VSFG as a tool for blood sugar sensing was the key goal of the present thesis and has been accomplished by demonstrating glucose sensing on the C-O

stretch vibration at $1035\,\mathrm{cm}^{-1}$ in the biologically relevant concentration range from 3 to 11 mM.

From a technical point of view, it turned out that detector saturation due to strong excitation pulse contributions below $1000\,\mathrm{cm}^{-1}$ makes it challenging to analyse the data and limits achievable the signal-to-noise ratio in the present setup. This might be adressed in future by reducing the 515 nm pump intensity and increasing the MID-IR intensity using a smaller beam diameter of $\approx 25\,\mu\mathrm{m}$. This would also shorten the measurement time from 30 minutes to just a few seconds. Additionally, slight variations in sample position and angle are inevitable when disassembling the liquid cell and changing solution concentrations. Therefore, a stable, sealed liquid cell that allows glucose solutions to flow in from outside is crucial for concentration-dependent measurements. Since the surfaces of BaF_2 windows solvated in water become blurred within 24 hours, all measurements should be conducted promptly to compare vibrational peak amplitudes across different glucose concentrations.

Last but not least, more detailed studies on biomolecules in the spectral fingerprint region will become possible by applying advanced experimental techniques such as time-resolved VSFG spectroscopy and VSFG microscopy.

Chapter 7

Appendix

7.1 Calculation of High-order Dispersion

Dispersion management is a critical aspect of OPCPA design, involving the manipulation of pulse duration through stretching and compressing. When the dispersion within the pulse is minimized, the pulse duration will closely approach the Fourier-transform limit of the spectrum. Tab.7.1 provides parameters for dispersion nduced by NLCs and optical lenses in the OPCPA systems. The calculation of pulse dispersion involves summing up individual dispersion values. It is important to highlight that the cumulative GDD is added into the chirped signal pulse before the DFG stage using the LGS crystal. During the DFG process, higher signal frequencies are transformed into lower idler frequencies, and vice versa. If the rainbow spectrum in Fig.2.4 indicates a chirped signal pulse, the rainbow will be horizontally inverted in the idler spectrum. Consequently, following the DFG stage, a positively chirped signal pulse will be converted into a negatively chirped idler pulse.

In the case of the negatively chirped signal scheme, the GDD of $+11000\,\mathrm{fs}^2$ induced by the chirped mirrors in the MID-IR Idler are almost removed by the LGS crystal, which gives -10467.88 fs^2 GDD, and acts as a pulse width compressor. Therefore, the remaining GDD of -2176.03 fs^2 can be easily offset by a 3 mm thick ZnSe bulk. On the other hand, the idler generated by the positively chirped signal scheme still retains a significant GDD of -23582.60 fs^2, requiring a minimum of a 60 mm thick Ge bulk for compensation. However, such a thick Ge bulk also gives a big amount of TOD and FOD, causing a significant distortion of the pulse shape. Therefore, the effective compression of the MID-IR pulse width in this scheme is not available.

Stage	Crystal	n	GD [fs]	GDD [fs^2]	TOD [fs^3]	FOD [fs^4]
OPCPA	YAG 10.0 mm	1.81	61.15	539.68	776.16	-762.40
	BBO 3.0 mm	1.65	16.74	109.48	203.78	-216.17
	Fused Silica 8.0 mm	1.45	39.01	86.08	424.35	-708.06
	SF11 100.0 mm	1.75	594.01	10406.57	12494.59	-6561.98
	Chipred Mirrors	–	–	-11000	–	–
	LGS 5.0 mm	2.05	36.5	-10467.88	154160.90	-2992094.08
	ZnSe 3.0 mm	2.41	24.60	-1972.91	34380.41	-705597.37
+GDD scheme: Dispersion in MID-IR pulse			772.01	-23582.60	202440.19	-3705940.06
-GDD scheme: Dispersion in MID-IR pulse			178*	-2176.03*	189945.60*	-3699378.08*
cross-correlation	KBr 17.0 mm	1.53	87.61	-3960.60	59449.71	-1129063.93

Table 7.1: The dispersion management in the MID-IR OPCPA. The parameters in the negatively chirped scheme, which are denoted with *, will be used for the deconvolution of the recorded cross-correlation trace. n: Refractive index; GD: Group delay; GDD: Group delay dispersion; TOD: Third-order dispersion; FOD: Fourth-order dispersion.

7.2 Deconvolution of the Recorded MID-IR Cross-correlation Trace

From Eq.2.2.17, we learn that a spectral phase ϕ is accumulated by monochromatic propagating waves. The dependence of ϕ on ω determines the pulse dispersion, which is given by Eq.2.4.1. Based on the above equations, a Matlab program provided by Dr. Mark J. Prandolini can simulate the pulse width of MID-IR pulses. This program can generate the theoretical temporal shape and pulse width by using the MID-IR spectrum and the dispersion parameters. For example, a chirped MID-IR pulse width of 1042 fs generated by the positively chirped signal scheme is derived using the broad MID-IR spectrum shown in Fig.4.10 (b) and the dispersion parameters listed in Tab.7.1. In the same way, based on the MID-IR spectrum displayed in Fig.7.1 (a) and the parameters for negatively chirped signal scheme, a theoretical pulse width can be obtained. Additionally, the program can simulate the convolution of unchirped and chirped MID-IR pulses measured in our home-built cross-correlator, as depicted in Fig.2.4 (b), by providing the KBr dispersion values of the optics.

The width τ_{cc} (FWHM) of the measured cross-correlation trace is 194 fs as shown in Fig.7.1 (b). Higher-order dispersion such as TOD and FOD affect the temporal shape, but the pulse width is primarily determined by GDD. By varying the GDD from -2000 to 5500 fs^2, the program calculates the theoretical widths of pulse 1 (with zero dispersion from KBr), pulse 2 (with additional dispersion from KBr), and their cross-correlation width, as depicted in Fig.7.2. The 194 fs width, indicated by the horizontal dashed line, corresponds to a residual GDD value of -300 fs^2 in pulse 1 and a pulse width τ_p of 74 fs, which is close to the transform limit of 68 fs.

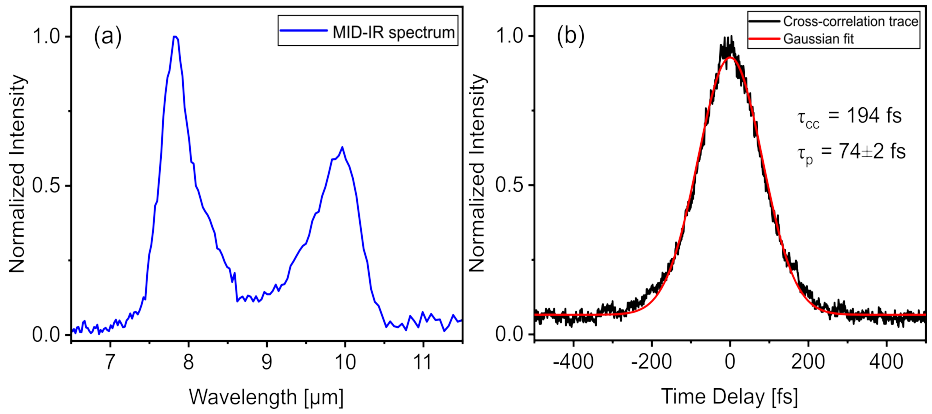

Figure 7.1: MID-IR spectrum (a), cross-correlation trace and Gaussain fit (b).

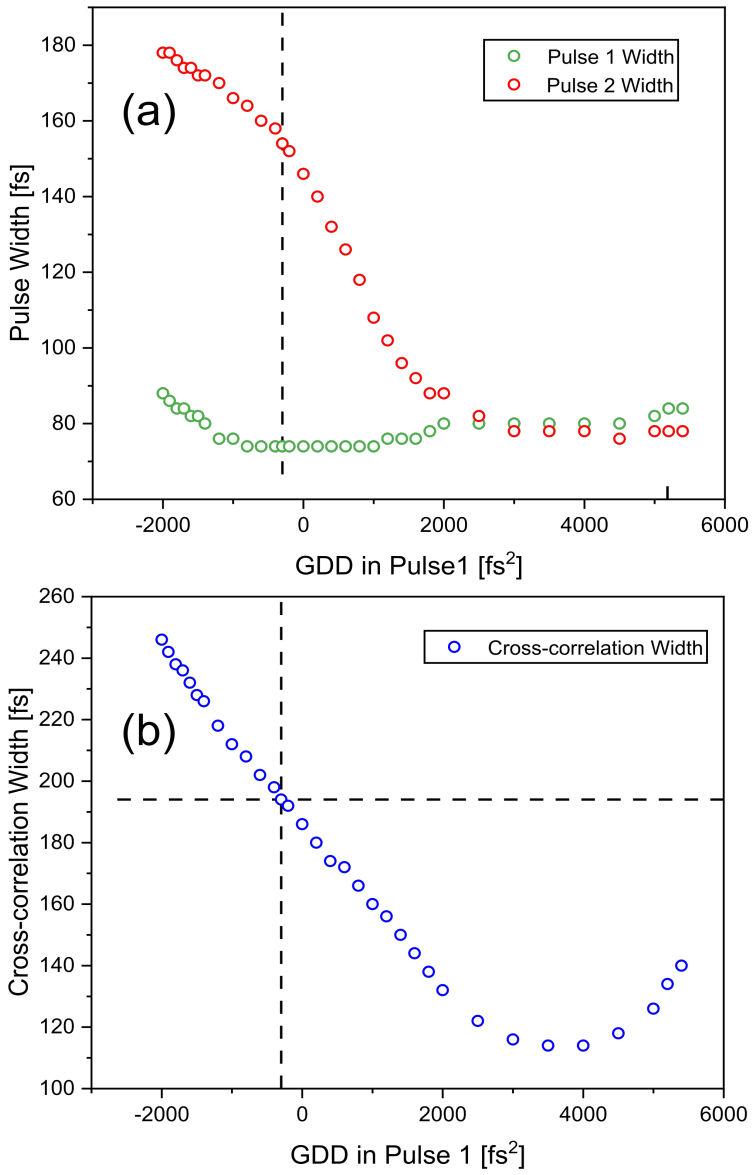

Figure 7.2: Pulse 1 and pulse 2 width (a) and cross-correlation width (b) are simulated as a function of GDD. The black dashed line indicates the width of the experimental cross-correlation width and the corresponding pulse 1 and pulse 2 widths, respectively.

List of Publications

Spectral fingerprinting of aqueous glucose with ultra-broadband vibrational sum-frequency generation spectroscopy at bio-relevant low concentration

C. Luo, M. Namboodiri, M. Schulz, R. Riedel, M. J. Prandolini, and T. Laarmann
Opt. Express 33, 6080-6091 (2025), DOI: 10.1364/OE.544862.

Versatile few-cycle high-energy MID-IR OPCPA for nonlinear optics, spectroscopy and imaging

M. Namboodiri, **C. Luo**, G. Indorf, J. H. Buss, M. Schulz, R. Riedel, M. J. Prandolini, and T. Laarmann
Opt. Continuum 1, 1157-1164 (2022), DOI: 10.1364/OPTCON.451879.

Optical properties of Li-based nonlinear crystals for high power mid-IR OPCPA pumped at 1 μm under realistic operational conditions

M. Namboodiri, **C. Luo**, G. Indorf, T. Golz, I. Grguraš, J. H. Buss, M. Schulz, R. Riedel, M. J. Prandolini, and T. Laarmann
Opt. Mater. Express 11, 231-239 (2021), DOI: 10.1364/OME.414478.

Acknowledgements

I would like to express my gratitude to my supervisor, Tim Laarmann, for providing me with numerous opportunities for personal and academic growth throughout my doctoral studies.

I am also thankful to my colleagues from the X-ray Femtochemistry and Cluster Physics Group, including Mahesh Namboodiri, Andreas Przystawik, Slawomir Skruszewicz, Samuel Hartwell, David Schwickert, Malte Sumfleth, Dian Diaman, Hsuan-Chun Yao, and Marcel Brockmann, as well as the partners from Class 5 Photonics: Gregor Indorf, Bastian Manschwetus, Mark J. Prandolini, and Michael Schulz.

Furthermore, I extend my appreciation to my family members, Yen-chu, Jian-xin, Yin and my parent, for their consistent support and encouragement. I also appreciate the prayers and fellowships from the churches in Hamburg, Taipei, and Hsinchu.

Finally, I would like to give thanks to my Lord Jesus Christ for His abundant grace, which has helped me overcome all challenges and obstacles in these years.

Bibliography

[1] M. Huber et al. "Infrared molecular fingerprinting of blood-based liquid biopsies for the detection of cancer". In: *eLife* 10 (2021), p. 68758. DOI: 10.7554/eLife.68758.

[2] *International Diabetes Federation*. 2024. URL: https://idf.org/about-diabetes/diabetes-facts-figures/.

[3] T. Kitazaki et al. "Glucose emission spectra through mid-infrared passive spectroscopic imaging of the wrist for non-invasive glucose sensing". In: *Scientific Reports* 12.1 (2022), p. 20558. DOI: 10.1038/s41598-022-25161-x.

[4] J. W. Kang et al. "Direct observation of glucose fingerprint using in vivo Raman spectroscopy". In: *Science Advances* 6.4 (2020), p. 5206. DOI: 10.1126/sciadv.aay5206.

[5] X. Wang et al. "Glucose concentration measured by the hybrid coherent anti-Stokes Raman-scattering technique". In: *Phys. Rev. A* 81 (2010), p. 013813. DOI: 10.1103/PhysRevA.81.013813.

[6] A. Golparvar et al. "Rapid, Sensitive and Selective Optical Glucose Sensing with Stimulated Raman Scattering (SRS)". In: *2022 IEEE International Symposium on Medical Measurements and Applications (MeMeA)*. 2022, pp. 1–5. DOI: 10.1109/MeMeA54994.2022.9856428.

[7] M. Huber et al. "Detection sensitivity of field-resolved spectroscopy in the molecular fingerprint region". In: *2017 CLEO/Europe-EQEC*, p. 1. DOI: 10.1109/CLEOE-EQEC.2017.8086921.

[8] J. Diels and W. Rudolph. *Ultrashort Laser Pulse Phenomena: Fundamentals, Techniques, and Applications on a Femtosecond Time Scale*. Academic Press, 2006. URL: https://www.sciencedirect.com/book/9780122154935/ultrashort-laser-pulse-phenomena#book-info.

[9] R. W. Boyd. *Nonlinear Optics*. Academic Press, 2008. URL: https://www.sciencedirect.com/book/9780123694706/nonlinear-optics.

[10] C. Manzoni and G. Cerullo. "Design criteria for ultrafast optical parametric amplifiers". In: *Journal of Optics* 18.10 (2016), p. 103501. DOI: 10.1088/2040-8978/18/10/103501.

[11] D. Strickland and G. Mourou. "Compression of amplified chirped optical pulses". In: *Optics Communications* 56.3 (1985), pp. 219–221. DOI: 10.1016/0030-4018(85)90120-8.

[12] K. A. Tanaka et al. "Current status and highlights of the ELI-NP research program". In: *Matter and Radiation at Extremes* 5.2 (2020), p. 024402. DOI: 10.1063/1.5093535.

[13] R. Paschotta. *Mid-infrared Spectrometers*. RP Photonics Encyclopedia. DOI: 10.61835/fw4.

[14] M. Piccardo et al. "Mid-infrared two-photon absorption in an extended-wavelength InGaAs photodetector". In: *Applied Physics Letters* 112.4 (2018), p. 041106. DOI: 10.1063/1.5018619.

[15] C. Luo et al. "Spectral fingerprinting of aqueous glucose with ultra-broadband vibrational sum-frequency generation spectroscopy at bio-relevant low concentration". In: *Opt. Express* 33.3 (2025), pp. 6080–6091. DOI: 10.1364/OE.544862.

[16] C. M. Lee et al. "Multimodal Broadband Vibrational Sum Frequency Generation (MM-BB-V-SFG) Spectrometer and Microscope". In: *The Journal of Physical Chemistry B* 120.1 (2016), pp. 102–116. DOI: 10.1021/acs.jpcb.5b10290.

[17] D. E. Gragson and G. L. Richmond. "Investigations of the Structure and Hydrogen Bonding of Water Molecules at Liquid Surfaces by Vibrational Sum Frequency Spectroscopy". In: *The Journal of Physical Chemistry B* 102.20 (1998), pp. 3847–3861. DOI: 10.1021/jp9806011.

[18] G. L. Richmond. "Molecular Bonding and Interactions at Aqueous Surfaces as Probed by Vibrational Sum Frequency Spectroscopy". In: *Chemical Reviews* 102.8 (2002), pp. 2693–2724. DOI: 10.1021/cr0006876.

[19] A. G. Lambert, P. B. Davies, and D. J. Neivandt. "Implementing the Theory of Sum Frequency Generation Vibrational Spectroscopy: A Tutorial Review". In: *Applied Spectroscopy Reviews* 40.2 (2005), pp. 103–145. DOI: 10.1081/ASR-200038326.

[20] X. Zhuang et al. "Mapping molecular orientation and conformation at interfaces by surface nonlinear optics". In: *Phys. Rev. B* 59 (1999), pp. 12632–12640. DOI: 10.1103/PhysRevB.59.12632.

[21] J. Pickering. *SFG Local Field Correction Factors*. 2021. URL: https://github.com/james-d-pickering/SFG_localfieldfactors.git.

[22] J. D. Pickering et al. "Tutorials in vibrational sum frequency generation spectroscopy. II. Designing a broadband vibrational sum frequency generation spectrometer". In: *Biointerphases* 17.1 (2022), p. 011202. DOI: 10.1116/6.0001403.

[23] S. Qu et al. "9 μm few-cycle optical parametric chirped-pulse amplifier based on $LiGaS_2$". In: *Opt. Lett.* 44.10 (2019), pp. 2422–2425. DOI: 10.1364/OL.44.002422.

[24] M. A. Jakob et al. "Generation and characterization of tailored MIR waveforms for steering molecular dynamics". In: *Opt. Express* 27.19 (2019), pp. 26979–26988. DOI: 10.1364/OE.27.026979.

[25] T. Südmeyer et al. "High-power femtosecond fiber-feedback optical parametric oscillator based on periodically poled stoichiometric LiTaO3". In: *Opt. Lett.* 29.10 (2004), pp. 1111–1113. DOI: 10.1364/OL.29.001111.

[26] F. Mörz et al. "Multi-Watt femtosecond optical parametric master oscillator power amplifier at 43 MHz". In: *Opt. Express* 23.18 (2015), pp. 23960–23967. DOI: 10.1364/OE.23.023960.

[27] T. Steinle et al. "Ultra-stable high average power femtosecond laser system tunable from 1.33 to 20 μm". In: *Opt. Lett.* 41.21 (2016), pp. 4863–4866. DOI: 10.1364/OL.41.004863.

[28] F. Adler et al. "Phase-stabilized, 1.5 W frequency comb at 2.8−4.8 μm". In: *Opt. Lett.* 34.9 (2009), pp. 1330–1332. DOI: 10.1364/OL.34.001330.

[29] I. Pupeza et al. "High-power sub-two-cycle mid-infrared pulses at 100 MHz repetition rate". In: *Nature Photonics* 9.11 (2015), pp. 721–724. DOI: 10.1038/nphoton.2015.179.

[30] A. Schliesser, N. Picqué, and T. W. Hänsch. "Mid-infrared frequency combs". In: *Nature Photonics* 6.7 (2012), pp. 440–449. DOI: 10.1038/nphoton.2012.142.

[31] F. Bach et al. "Laser induced damage studies of $LiNbO_3$ using 1030 nm, ultrashort pulses at 10-1000 kHz". In: *Opt. Mater. Express* 7.1 (2017), pp. 240–252. DOI: 10.1364/OME.7.000240.

[32] F. Bach et al. "High repetition rate, femtosecond and picosecond laser induced damage thresholds of Rb:$KTiOPO_4$ at 1.03 μm". In: *Opt. Mater. Express* 7.3 (2017), pp. 744–750. DOI: 10.1364/OME.7.000744.

[33] O. Novák et al. "Femtosecond 8.5 µm source based on intrapulse difference-frequency generation of 2.1 µm pulses". In: *Opt. Lett.* 43.6 (2018), pp. 1335–1338. DOI: 10.1364/OL.43.001335.

[34] M. Beutler et al. "Difference-frequency generation of ultrashort pulses in the mid-IR using Yb-fiber pump systems and $AgGaSe_2$". In: *Opt. Express* 23.3 (2015), pp. 2730–2736. DOI: 10.1364/OE.23.002730.

[35] M. Knorr et al. "Phase-locked multi-terahertz electric fields exceeding 13 MV/cm at a 190 kHz repetition rate". In: *Opt. Lett.* 42.21 (2017), pp. 4367–4370. DOI: 10.1364/OL.42.004367.

[36] C. Gaida et al. "Watt-scale super-octave mid-infrared intrapulse difference frequency generation". In: *Light: Science & Applications* 7.1 (2018), p. 94. DOI: 10.1038/s41377-018-0099-5.

[37] J. Zhang et al. "Multi-mW, few-cycle mid-infrared continuum spanning from 500 to 2250 cm^1". In: *Light: Science & Applications* 7.2 (2018), pp. 17180–17180. DOI: 10.1038/lsa.2017.180.

[38] G. M. Archipovaite et al. "Efficient few-cycle mid-IR pulse generation in the 5-11 µm window driven by an Yb amplifier". In: *Laser Congress 2017 (ASSL, LAC)*. Optica Publishing Group. DOI: 10.1364/ASSL.2017.AM4A.4.

[39] A. A. Lanin et al. "Multioctave, 3-18 µm sub-two-cycle supercontinua from self-compressing, self-focusing soliton transients in a solid". In: *Opt. Lett.* 40.6 (2015), pp. 974–977. DOI: 10.1364/OL.40.000974.

[40] H. Liang et al. "High-energy mid-infrared sub-cycle pulse synthesis from a parametric amplifier". In: *Nature Communications* 8.1 (2017), p. 141. DOI: 10.1038/s41467-017-00193-4.

[41] L. v. Grafenstein et al. "5 µm few-cycle pulses with multi-gigawatt peak power at a 1 kHz repetition rate". In: *Opt. Lett.* 42.19 (2017), pp. 3796–3799. DOI: 10.1364/OL.42.003796.

[42] D. Sanchez et al. "7 µm, ultrafast, sub-millijoule-level mid-infrared optical parametric chirped pulse amplifier pumped at 2 µm". In: *Optica* 3.2 (2016), pp. 147–150. DOI: 10.1364/OPTICA.3.000147.

[43] T. Kanai et al. "Parametric amplification of 100 fs mid-infrared pulses in $ZnGeP_2$ driven by a Ho:YAG chirped-pulse amplifier". In: *Opt. Lett.* 42.4 (2017), pp. 683–686. DOI: 10.1364/OL.42.000683.

[44] V. Petrov. "Parametric down-conversion devices: The coverage of the mid-infrared spectral range by solid-state laser sources". In: *Optical Materials* 34.3 (2012), pp. 536–554. DOI: 10.1016/j.optmat.2011.03.042.

[45] M. Seidel et al. "Multi-watt, multi-octave, mid-infrared femtosecond source". In: *Science Advances* 4.4 (2018), p. 1526. DOI: 10.1126/sciadv.aaq1526.

[46] S. B. Penwell, L. Whaley-Mayda, and A. Tokmakoff. "Single-stage MHz mid-IR OPA using $LiGaS_2$ and a fiber laser pump source". In: *Opt. Lett.* 43.6 (2018), pp. 1363–1366. DOI: 10.1364/OL.43.001363.

[47] B.-H. Chen et al. "Octave-spanning single-cycle middle-infrared generation through optical parametric amplification in $LiGaS_2$". In: *Opt. Express* 27.15 (2019), pp. 21306–21318. DOI: 10.1364/OE.27.021306.

[48] B.-H. Chen, T. Nagy, and P. Baum. "Efficient middle-infrared generation in $LiGaS_2$ by simultaneous spectral broadening and difference-frequency generation". In: *Opt. Lett.* 43.8 (2018), pp. 1742–1745. DOI: 10.1364/OL.43.001742.

[49] K. Kaneshima et al. "Generation of carrier-envelope phase-stable mid-infrared pulses via dual-wavelength optical parametric amplification". In: *Opt. Express* 24.8 (2016), pp. 8660–8665. DOI: 10.1364/OE.24.008660.

[50] L. Isaenko et al. "Growth and properties of $LiGaX_2$ (X = S, Se, Te) single crystals for nonlinear optical applications in the mid-IR". In: *Crystal Research and Technology* 38.3-5 (2003), pp. 379–387. DOI: 10.1002/crat.200310047.

[51] M. Mero et al. "Laser-induced damage of nonlinear crystals in ultrafast, high-repetition-rate, mid-infrared optical parametric amplifiers pumped at 1 µm". In: International Society for Optics and Photonics. SPIE, 2019, p. 1106307. DOI: 10.1117/12.2540125.

[52] R. Riedel et al. "Thermal properties of borate crystals for high power optical parametric chirped-pulse amplification". In: *Opt. Express* 22.15 (2014), pp. 17607–17619. DOI: 10.1364/OE.22.017607.

[53] A. Alexandrovski et al. "Photothermal common-path interferometry (PCI): new developments". In: SPIE, 2009, p. 71930D. DOI: 10.1117/12.814813.

[54] M. Sheik-Bahae et al. "Sensitive measurement of optical nonlinearities using a single beam". In: *IEEE Journal of Quantum Electronics* 26.4 (1990), pp. 760–769. DOI: 10.1109/3.53394.

[55] *AMPHOS GmbH Website*. 2022. URL: https://www.amphos.de/.

[56] P. Russbueldt et al. "Innoslab Amplifiers". In: *IEEE Journal of Selected Topics in Quantum Electronics* 21.1 (2015). DOI: 10.1109/JSTQE.2014.2333234.

[57] M. Namboodiri et al. "Optical properties of Li-based nonlinear crystals for high power mid-IR OPCPA pumped at 1 µm under realistic operational conditions". In: *Opt. Mater. Express* 11.2 (2021), pp. 231–239. DOI: 10.1364/OME.414478.

[58] M. K. R. Windeler et al. "100 W high-repetition-rate near-infrared optical parametric chirped pulse amplifier". In: *Opt. Lett.* 44.17 (2019), pp. 4287–4290. DOI: 10.1364/OL.44.004287.

[59] M. Sabaeian et al. "Temperature Distribution in a Gaussian End-Pumped Nonlinear KTP Crystal: the Temperature Dependence of Thermal Conductivity and Radiation Boundary Condition". In: *Brazilian Journal of Physics* 45.1 (2015), pp. 1–9. DOI: 10.1007/s13538-014-0291-x.

[60] S. Seidel and G. Mann. "Numerical modeling of thermal effects in nonlinear crystals for high-average-power second harmonic generation". In: SPIE, 1997, pp. 204–214. DOI: 10.1117/12.273671.

[61] L. I. Isaenko and A. P. Yelisseyev. "Recent studies of nonlinear chalcogenide crystals for the mid-IR". In: *Semiconductor Science and Technology* 31.12 (2016), p. 123001. DOI: 10.1088/0268-1242/31/12/123001.

[62] A. V. Smith. *SNLO nonlinear optics code (free version)*. 2023. URL: https://as-photonics.com/snlo/.

[63] R. DeSalvo et al. "Self-focusing and self-defocusing by cascaded second-order effects in KTP". In: *Opt. Lett.* 17.1 (1992), pp. 28–30. DOI: 10.1364/OL.17.000028.

[64] M. Falconieri. "Thermo-optical effects in Z -scan measurements using high-repetition-rate lasers". In: *Journal of Optics A: Pure and Applied Optics* 1.6 (1999), p. 662. DOI: 10.1088/1464-4258/1/6/302.

[65] P. Larkin. *Infrared and Raman Spectroscopy; Principles and Spectral Interpretation*. 2011. DOI: 10.1016/C2010-0-68479-3.

[66] P. Griffiths and J. Haseth. *Fourier Transform Infrared Spectrometry, Second Edition*. John Wiley & Sons, Inc., 2006. DOI: 10.1002/9780470106310.ch9.

[67] K. Hashimoto et al. "Complementary vibrational spectroscopy". In: *Nature Communications* 10.1 (2019), p. 4411. DOI: 10.1038/s41467-019-12442-9.

[68] R. Fritzsch et al. "Two-dimensional infrared spectroscopy: an emerging analytical tool?" In: *Analyst* 145 (2020), pp. 2014–2024. DOI: 10.1039/C9AN02035G.

[69] D. Zhang et al. "Depth-resolved mid-infrared photothermal imaging of living cells and organisms with submicrometer spatial resolution". In: *Science Advances* 2.9 (2016), p. 1600521. DOI: 10.1126/sciadv.1600521.

[70] M. Hermes et al. "Mid-IR hyperspectral imaging for label-free histopathology and cytology". In: *Journal of Optics* 20.2 (2018), p. 023002. DOI: 10.1088/2040-8986/aaa36b.

[71] T. T. Luu et al. "Extreme ultraviolet high-harmonic spectroscopy of solids". In: *Nature* 521.7553 (2015), pp. 498–502. DOI: 10.1038/nature14456.

[72] S. Gholam-Mirzaei, J. Beetar, and M. Chini. "High harmonic generation in ZnO with a high-power mid-IR OPA". In: *Applied Physics Letters* 110.6 (2017), p. 061101. DOI: 10.1063/1.4975362.

[73] M. Först et al. "Nonlinear phononics as an ultrafast route to lattice control". In: *Nature Physics* 7.11 (2011), pp. 854–856. DOI: 10.1038/nphys2055.

[74] J. Huang. "Ultrashort mid-infrared pulse generation in soft-glass fibre laser system". PhD thesis. FAU Erlangen-Nürnberg, 2020. URL: https://open.fau.de/items/964bb6e6-996a-4301-80b7-b7c71410640d.

[75] W. S. Warren, H. Rabitz, and M. Dahleh. "Coherent Control of Quantum Dynamics: The Dream Is Alive". In: *Science* 259.5101 (1993), pp. 1581–1589. DOI: 10.1126/science.259.5101.1581.

[76] D. B. Strasfeld, S.-H. Shim, and M. T. Zanni. "Controlling Vibrational Excitation with Shaped Mid-IR Pulses". In: *Phys. Rev. Lett.* 99 (2007), p. 038102. DOI: 10.1103/PhysRevLett.99.038102.

[77] Y. Zhao et al. "High-speed scanless entire bandwidth mid-infrared chemical imaging". In: *Nature Communications* 14.1 (2023), p. 3929. DOI: 10.1038/s41467-023-39628-6.

[78] D. J. Maas et al. "Vibrational ladder climbing in NO by (sub)picosecond frequency-chirped infrared laser pulses". In: *Chemical Physics Letters* 290.1 (1998), pp. 75–80. DOI: 10.1016/S0009-2614(98)00531-4.

[79] T. Eidam et al. "Femtosecond fiber CPA system emitting 830 W average output power". In: *Opt. Lett.* 35.2 (2010), pp. 94–96. DOI: 10.1364/OL.35.000094.

[80] J. Limpert et al. "Performance Scaling of Ultrafast Laser Systems by Coherent Addition of Femtosecond Pulses". In: *IEEE Journal of Selected Topics in Quantum Electronics* 20.5 (2014), pp. 268–277. DOI: 10.1109/JSTQE.2014.2304135.

[81] A. Giesen and J. Speiser. "Fifteen Years of Work on Thin-Disk Lasers: Results and Scaling Laws". In: *IEEE Journal of Selected Topics in Quantum Electronics* 13.3 (2007), pp. 598–609. DOI: 10.1109/JSTQE.2007.897180.

[82] P. Russbueldt et al. "Compact diode-pumped 1.1 kW Yb:YAG Innoslab femtosecond amplifier". In: *Opt. Lett.* 35.24 (2010), pp. 4169–4171. DOI: 10.1364/OL.35.004169.

[83] V. Badikov et al. "$BaGa_4S_7$: wide-bandgap phase-matchable nonlinear crystal for the mid-infrared". In: *Opt. Mater. Express* 1.3 (2011), pp. 316–320. DOI: 10.1364/OME.1.000316.

[84] A.-L. Calendron et al. "White-light generation with sub-ps pulses". In: *Opt. Express* 23.11 (2015), pp. 13866–13879. DOI: 10.1364/OE.23.013866.

[85] M. Namboodiri et al. "Versatile few-cycle high-energy MID-IR OPCPA for nonlinear optics, spectroscopy and imaging". In: *Opt. Continuum* 1.5 (2022), pp. 1157–1164. DOI: 10.1364/OPTCON.451879.

[86] Z. Heiner, V. Petrov, and M. Mero. "Efficient, sub-4-cycle, 1-µm-pumped optical parametric amplifier at 10 µm based on $BaGa_4S_7$". In: *Opt. Lett.* 45.20 (2020), pp. 5692–5695. DOI: 10.1364/OL.403856.

[87] Z. Heiner et al. "Broadband vibrational sum-frequency generation spectrometer at 100 kHz in the 950-1750 cm^{-1} spectral range utilizing a $LiGaS_2$ optical parametric amplifier". In: *Opt. Express* 27.11 (2019), pp. 15289–15297. DOI: 10.1364/OE.27.015289.

[88] S. N. Smetanin et al. "50 mJ level, 20-picosecond, narrowband difference-frequency generation at 4.6, 5.4, 7.5, 9.2, and 10.8 µm in $LiGaS_2$ and $LiGaSe_2$ at Nd:YAG laser pumping and various crystalline Raman laser seedings". In: *Opt. Mater. Express* 10.8 (2020), pp. 1881–1890. DOI: 10.1364/OME.395370.

[89] L. Nybacka. "FTIR spectroscopy of glucose". MA thesis. Uppsala universitet, 2016. URL: https://api.semanticscholar.org/CorpusID:114076654.

[90] J. Chen and H. Furukawa. "Rapid and non-invasive detection of high-thickness glucose solution concentrations using quantum cascade laser-based transmission infrared spectroscopy". In: *Infrared Physics & Technology* 131 (2023), p. 104717. DOI: 10.1016/j.infrared.2023.104717.

[91] A. Golparvar et al. "Very Selective Detection of Low Physiopathological Glucose Levels by Spontaneous Raman Spectroscopy with Univariate Data Analysis". In: *BioNanoScience* 11.3 (2021), pp. 871–877. DOI: 10.1007/s12668-021-00867-w.

[92] K. E. Shafer-Peltier et al. "Toward a Glucose Biosensor Based on Surface-Enhanced Raman Scattering". In: *Journal of the American Chemical Society* 125.2 (2003), pp. 588–593. DOI: 10.1021/ja028255v.

[93] S. Chattopadhyay et al. "Non-enzymatic glucose sensing by enhanced Raman spectroscopy on flexible 'as-grown' CVD graphene". In: *Analyst* 140 (2015), pp. 3935–3941. DOI: 10.1039/C5AN00546A.

[94] EKSPLA. *Sum Frequency Generation vibrational spectroscopy*. 2024. URL: https://ekspla.com/product/broadband-sfg-spectrometer.

[95] L. Velarde and H.-F. Wang. "Unified treatment and measurement of the spectral resolution and temporal effects in frequency-resolved sum-frequency generation vibrational spectroscopy (SFG-VS)". In: *Phys. Chem. Chem. Phys.* 15 (2013), pp. 19970–19984. DOI: 10.1039/C3CP52577E.

[96] M. B. Raschke et al. "Doubly-resonant sum-frequency generation spectroscopy for surface studies". In: *Chemical Physics Letters* 359.5 (2002), pp. 367–372. DOI: 10.1016/S0009-2614(02)00560-2.

[97] D. Ojha, N. K. Kaliannan, and T. D. Kühne. "Time-dependent vibrational sum-frequency generation spectroscopy of the air-water interface". In: *Communications Chemistry* 2.1 (2019), p. 116. DOI: 10.1038/s42004-019-0220-6.

[98] S. Sun et al. "Phase-Sensitive Sum-Frequency Generation Measurements Using a Femtosecond Nonlinear Interferometer". In: *The Journal of Physical Chemistry C* 123.12 (2019), pp. 7266–7270. DOI: 10.1021/acs.jpcc.9b00861.

[99] Y. Hsiao et al. "Momentum-dependent sum-frequency vibrational spectroscopy of bonded interface layer at charged water interfaces". In: *Science Advances* 9.15 (2023), p. 2823. DOI: 10.1126/sciadv.adg2823.

[100] A. M. Briggs et al. "Structure and Thermal Stability of Dichain Sugar Surfactants at the Solid/Water Interface Studied by Sum-Frequency Vibrational Spectroscopy". In: *Langmuir* 15.5 (1999), pp. 1817–1828. DOI: 10.1021/la981276b.

[101] H. C. Hieu et al. "Wetting effect on optical sum frequency generation (SFG) spectra of d-glucose, d-fructose, and sucrose". In: *Spectrochimica Acta Part A: Molecular and Biomolecular Spectroscopy* 138 (2015), pp. 834–839. DOI: 10.1016/j.saa.2014.10.108.

[102] R. Danilevičius et al. "Novel OPCPA based source for broadband high resolution sum frequency generation spectroscopy". In: *2017 CLEO/Europe-EQEC*, p. 1. DOI: 10.1109/CLEOE-EQEC.2017.8086867.

[103] X.-H. Hu et al. "α-Quartz Crystal as Absolute Intensity and Phase Standard in Sum-Frequency Generation Vibrational Spectroscopy". In: *The Journal of Physical Chemistry C* 123.24 (2019), pp. 15071–15086. DOI: 10.1021/acs.jpcc.9b03202.

[104] W.-T. Liu and Y. R. Shen. "Sum-frequency phonon spectroscopy on α-quartz". In: *Phys. Rev. B* 78 (2008), p. 024302. DOI: 10.1103/PhysRevB.78.024302.

[105] M. Makarem et al. "Probing cellulose structures with vibrational spectroscopy". In: *Cellulose* 26.1 (2019), pp. 35–79. DOI: 10.1007/s10570-018-2199-z.

[106] F. A. Bettelheim et al. *Introduction to Organic and Biochemistry*. Brooks/Cole Pub Co, 2008.

[107] P. J. Linstrom and W. G. Mallard. *NIST Chemistry WebBook, NIST Standard Reference Database Number 69*. National Institute of Standards and Technology, 2024. URL: https://doi.org/10.18434/T4D303.

[108] *D-(+)-Glucose Raman spectrum from SpectraBase*. 2024. URL: https://spectrabase.com/spectrum/8GygCmzr5jL.

[109] M. V. Korolevich, R. G. Zhbankov, and V. V. Sivchik. "Calculation of absorption band frequencies and intensities in the IR spectrum of α-d-glucose in a cluster". In: *Journal of Molecular Structure* 220 (1990), pp. 301–313. DOI: 10.1016/0022-2860(90)80120-9.

[110] M. Dudek et al. "Raman Optical Activity and Raman spectroscopy of carbohydrates in solution". In: *Spectrochimica Acta Part A: Molecular and Biomolecular Spectroscopy* 206 (2019), pp. 597–612. DOI: 10.1016/j.saa.2018.08.017.

[111] R. Khatib et al. "Water orientation and hydrogen-bond structure at the fluorite/water interface". In: *Scientific Reports* 6 (2016), p. 24287. DOI: 10.1038/srep24287.

[112] D. Jin et al. "Flotation separation of fluorite and calcite using anhydrous glucose and aluminum sulfate as a combined depressant". In: *Applied Surface Science* 624 (2023), p. 157089. ISSN: 0169-4332. DOI: 10.1016/j.apsusc.2023.157089.

[113] Z. Heiner et al. "Efficient generation of few-cycle pulses beyond 10 µm from an optical parametric amplifier pumped by a 1-µm laser system". In: *Scientific Reports* 12.1 (2022), p. 5082. DOI: 10.1038/s41598-022-08964-w.